| Technical Report | 465 |
|---|---|
| LES-6 Antenna System | R. N. Assaly<br>M. E. Devane<br>B. F. LaPage<br>M. L. Rosenthal<br>A. Sotiropoulos<br><br><br>10 March 1969 |

# Lincoln Laboratory

MASSACHUSETTS INSTITUTE OF TECHNOLOGY

Lexington, Massachusetts

MASSACHUSETTS INSTITUTE OF TECHNOLOGY

LINCOLN LABORATORY

# LES-6 ANTENNA SYSTEM

*R. N. ASSALY*
*M. E. DEVANE*
*B. F. LaPAGE*
*M. L. ROSENTHAL*
*A. SOTIROPOULOS*

Group 61

TECHNICAL REPORT 465

10 MARCH 1969

LEXINGTON                                        MASSACHUSETTS

ABSTRACT

The antenna system for Lincoln Laboratory's sixth experimental satellite (LES-6) is described. It is the first circularly polarized, despun, VHF antenna to be successfully used on an orbiting satellite. A relatively high-gain (11-db peak) beam is electronically scanned to be always Earth-directed. The evolution from the simple LES-5 antenna system is detailed, and performance characteristics of the flight configuration are given.

## CONTENTS

# LES-6 ANTENNA SYSTEM

## I. INTRODUCTION

The sixth Lincoln Experimental Satellite (LES-6, shown in Fig. 1) is the second all-solid-state VHF communications satellite designed and built by Lincoln Laboratory. It was placed in a near-circular, synchronous orbit on 26 September 1968 by a Titan III-C launch vehicle. LES-6 is spin-stabilized and rotates at $7\frac{1}{4}$ rpm about an axis nearly normal to its orbital plane which coincides with the Earth's equatorial plane. Like its predecessor, LES-5, this new satellite is stabilized with a magnetic torquing system. Unlike LES-5, however, LES-6 has automatic, self-contained station-keeping equipment which maintains the satellite's position over a desired Earth coordinate. This location can be altered by command from a ground station, and the station-keeping system will then automatically maintain the new position completely independent of the ground station. Therefore, enemy jamming is not a problem so far as the station-keeping function is concerned.

LES-5 had a relatively low-gain omnidirective antenna array,[1] while LES-6 has a high-gain, despun, steerable-beam antenna system. It is the first circularly polarized VHF antenna with a beam automatically kept pointing toward Earth. This is accomplished by electronically switching the beam through 16 different positions, equally spaced around the satellite's equator. The effective radiated power of the transmitted beam is almost 1 kW, representing a significant advance over previous VHF communications satellites.

## II. GENERAL DESCRIPTION

LES-6 is basically the same size and shape as LES-5: a right-circular cylinder, 4 feet in diameter and $5\frac{1}{2}$ feet high. A sketch of the LES-6 configuration is shown in Fig. 2. Unlike LES-5, the entire lateral surface is covered with solar cells except for a 6-inch wide "viewband" around the center of the cylinder. Between the solar panels are $\frac{1}{4}$-inch gaps which are utilized as circumferentially polarized slot antenna elements. There are two sets of 8 equally spaced slot elements, one set on each side of the viewband. Directly over each slot, and parallel to it, is a dipole supported 6 inches from the cylinder to provide the orthogonal axially polarized field. Appropriate electrical phasing of the excitations of the slots and dipoles results in circular polarization.

Some of the dipole antenna elements can be seen in Fig. 2. There are 8 equally spaced dipoles around the circumference of each half of the satellite above and below the viewband — 16 elements in all, arranged as 8 collinear pairs. Each dipole is self-supported by means of its feed lines and a mounting pad on the solar panel. As can be seen in Fig. 1, the feed lines, which actually constitute a balun (balanced-to-unbalanced transformer), are bent in a curve to put each

dipole directly over its associated slot. As stated above, these 16 dipoles provide the axially polarized component of the circularly polarized field, while the 16 slot elements, arranged as 8 collinear pairs like the dipoles, supply the circumferentially polarized component. However, only 2 adjacent collinear pairs of dipole and slot elements are in use at any one time. Thus, a directive, circularly polarized beam is formed with maximum field normal to the spin axis. By electronic sequential switching, the beam scans through 16 equally spaced positions, with sensor-controlled switching logic pointing the beam toward Earth, as the satellite rotates.

Solar panels are similar to those used on LES-5 except there are twice as many, 32 in all: 16 on the upper half, and 16 on the lower half of the satellite. Each solar panel is curved to conform to the cylindrical outside surface of the satellite which is, in fact, mainly composed of the solar cells themselves. A frame of fiberglass rings, with U-shaped (channel) cross sections and thin-aluminum transverse channels, supports the solar panels for each half of the satellite (upper and lower). The two halves are joined by structural members which constitute a frame for the viewband. An inner cylinder of thin aluminum, about 1 inch from the inner surface of the solar panels, forms an annular region which is divided into 8 cavities by the equally spaced transverse channels. Each of these cavities serves to terminate a slot antenna element. They are called "backup" cavities because they prevent radiation back into the satellite. A slot thus constrained to radiate in one direction is called a "cavity-backed slot."

The viewband is so-called because it contains the optical sensors which establish Earth references for station-keeping and antenna-beam pointing. Inside the satellite, adjacent to the viewband, is a platform for the communications, telemetry, beacon, and radiometry equipment boxes and interconnecting cables. Also on this platform, and in the viewband, are the station-keeping thrusters which emit gas whenever necessary to reposition the satellite in its proper orbit.

Within the communications equipment box is a transponder whose function is to generate a signal of frequency $f_T$ in the neighborhood of 250 MHz at a power level of $P_T \simeq 50$ dbm (100 watts), and to detect signals at a frequency in the neighborhood of $f_T + 50$ MHz at levels as low as $-120$ dbm. The beacon produces a signal with frequency $f_B = f_T + 5$ MHz at a power level $P_B = 36$ dbm (4 watts). A radiometry instrument monitors radio-frequency-interference (RFI) signals throughout a band from $f_R = f_T + 40$ to $f_T + 65$ MHz (RFIL to RFIH) also at levels of $-120$ dbm. The slot-dipole antenna system is used for the radiation and reception of these signals simultaneously. In order that the signals be handled in common, they are combined by a triplexer with pass bands at frequencies $f_T$, $f_B$, and $f_R$. The RF circuit layout, showing the connections between the various systems, is shown in Fig. 3. Separate diode switches are used for the slots and dipoles. The signal from the triplexer is divided by a hybrid to provide the inputs to the switches. The hybrid in the line feeding the dipole switch provides the proper relative phase between the slots and the dipoles, over the frequency range.

Most of the satellite structural parts are fabricated from lightweight, high-strength aluminum sections and the fiberglass rings described previously. Both the equipment platform and the solar panel construction feature a thin-aluminum skin epoxy-bonded to an aluminum honeycomb core.

Total weight of the complete satellite at launch was about 360 pounds.

## III. DESIGN CONSIDERATIONS

The original plan was to use the same dipole and slot antenna elements on LES-6 as were used on LES-5. However, the available volume within the shroud of the launch vehicle was increased

to allow room for the dipoles.  Thus, they did not have to be stowed against the cylinder during launch and then deployed in orbit, as on LES-5.  This permitted the use of two fixed, collinear half-wave dipoles in place of each full-wave dipole used on the previous satellite.  A much improved antenna element resulted from this change, both electrically and mechanically.

Little change was made in the basic cavity-backed slot configuration, but the feed and matching network were completely redesigned.  Although the lowest frequency of operation (the transmit frequency) is higher on LES-6 than it was on LES-5, the backup cavity is still operating closer to the cutoff frequency than is usually the case, and the slot impedance characteristic is a very difficult one to match over the required frequency range.  The transformer feed of LES-5 was not suitable for the new frequency range, and an entirely different approach had to be used.  Also on LES-5, the advantage of not having physical contact between the feed and the inner surface of the solar panel proved to be offset by the fact that the gap between the transformer and the solar panel had to be held to a very close tolerance.  Each of the LES-6 slots are center fed right across the $\frac{1}{4}$-inch gap between solar panels, and the resulting input impedance is matched by means of two coaxial-cavity matching devices.

Another departure from LES-5 is the use of an entirely separate antenna for the telemetry system.  This is a short monopole in the center of a ground plane on top of the satellite, as shown in Fig. 2.  The telemetry signals are transmitted at a lower frequency than the communications transmit frequency, and the use of a separate antenna permits the main antenna system to operate over a narrower frequency band.  Also, the redundancy increases reliability, and the problem of having intermodulation noise produced when a single antenna is used for transmitting several different frequencies is reduced since only the beacon and communications transmitter use the main antenna system.

The experience gained with LES-5 in the generation and suppression of intermodulation noise indicates that, in addition to adequate isolation of the two transmit functions, all common electrical contact surfaces must be free of nonlinear elements.  Therefore, where metal-to-metal contact occurs, the surfaces are gold-plated and kept absolutely clean.  Extensive tests were conducted to measure the power level of the intermodulation, and procedures were adopted to reduce it to acceptable levels.

A feature of LES-5 was the fail-safe design inherent in the use of the hybrid junction between the dipoles and slots.  If the dipoles had failed to deploy, half the power would still be delivered to the slots which could then operate normally as a linearly polarized antenna.  Four similar hybrids are used in LES-6 to perform a variety of power-division and phasing functions.  They also serve to isolate the effects of any possible failure on one side of the antenna system.

A failure in any part of the sensing, logic, and switching circuitry could cause the antenna beam to point away from Earth.  In the event of such spurious operation, provision is made to switch the antenna to an omnidirective mode (omni-mode) so that it will operate essentially the same as LES-5.  System gain will naturally be less than normal due to the reduced antenna directivity, but some communication links can be provided between the satellite and the higher gain ground stations.  This omni-mode is also useful when testing various combinations of sensing and logic circuit operation in orbit.

## IV.  DEVELOPMENT

### A.  Switch Matrix

An RF switch on a spinning satellite would serve to switch among n collimated beams equally spaced around the satellite, with the beam aimed most nearly toward Earth being turned on.  This

results in a higher gain than from a stationary omnidirectional antenna system. The switch would be designed to excite specific elements which produce a pattern that is highest, or nearly highest, in gain of the many alternatives for any station on the Earth. The switch will be operated by logic circuits in conjunction with Earth and Sun sensors.

First, a choice of switch configuration had to be made, and this is intimately related to the desired antenna patterns. Therefore, the investigation of antenna patterns and Earth coverage occupied the initial phase of the program.

### 1. Antenna Patterns and Choice of Switch Matrix Configuration

#### a. Discussion of Antenna Patterns in General

A communication system between the satellite O and the Earth center E is represented in Fig. 4 where the typical pattern of a beam in the two limiting cases is shown: the moment it is turned ON (solid curve), and the moment it goes OFF (dashed curve). An arbitrary line OA is designated the beam center so that other lines may be referred to it. In the first moment, a station at P is located at an angle AOP from the beam center and, as shown in Fig. 4, the angle is the largest that would be seen by the station. For this station, the satellite is on the horizon. Similarly, at the last moment, the largest angle is BOQ, where now the beam has moved through angle AOB and the "most poorly" located station is at Q. The angular range of the antenna pattern that is of concern is then given by

$$2\varphi_o = \angle AOP + \angle BOQ \quad . \tag{1}$$

Now,

$$\angle AOP = \angle AOE + \angle POE \tag{2}$$

and

$$\angle BOQ = \angle BOE + \angle QOE \quad . \tag{3}$$

Therefore,

$$2\varphi_o = \angle AOE + \angle POE + \angle BOE + \angle QOE \quad . \tag{4}$$

There are n beams, and each beam is on for $1/n$ of one rotation of the satellite. Hence,

$$\angle AOE + \angle BOE = \angle AOB = \frac{2\pi}{n} \quad . \tag{5}$$

At the altitude of the synchronous satellites ($3.59 \times 10^7$ meters),

$$\angle POE = \angle QOE = 0.15 \text{ rad } (8\tfrac{1}{2}°) \quad . \tag{6}$$

This angle shall be denoted $\Theta_o$. Equation (4) becomes

$$2\varphi_o = \frac{2\pi}{n} + 2\Theta_o \quad . \tag{7}$$

Some values of $2\varphi_o$ are

| n | 4 | 8 | 12 | 16 | ∞ |
|---|---|---|---|---|---|
| $2\varphi_o$ | 107° | 62° | 47° | $39\tfrac{1}{2}$° | 17° |

Figure 5 shows the region $\sigma$, enclosed by the curve $\Gamma$, in which any ground station can be located; the length is $2\varphi_o$, and the width is $2\Theta_o$. A rectangular coordinate system is centered

4

in the region.  Coordinates of various points related to one semicircle are given in the figure.

With the limited control of the antenna element excitations, the choice of best pattern is restricted.  If the pattern is represented by the intensity function $l(\varphi, \Theta)$, the minimum value of $l$ in the region $\sigma$ is of concern, since it should be as large as possible.

The $\Theta$-axis pattern cannot be varied if it is to be symmetrical about $\Theta = 0$.  (There are two rows of elements, and the excitations for the two must be the same.)  Logically, then, the $\varphi$-axis pattern should be optimized.  The lowest signals of this pattern occur at point P and the corresponding point on the opposite side.

Various situations are illustrated in Fig. 6 with three directivity patterns A, B, and C of increasing beamwidth.  If angle $\varphi_0$ has the value shown, pattern B is the best choice.  At another value, one of the other patterns might be a better choice.

Suppose the pattern is approximated by a parabola, thusly:

$$l(\varphi, 0) = b(\xi - \varphi^2) \quad \text{for } \varphi^2 < \xi$$

$$\qquad\qquad = 0 \qquad\qquad \text{for } \varphi^2 > \xi \quad . \tag{8}$$

The peak field is $b\xi$, and the beamwidth is determined by the value of $\xi$.  The next step is to find the relation between the two, where the total energy radiated is constant.

The total energy is proportional to the energy radiated along the plane $\Theta = 0$ (since the relative $\Theta$-axis pattern does not change).  The integral

$$E = \int_{-\pi}^{\pi} I(\varphi, 0) \, d\varphi \tag{9}$$

is then a constant.  Substituting Eq. (8),

$$E = \int_{-\sqrt{\xi}}^{\sqrt{\xi}} b(\xi - \varphi^2) \, d\varphi \tag{10}$$

or

$$E = \frac{4}{3} b\xi^{3/2} \quad . \tag{11}$$

Equation (8) becomes

$$l(\varphi, 0) = \frac{3}{4} E(\xi^{-1/2} - \xi^{-3/2}\varphi^2) \quad \text{for } \varphi^2 < \xi \quad . \tag{12}$$

The question now is:  For what value of $\xi$ is the field $l(\varphi_0, 0)$ maximum, when $\varphi_0$ is given?  This is found by equating to zero the differential of $l$ with respect to $\xi$.  Thus,

$$\xi = \xi_m = 3\varphi_0^2 \quad . \tag{13}$$

Then, the field intensity is

$$I(\varphi_0, 0) = I_m(\varphi_0, 0) = \frac{E}{\sqrt{12}\,\varphi_0} = \frac{E}{2\sqrt{\xi_m}} \quad . \tag{14}$$

5

For the same pattern, the intensity at $\varphi = 0$ is

$$l_m(0, 0) = \frac{3}{4} \frac{E}{\sqrt{\xi_m}} \quad . \tag{15}$$

By dividing Eq. (14) by Eq. (15), the following interesting result is obtained:

$$\frac{l_m(\varphi_o, 0)}{l_m(0, 0)} = \frac{2}{3} \rightarrow -1.8 \, db \quad . \tag{16}$$

This implies that, for a specified value of $\varphi_o$, the directivity goes through a maximum as $\xi$ is increased; this maximum occurs at $\xi_m = 3\varphi_o^2$. For larger values of $\xi$, the pattern is more uniformly flat but low in directivity throughout. On the other hand, if $\xi$ is smaller the pattern is narrower, and although the peak directivity is higher, it drops off too rapidly at increasing values of $\varphi$.

In this discussion, an antenna pattern with a simple form was assumed and, consequently, the accuracy of the conclusions comes into question. Suppose that the fields $l_m(\varphi_o, 0)$ and $l_m(0, 0)$ are the maximum that can be obtained from a realistic situation, rather than from the simplified situation considered. If angle $\varphi_o$ is decreased, $l_m(\varphi_o, 0)$ and $l_m(0, 0)$ both increase since the radiated energy is now concentrated in a smaller angle. If the ratio is constant, for the cases of interest, it provides a significant aid to the pattern selection.

b. Arrangements of Antenna Excitations and Beams

In any scheme implemented on the satellite for generating the antenna patterns, m = 1, 2, 3, or 4 adjacent element pairs are excited at a time. More than four is not feasible, since radiation from two of the ON elements is in diametrically opposite directions. For m = 1, only one pattern exists so far as change in the phase and amplitude are concerned. For m = 2, the peak gain of the pattern will be higher than for m = 1. Furthermore, the beam direction can be controlled within limits by adjusting the relative phases. With m = 3, having the three amplitudes equal could produce a higher peak gain than for m = 2. Unequal amplitudes (for example, exciting the middle element with a higher amplitude than the elements on either side) might further enhance the gain. As in the m = 2 case, the beam can be aimed within limits by appropriate phasing. For m = 4, higher gains might not be obtained since two element pairs are 135° apart, quite a large value. A reasonable assumption is that the peak gain is highest when the two middle-element pairs are excited equally, and the outer pairs are also equal but possibly at another level.

Each of the patterns that exist for these several cases has associated with it a beamwidth which can give a fairly good indication of the directivity. Hence, the pattern will be near optimum for some angle $2\varphi_o$. The angle having been found, the value of n can then be found by Eq. (7). A definite relation has then been established between the number of beams for which to design the satellite, and the number of antenna elements to excite at a time.

Equatorial-plane directivity patterns were calculated[2] at the transmit frequency for the slots. Four patterns are plotted in Fig. 7, in terms of the directivity $D(\varphi, 0)$, showing only a part of the main lobe. One pattern (m = 1) is of a single-slot pair. The other three patterns (m = 2, 3, and 4) are based on the condition that amplitudes of the excitations are equal and the phases are adjusted so that the signals arrive in phase at a plane whose normal is centrally located among the ON antennas. Also in Fig. 7, the angle $\varphi_o$ [given by Eq. (7)] is plotted for n with values of 4, 8, 12, 16, and $\infty$. If the choice were limited to the four patterns, for n = 4, pattern m = 1 is the

6

best choice; for n = 8, the choice is pattern m = 2; for n = 12 or 16, it is pattern m = 3; and for n = ∞, it is pattern m = 4. In the cases n = 8, 12, and 16, for the best pattern, $[I(\varphi_O, 0)/I(0, 0)] = [D(\varphi_O, 0)/D(0, 0)] \rightarrow -2.1, -2.3,$ and $-1.7$ db, respectively. These values are not too different from the value of $-1.8$ db given in Eq. (16).

The patterns m = 3 and 4 can be broadened or narrowed if the relative amplitude or phase is changed. Thus, there are any number of alternative patterns to the four shown in Fig. 7. Furthermore, the calculated patterns are not very accurate due to the neglect of the mutual coupling between antennas. The point of these statements is that, given n, a number of patterns may be calculated to obtain $D(\varphi_O, 0)$, and the pattern with the largest value $D_{max}(\varphi_O, 0)$ may be chosen, but the result may not be the same as that obtained by actual pattern measurements. Suppose, however, that there are two patterns (one calculated and one measured) whose main lobes have about the same shape. (They may arise from different antenna excitations.) If the calculated pattern is optimum, then the measured pattern will be also nearly optimum and the ratio $D_{max}(\varphi_O, 0)/D(0, 0)$ will be about the same in the two cases. If this ratio can be calculated, then it can be applied to a measured pattern to find the angle $\varphi_O$ for which it is optimum. The alternate procedure of measuring many patterns and comparing the directivities at different angles $\varphi_O$ involves considerably more effort.

Many patterns were calculated, and the directivities $D(\varphi_O, 0)$ were plotted vs $D(\varphi_O, 0)/D(0, 0)$ for n = 8 and 16; the plot is shown in Fig. 8. Except for some scattering of points, there is a well-defined trend. Both curves exhibit a maximum directivity $D_{max}(\varphi_O, 0)$ at approximately $D(\varphi_O, 0)/D(0, 0) \rightarrow -2.0$ db. This is in good agreement with the value of $-1.8$ db determined previously. In conclusion, the ratio $D(\varphi_O, 0)/D(0, 0) = -2.0$ db can be applied to a measured pattern to determine angle $\varphi_O$, and therefore n, by Eq. (7). A switch configuration may then be chosen.

Typical measured patterns of one slot pair and one dipole pair at frequency $f_T$ are shown at the top of Fig. 9, and both are plotted on a scale where their peaks are arbitrarily set at 0 db. The slot pattern agrees fairly well with the calculated pattern in Fig. 7, but the dipole pattern is somewhat narrower.

The patterns at the bottom of Fig. 9 are the gains of two dipole pairs and two slot pairs as measured at the input to the cable that would be connected to the triplexer. Hence, it includes cable and power-divider losses. Because of differences in configuration and matching technique, the dipole pattern has about 1.6-db higher gain than the slot pattern. By considering first the dipole pattern, the ratio $D(\varphi, 0)/D(0, 0)$ is $-2.0$ db at $\varphi = 21\frac{1}{2}°$ and, therefore, the optimum n is about 14. If n is set equal to 16, the ratio $D(\varphi, 0)/D(0, 0)$ has the value $-1.7$ db as indicated by the line in Fig. 9, and this should be satisfactory.

In the case of the slots, because of mutual coupling, the pattern depends on the termination of those slot pairs that are not excited. In the satellite system, this termination would be approximately an open circuit at the output of the switch matrix. Thus, for these pattern measurements, adjustable open-circuited lines terminated the six unexcited slot pairs. For each length adjustment, the six distances were kept equal. Four of the measured patterns (A, B, C, and D) are shown in Fig. 9. Pattern A is found to have the highest peak gain. Then, the pattern trend is through B, C, and to D which has the lowest peak 1.2 db below that of pattern A.

Pattern D has nearly the same appearance as the calculated pattern m = 2 in Fig. 7. It is somewhat broader than the ideal of n = 16. The pattern A shows $D(\varphi, 0)/D(0, 0) = -2.0$ db at n = 16 and is therefore just the optimum. Note, incidentally, that these patterns all intersect at about 2 db below the average of the peaks.

Why the pattern can be controlled by the position of the open circuits of the unexcited slot pairs is qualitatively explained by supposing that RF energy coupled to these slots is reflected and reradiated, and hence affects the total pattern. The phase of the reradiated signal can be adjusted to enhance the peak gain. Pattern A of Fig. 9 approaches the m = 4 pattern in Fig. 7; therefore, exciting two slot pairs with correct use of mutual coupling is similar to exciting four slot pairs directly, with no mutual coupling.

Slot and dipole patterns measured along the $\Theta$-axis are shown in Fig. 10. The vertical dashed lines mark the north and south edge of the Earth. The ratio $D(0, \Theta)/D(0, 0)$ is about $-0.8$ db at these lines for both patterns. It is then likely that the patterns are broader and therefore of lower gain than the ideal pattern.

c. Choice of Configurations for the Switch Matrix

A good choice is to generate 16 beams, exciting two antennas at a time. The appropriate scheme is then as shown in Fig. 11, where the antennas are numbered 1 through 8 and the beam centers are lettered A through Q (omitting letter I).

To obtain beam A from antennas 1 and 2, there must be a difference of phase between signals at the two antennas. Likewise, beam B is obtained by reversing the phases of the two antenna signals. This implies that a 2P2T switch section is required. For any beam, one even-numbered antenna and one odd-numbered antenna are ON. Hence, a SP4T section is needed to select one of the four odd-numbered antennas, and another is needed to select one of the even-numbered antennas.

Under these considerations, the switch matrix takes the configuration shown in Fig. 12. The input signal is divided by a hybrid into two equal parts. One signal leads in phase by 90°, so that an additional length of line must be added to reduce this phase lead to a suitable value. Then, the two signals are fed into the two input ports of a 2P2T section. The two outputs are tied to the inputs of two SP4T sections and their output ports, in turn, are connected to the eight antennas.

The 2P2T and SP4T sections consist of twelve SPST units which are represented in Fig. 12 by circles blackened on one side and labeled "a" through "d" and "e" through "h" in the two SP4T sections, and "j" through "m" in the 2P2T section. If the states of these units are represented by waveforms which swing up for the OFF state and down for the ON state, they take the shape shown in Fig. 13. Any beam can be checked by determining the states shown in Fig. 13 and tracing the signal through the circuit in Fig. 12. For example, for beam A, SPST units a, e, k, and l are ON; this switches ON antennas 1 and 2. The additional line length ties to antenna 2, and the beam is shifted to the side of antenna 1.

For each diode that the RF signal passes through, there is an insertion loss of about 0.2 db. In addition, there is about 0.1-db loss due to radiation leakage out the OFF ports, as well as other incidental losses. This switch matrix will then have a total insertion loss of about 0.5 db. By the patterns of Fig. 9, the net antenna gain to be expected at angle $\varphi_0$ is then $9.6 - 0.5 = 9.1$ db for the dipoles and 7.2 db for the slots.

2. Switch Construction and RF Characteristics

The switch matrix consists of SPST units such as that shown in Fig. 12. A diode is placed in series with the RF inner conductor. When on forward bias, the diode is a conductor approximating a 1-ohm resistor; on reverse bias, it is an insulator but has a capacitance of about 1 pF. These states are denoted ON and OFF, respectively. Coils and capacitors in the circuit separate

the RF and bias signals. The 180-pF capacitor has a low reactance (3.5 ohms) at $f_T$, while the coil adjacent to the RF line is chosen to be parallel self-resonant at $f_T$ (its reactance there is over 2000 ohms). The ferrite coil helps the filtering as well as reducing the RFI coming in the bias lines. It also reduces the switching noise which will be discussed in Sec. IV-A-5-b. Two coils, shown in the switch matrix circuit at points B, provide the bias return for the twelve SPST units.

Stripline was chosen because of the convenience it provides in laying out circuits. The material selected was 1/8-inch thick, copper-clad Rexolite (a cross-linked styrene copolymer) which has a dielectric constant of 2.53 and a dissipation factor of 0.0004 at $f_T$. On one sheet, the circuit was etched from the copper clad using a photo-etch process (Fig. 14); on another sheet, the copper-clad surface was removed and the circuit was formed by placing the two sheets together. The copper clad on the outer surfaces was replaced by 1/32-inch thick, gold-plated aluminum for additional strength and to provide a path for heat dissipation.

Two SP4T sections are laid out on one circuit board in x-arrangements, and the 2P2T section is laid out on a second board in a square-diamond pattern. Then the boards are lined up, one atop the other, and joined by conductors as shown in Fig. 15.

To simplify the construction, the coils and capacitors are bonded outside the ground plane and their leads brought through drilled holes to the circuit where they are soldered. A place to route the bias lines also becomes available on the surface of the printed circuit. Measurements of impedance on some test items indicated there was a negligible difference in characteristics with or without the components [see Fig. 16(a-b)].

Diodes are soldered in small metal blocks which, in turn, are soldered to the printed circuit. Mating Rexolite boards have cutouts for these metal blocks and diodes, and when the two boards are together the outer surfaces of the ground plane and the metal blocks are coplanar (Fig. 17). This arrangement provides a convenient way to dissipate the significant amount of heat that may develop in the diodes by allowing a thermal conductor to be placed across the metal block to the ground plane. Boron nitride, which has a conductivity of about 0.5 watt/cm°C at 100°C (approximately that of steel), is the thermal conductor. Its dielectric constant is 4.1 and dissipation factor is 0.0011.

Figure 18 is a photograph of the switch sections that make up the whole unit. In addition to the SP4T and 2P2T circuits, there is a metal spacer to separate the circuits, the boron-nitride slabs, a 15-pin connector for the biases, and covers to go over the boron-nitride slabs to prevent the radiation of RF power. These covers are painted black to help dissipate the heat developed in the switch. Figure 19 shows the switch completely assembled. OSM-type connectors are mounted on the surface of the ground plane, while the inner conductor passes through the Rexolite where it is soldered to the circuit.

Considerable effort was expended in arriving at this design. In addition to the need for suitable RF characteristics, the thermal problem had to be taken into account. Furthermore, the amplitude of the intermodulation products and switching noise, although originating in the diodes, was determined to some extent by the circuit.

RF characteristics of the switch without the hybrid are now summarized in Table 1. Averages are given for the switch that was measured at one of the two inputs, while the other input was terminated in a matched load. An indication of the bandwidth of the device is given by Fig. 20 which is a plot of the VSWR vs frequency.

| TABLE I | | | |
|---------|---|---|---|
| SWITCH RF CHARACTERISTICS | | | |
| f | VSWR | Insertion Loss (db) | Isolation (db) |
| Transmit | 1.20 | 0.48 | 20 |
| Receive | 1.30 | 0.64 | 18 |

### 3. PIN Diode and Temperature

Initially, the diode chosen for this application consisted of a silicon chip of planar construction with silicon-dioxide passivation and a 0.002-inch thick I-layer. Another diode of different construction which exhibited lower intermodulation product and switching-noise amplitude was ultimately used. This diode is of mesa construction with glass passivation and a 0.003-inch thick I-layer (shown in detail in Fig. 21). Differences in characteristics depend, for the most part, on the 1-layer thickness. Manufacturer's specifications for the two diodes are summarized in Table II.

| TABLE II | | |
|----------|---|---|
| DIODE CHARACTERISTICS | | |
| I-layer thickness (inches) | 0.002 | 0.003 |
| Series resistance (ohms) $(f = 500 \text{ MHz}, I_F = 100 \text{ mA})$ | 0.6 to 1.0 | 0.45 to 0.8 |
| Total capacitance (pF) $(f = 1 \text{ MHz}, V_R = 50 \text{ volts})$ | 0.3 to 0.5 | 0.65 to 0.9 |
| Case capacitance (pF) | 0.16 | 0.16 |
| Reverse-bias voltage for current of 10 μA (volts) | 200 to 550 | >800 |
| Thermal resistance $\theta_i$ (°C/watt) | 10 to 20 | 15 to 30 |
| Minority carrier lifetime (μsec) | 1.5 | 2 to 4 |

In normal operation, diode heating is a concern, for the reliability decreases with increasing temperature. If the RF power level of the signal passing through the diode is $P_o$, the current is $\sqrt{P_o/R_o}$, where $R_o = 50$ ohms is the switch characteristic impedance. The power dissipated in the diode is approximately

$$P_d = R_s \frac{P_o}{R_o} \tag{17}$$

where $R_s$ is the diode series resistance. The temperature rise of the diode can then be put in the form

$$\Delta T = \theta_d P_d \quad . \tag{18}$$

If heat dissipation is by conduction, then $\Theta_d$ is a constant (i.e., independent of sink temperature), depending on the thermal conductivity of the materials and the geometry. If the heat is by radiation, then $\Theta_d$ depends on the viewing temperature.

The temperature rise ($\Delta T$) of the diode semiconductor chip cannot be measured directly, but the temperature rise of the diode outer surface can be measured; therefore, let $\Delta T$ be separated in two parts:

$$\Delta T = \Delta T_c + \Delta T_j \tag{19}$$

where $\Delta T_c$ is the temperature rise of the diode surface above the sink temperature. $\Delta T_c$ can be expressed as

$$\Delta T_c = \Theta_c P_d \quad . \tag{20}$$

In designing a switch, an objective is to make $\Theta_c$ as small as possible. Similarly,

$$\Delta T_j = \Theta_j P_d \quad . \tag{21}$$

There is nothing in the switch design that can be done to reduce this value, as the value of $\Theta_j$ is determined by the manufacturer. Substituting Eq. (17),

$$\Delta T_j = \Theta_j R_s \frac{P_o}{R_o} \quad . \tag{22}$$

Both $\Theta_j$ and $R_s$ have specific values for each diode and, for use in the switch, a choice can be made of diodes with lower values of the $\Theta_j R_s$ product.

The first significant attempt to reduce $\Theta_c$ was by soldering a diode to a 1-inch-square metal plate with a blackened surface which dissipates heat by radiation (this arrangement is shown in Fig. 22). (In all cases, the thermal path was chosen via the diode cathode because of the lower thermal resistance which is apparent from Fig. 21.) In one experiment, temperatures were measured at five points on the piece as indicated in Fig. 22. Results of each measurement in a vacuum chamber are shown in Fig. 23. Point 1 is on the metal rim of the diode cathode, and points 2 and 3 are on the metal plate. Temperatures at these points agreed within a couple of degrees, indicating a low thermal resistance from the diode through the metal plate. Point 4 on the edge of the switch showed a temperature rise of a somewhat lower value. Point 5 is the viewing temperature.

With the diode on forward bias, the switch was placed in series with the transmission line. Raising the bias from 30 to 50 mA produced a significant decrease in temperature, as shown in the graph (Fig. 23). With the diode on reverse bias, the switch was placed across the transmission line, with its second port terminated in the characteristic impedance, to simulate the switch matrix. As the graph shows, the temperature is considerably lower than for the forward-bias case. Also, a decrease in reverse bias from 100 to 25 volts increases the temperature somewhat.

Values of $\Theta_c$ were calculated for the various cases and are given in Table III. As described earlier, the configuration adopted for good heat dissipation is shown in Fig. 17. Boron nitride is used because of high heat conductivity and low electrical conductivity. A unit was set up in a vacuum chamber with three thermocouples: one bonded to the metal block to which the diode is soldered, one on the outer surface of the switch next to the edge of the boron nitride and about 1 inch from the diode, and one connected to the base on which the switch was supported (as shown in Fig. 17). Measured results are shown in Fig. 24. $\Theta_c$ is now about 20°C/watt, much better than the radiation model.

11

| TABLE III |
|-----------|
| $\theta_c$ VS TEMPERATURE |

| Viewing Temperature (°C) | $\theta_c$ (°C/watt) | | | |
|---|---|---|---|---|
| | Forward Bias | | Reverse Bias | |
| | 30 mA | 50 mA | 100 volts | 25 volts |
| −30 | 130 | — | 14 | — |
| 0 | 120 | — | 4 | — |
| 30 | 100 | 80 | 2 | 22 |

To test the diodes in a normally operating switch matrix, such a switch was set up with seven thermocouples and mounted on a triplexer filter as shown in Fig. 25. Four thermocouples were bonded to diodes m, g, k, and c; a fifth was bonded to the black cover on the switch (which is visible in Fig. 25); a sixth was bonded to one of the support legs of the switch; and the seventh was bonded on the filter under the switch (this last one provided the "sink" temperature). Table IV summarizes the temperatures measured from three modes of operation after conditions stabilized (requiring at least a 2-hour period) with 60-watt input. The three modes are: (1) Switch-on mode for beam J, that is with diodes ℓ, g, k, and c ON; (2) scan mode, where the switch is sequenced through the 16 beams at the normal satellite rate; (3) omni-mode, where all diodes are ON. In normal operation, the temperature rise is acceptably low.

| TABLE IV |
|----------|
| OPERATING-MODE SWITCH TEMPERATURE |

| Location | Temperature Rise Above Sink (°C) | | |
|---|---|---|---|
| | Beam J | Scan Mode | Omni−mode |
| Diode m (OFF) | 3 | 6 | 3 |
| Diode g (ON) | 6 | 5 | 1 |
| Diode k (ON) | 6 | 6 | −2 |
| Diode c (ON) | 11 | 4 | 4 |
| Switch surface | 2 | 4 | 0 |
| Support leg | 1 | 1 | 1 |

4. Diode Reliability

Diodes had to show a high degree of reliability in the environment to which they would be subjected. This included the shock and vibration of launch and an anticipated 5 years of operational life. In this lifetime, the diode would undergo many thermal cycles while handling 30 watts of RF power.

Other than a mechanical failure, the type of most concern is an intolerable increase in leakage current in the reverse-bias state. Under the stress of elevated temperatures, this leakage may increase irreversibly, with an evident degradation in diode performance. This was apparent

in a step-stress experiment that was performed; it consisted of subjecting a set of diodes to 100-volt bias at a series of temperatures for 24 hours, namely: 25°C, 50°C, 75°C, and so on up to and including 200°C. After each 24-hour period, the leakage current was measured at ambient conditions, and the results are shown in Fig. 26. The rapid increase in cold leakage current above 150°C, which indicates an irreversible change in the material of the diode, is significant. Hence, on the short-term basis, temperatures should be kept below this value.

A question still existed regarding diode reliability over a long period of time. To test this point, a run was made on 10 diodes for 4000 hours at 100-volt reverse bias and 125°C. Results of the more typical and the worst cases are given in Fig. 27. By extrapolating the results of the worst case, the time it takes to reach 100 $\mu$A is about 80 years. Thus, a good safety margin is assured for a nominal 5-year lifetime. This margin should improve further when the temperature in the satellite does not exceed 50°C.

A large number of diodes were screened and the weaker ones were eliminated. Screening included a visual and x-ray examination, a shock and vibration mode, and several continued stress tests which included stresses of 240 hours at 100°C without bias, 216 hours at ambient temperature on forward bias of 50 mA, and 48 hours at 100°C and 100-volt reverse bias. Of the 81 diodes tested, four became unacceptable. This low number indicates that none of the tests was severe enough to weaken the diodes.

     5. Intermodulation Products and Switching Noise

       a. Intermodulation

Intermodulation (IM) products are generated when a signal consisting of two frequencies and represented by the equation

$$i = 1_T \sin 2\pi f_T t + 1_B \sin 2\pi f_B t \tag{23}$$

passes through a nonlinear device whose characteristics may be described by a power series

$$e = \sum_\ell a_\ell i^\ell \quad . \tag{24}$$

IM frequencies are

$$f_{IM} = mf_T + nf_B \tag{25}$$

where m and n are integers. The order of the IM is given by

$$k = |m| + |n| \quad . \tag{26}$$

Figure 28 shows an array of IM terms together with the fundamental frequencies $f_T$ and $f_B$. Upper side-band orders — first, third, fifth, etc. — correspond to m = −1, −2, −3, ..., and n = 1 − m. The receive band shown here encompasses the fifteenth through the twenty-fifth orders. Since the IM power generally decreases with increasing order, the emphasis shall be on the fifteenth order in this discussion.

IM measurements were made on the two types of diodes described above which shall be designated as 2- or 3-mil diodes according to the I-layer thickness. A diode was mounted in a SPST unit and set up for IM measurements in the system shown in Fig. 29. Basically, this system combines two signals and sends them to the component under test. Signals falling in the receive band are then separated and monitored. This is similar to the arrangement in the communication

13

system, but the antennas have been replaced with matched loads. Two frequency-stable signals are amplified and combined in a triplexer (a triplexer is a junction of three band-pass filters used to separate signals falling in three bands). The combined signal then goes to the switch. IM falling in the receive band is then routed via the triplexer to a low-noise amplifier and spectrum analyzer. Adding an integrator and recorder provides additional sensitivity and a permanent record. This arrangement could measure signals of $-140$ dbm, 20 db below the expected sensitivity of the communication system. To measure forward-bias IM, the switch was placed in series with the transmission line; for reverse bias, it shunted the line.

Nominal operating levels for each diode, as shown in Fig. 29, are $P_T = 25$ watts, $P_B = 1$ watt, $V_R = 100$ volts or $1_F = 50$ mA, and $T = 10°C$. Diode IM was measured as a function of one or two of these parameters, while the others were held at the nominal levels.

Figure 30 shows the amplitudes of the IM for the 3-mil diode as a function of $P_T$, $P_B$, and $V_R$. The fifteenth order, which is plotted at the top, was measured at $-40°C$, $10°C$, and $60°C$; the nineteenth and twenty-third were measured for $10°C$ only. A second scale, the ratio $P_T/P_B$, was added to the plots involving $P_T$, since this ratio is significant. Some observations are that, in general,

(1) The higher-order IM have lower levels — they could not be observed in the cases indicated by four of the plots

(2) IM increases with decreasing temperature

(3) IM exhibits a peak as a function of $P_T$ or $V_R$; a peak is evident where $P_T = P_B$

(4) IM increases with $P_B$ over the range given in the plot.

A more interesting graph is shown in Fig. 31 which is a map on a $P_T - V_R$ plane showing contours of constant IM amplitude of the fifteenth order for the 3-mil diode. A peak in the amplitude of over $-90$ dbm runs diagonally upward to the right and drops off on either side. At the nominal operating power level of $P_T = 44$ dbm, the bias must be set at 60 volts or higher for the IM to be below $-130$ dbm. IM is also low at a low bias level but the margin is small, i.e., a small decrease in $P_T$ results in a rapid increase in IM. Interestingly, a maximum exists along the bias $P_T = P_B$ but is not as pronounced. The dashed curve labeled $V_T$ (peak) shows where the peak RF voltage equals the bias voltage. Its notability is that it provides an indication of how much of the nonlinear characteristic of the diode the combined voltage sees. Significantly, the peak in the IM roughly parallels this curve.

Figure 32 is a set of contours for the 2-mil diode. Note that now the diagonal peak of the IM is nearer the $V_T$ (peak) curve.

Measurements of IM for the 3-mil diode on forward bias failed to produce any observable values at bias levels from 10 to 50 mA as a function of the various parameters of power and temperature. On the other hand, the 2-mil devices exhibited IM power levels up to $-100$ dbm at forward-bias levels up to 50 mA. Many of the IM characteristics of the 2-mil diode have already been published.[3]

### b. Switching Noise

When the diode was switched from ON to OFF (or from OFF to ON) with the RF signals present, it emitted a signal burst which had a continuous spectrum throughout the receiver band. In an effort to characterize, understand, and control this noise, measurements were made on a SP2T switch where the bias state of the two diodes was alternated by a square-wave signal, one diode being ON while the other is OFF.

Figure 33 shows the switching-noise measurement setup. The spectrum analyzer is replaced by an oscilloscope which is synchronized with the switching waveform. Receiver bandwidth is narrowed to 7 MHz by the addition of a band-pass filter in order to simulate the transponder operation of our communication system. The RF signal is mixed down to a center frequency of about 40 MHz for suitable viewing on a conventional oscilloscope.

Figure 34(a) is an oscilloscope trace of the bias waveform and the RF signal at the moment when the SP2T switch is triggered. The scale is 1 $\mu$sec per major division. The OFF-going switch driver in this region is a constant current source. Initial oscillation is at the natural resonant frequency of the bias circuit (as loaded by the diode). At this moment, the diode is clamped while the stored charge is being depleted. There is sufficient stored charge to prevent the RF signals from depleting it in the negative half cycles. A point is reached where the stored charge is sufficiently small, then the negative half RF cycles fully and abruptly deplete the stored charge. The ensuing positive swing causes some rectification, resulting in the large spike of signal voltage. As the diode bias approaches the level of maximum intermodulation generation, the signal noise burst has a characteristic 5-MHz repetition frequency which is due to rectification of the difference signal $f_B - f_T$. This fact is more vividly illustrated in Fig. 34(b) where the OFF-state bias level is reduced to that where maximum IM generation occurs and the 5-MHz beat continues through the steady state.

Figure 35 shows a number of graphs of maximum amplitudes of the switching-noise signals as a function of $P_T$, $P_B$, $I_F$, and T. There are two sets for the two cases (OFF to ON, and ON to OFF), and each plot has curves for the three temperatures ($-40°C$, $10°C$, and $60°C$). From these data, some definite observations can be made:

(1) Noise amplitudes are considerably higher than the IM amplitudes, but generally last only a fraction of a microsecond

(2) Pulses are quite temperature-dependent, the higher amplitudes corresponding to lower temperatures

(3) ON-to-OFF amplitude peaks where $P_T = P_B$

(4) When only one signal is present, the amplitudes are still significant; introducing the second signal increases the noise substantially, which indicates intermodulation coming into play.

Included in the graphs are plots for a 2-mil diode of its $P_T$ dependence; the switching noise is generally 10 to 20 db higher. There are no graphs showing how the noise amplitude varies with $V_R$ since it had very little effect.

c. Switch Matrix

A large number of diodes were measured for IM and switching noise, and showed significant individual differences. (Those characteristics reported here are typical.) Diodes for the final switch matrix were selected for low IM and switching noise. Measurements were made of the IM and switching noise of the satellite switches in the receive band under a number of conditions. At the nominal levels ($P_T$ = 50 watts, $P_B$ = 2 watts (the power at the diodes are half these values), $V_R$ = 100 volts, $I_F$ = 50 mA, and T = 10°C), IM did not exceed $-135$ dbm. The switching noise remained below $-60$ dbm in the 7-MHz band, and its duration above $-90$ dbm was $<6\,\mu$sec.

B. Dipoles

By using the half-wave dipole, in a fixed location with respect to the satellite, the axially polarized antenna elements on LES-6 were developed more easily than on LES-5. Once the size

15

of the tubing used to support and form the dipole had been chosen, the mechanical parameters which could effect the electrical characteristics became invariant. A photograph of a dipole is shown in Fig. 36. Its support structure is curved to bring the dipole feed point over the slot on the satellite surface. The length of the dipole is approximately $0.4\lambda$, and the distance from the satellite which forms the ground plane is $\lambda/8$ at the transmit frequency.

The dipole itself is made from 1/8-inch o.d. aluminum tubing, while the support and balun are made from 3/16-inch tubing. These diameters are the maximum permitted without excessive shadowing of the solar panels. In fact, the dipoles were originally designed using 1/16-inch tubing, but this proved unsatisfactory from a mechanical standpoint. A coaxial feed [labeled (a) in Fig. 36] was run inside one leg of the support, the inner diameter of the tubing forming the outer conductor of the coaxial line, and the inner conductor was soldered to the other arm of the dipole. Rather than place reliance on a mechanical joint, this solder contact was a precaution to prevent the generation of intermodulation products on the flight model. For the same reason, the entire unit was gold-plated. Bonding a fiberglass support [(b) in Fig. 36] across the feed point ruggedizes the unit. As can be seen, the coaxial line extends past the mounting flange [(c) in the photograph] to the inside of the satellite, where the connector permits the mating with standard coaxial line.

Protruding from each end of the dipole is a piece of rubber tubing [(d) in Fig. 36] approximately 1-inch long. In the course of the dipole mechanical design, a dipole had been shaken several times but never mounted on the satellite. The first shake test of the dipoles in their normal position on the satellite proved disastrous. Some of the lower arms of the bottom row of dipoles fell off because the dipole and satellite resonant frequencies were too close. This was solved by damping the dipoles to reduce the amplitude of vibration — hence the addition of the rubber tubing.

With the mechanical details completed early in the design, the only parameter left to assist in the adjustment of the electrical characteristics was a small variation in length.

An array of 16 dipoles was built and mounted on a sheet-metal model of LES-6 (Fig. 37). This permitted development of the two orthogonally polarized antenna elements simultaneously, since the slot development was proceeding on a separate antenna model which resembled the flight model quite closely. As indicated in the Introduction (Sec. 1), 16 equally spaced beams are formed by feeding two adjacent pairs of collinear elements and then successively switching a phase delay through the elements. No adjacent pair would ever be fed in phase. A sufficient delay was inserted to scan the beam $\pm 11\text{-}1/4°$ around the in-phase position, as explained in Sec. IV-A.

    1. Patterns and Directivity

       a. Theoretical

Formulas for the radiation patterns of dipoles around a cylinder are given in Ref. 4. Modifying the formulas given for an array of vertical dipoles (Fig. 38), to make a more general expression capable of solution with varying amplitude and phase of excitation as well as the number of tiers of dipoles, gives

$$E_\theta = \left| \chi \sin\Theta \sum_{m=0}^{N-1} A_m e^{j\beta m} \left\{ V_o + 2 \sum_{n=1}^{\infty} j^n V_n \cos[n(\varphi - m\Delta\varphi)] \right\} \right| \tag{27}$$

16

where

$$V_o = J_o(kb \sin \Theta) - \left[ \frac{J_o(ka \sin \Theta)}{H_o^2(ka \sin \Theta)} \; H_o^2(kb \sin \Theta) \right]$$

$$V_n = J_n(kb \sin \Theta) - \left[ \frac{J_n(ka \sin \Theta)}{H_n^2(ka \sin \Theta)} \; H_n^2(kb \sin \Theta) \right]$$

$$\chi = \frac{\sin\left(\frac{\ell kS}{2} \cos \Theta\right)}{\sin\left(\frac{kS}{2} \cos \Theta\right)}$$

$$k = \frac{2\pi}{\lambda} \; (\lambda = \text{wavelength})$$

$\ell$ = number of tiers

N = number of dipoles

$A_M$ = amplitude (voltage) of the excitation of the $m^{th}$ element

$\beta_m$ = phase relationship (radians) of the $m^{th}$ element.

The directivity is calculated by

$$D = \frac{|E(\Theta_o, \varphi_o)|^2}{\left| \sum_{p=0}^{N-1} \sum_{m=0}^{N-1} A_m A_p r^{j(\beta_m - \beta_p)} \int_0^{\pi/2} \chi^2 \sin^3 \Theta Z \, d\Theta \right|} \tag{28}$$

where

$$\Theta_o = \frac{\pi}{2}$$

$$\varphi_o = \frac{N-1}{2} \cdot \Delta\varphi$$

$$Z = |V_o|^2 + 2 \sum_{n=1}^{\infty} |V_n|^2 \cos[n\Delta\varphi(p-m)] \quad .$$

These formulas were programmed for an IBM 360 computer; the Appendix of this report contains the program and a sample printout. The calculated half-power beamwidths for a 2 × 2 array were 32° × 58°, and the directivity was 12.52 db at the transmit frequency.

b. Measurements

Antenna radiation patterns were measured at the Lincoln Laboratory Antenna Test Range in Lexington, on several outdoor ranges, as well as in an anechoic chamber. The measured half-power beamwidths (HPBW) at the transmit frequency were 34° × 54°. The product of the beamwidths is within 1 percent of the theoretical. Complete pattern data at other frequencies will be given in the section on flight performance (Sec. V). Patterns of each dipole element (Fig. 39) appeared at the location expected, but in the equatorial plane they were considerably narrower than calculated, 70° HPBW vs 114° HPBW (mutual couplings are ignored in the calculation), and flat-topped with large shoulders. When two pairs of dipoles were fed, the phase delay required

17

to position them at the desired location, $\pm 11\frac{1}{4}°$ about the in-phase condition, was about 60° rather than the calculated 40°. Also, the manner in which the pairs are fed (see Sec. IV-A), that is through a fixed 90° hybrid, means that as the frequency is increased, the phase difference becomes less rather than increasing as required to keep the beam pointing constant. For this reason, the receive frequency performance is somewhat compromised to optimize operation at the transmit and beacon frequencies. In addition, the computer program indicated only a 0.05-db difference in directivity between the in-phase condition and the scanned, whereas the measured difference was 0.7 db. Despite these difficulties, the measured gain of the antenna model is reasonably close to that predicted. Four elements were fed with appropriate matching devices, and the gain was measured at one of the outdoor ranges. The gain was 11.8 db and the calculated losses were 0.4 db in the matching devices, resulting in a directivity of 12.2 db. As a check of the measurements, the gain of a 4-element array was also measured at 265 MHz where the dipoles were inherently matched; therefore, no matching devices were required. The directivity here was also 12.2 db.

### 2. Impedance

Figure 40 shows the admittance of a single dipole at its input when it is excited in phase with three other dipoles, and the other twelve are terminated in open circuits at the connector [see Fig. 36, callout (c)]. This configuration was used consistently during the development, since varying the termination of the unused dipoles had little effect on the basic impedance of the one being measured.

In matching this admittance, there were two philosophies which were considered: first, to reduce the VSWR at the transmit-beacon frequencies to the lowest levels, allowing the receive and radiometry-band RFl to fall where they may; or second, to match at the transmit and receive frequencies and accept the resulting mismatch at other frequencies. The second philosophy was deemed to be the more advisable. This was accomplished by adding two stubs each about $\lambda/8$ long. Results of adding the first (open-circuited) stub are shown in Fig. 41. Then, a short length of 50-ohm transmission line is used before the second (short-circuited) stub is added.

Figure 42 shows the effect on the impedance of adding the appropriate phase delay to scan the beams. The flight dipoles showed the same basic impedance characteristics as the development models and, because of their very simple nature and the ruggedness of their construction, they were very similar to one another. This made it possible to mass-produce and install the matching network, or to replace damaged dipoles without perturbation of the final VSWR.

### C. Cavity-Backed Slots

Development of the cavity-backed slot antenna elements began where the LES-5 development ended. Comparison of Fig. 1 of this report with the corresponding figure in the LES-5 report[1] reveals the major differences between the slot elements for the two satellites. On LES-6, the slots are completely formed by the edges of the solar panels, whereas previously (in LES-5) they were formed partly by solar panels and partly by the extensions on each end of the satellite. Thus, while the slots on LES-5 were terminated by adjustable shorting strips on the extension panels, those on LES-6 could not easily be short-circuited in this manner due to the difficulty of fastening to the solar panels. The slots were therefore made maximum length, and the length was not adjustable.

## 1. Impedance

Figure 43 shows the impedance of a single LES-6 slot at its center. Comparison with Fig. 6 of the LES-5 report[1] shows that the LES-6 impedance at 240 MHz is about the same as it was at 280 MHz for LES-5. This is consistent with the fact that the LES-6 slot is about 15-percent longer than the LES-5 slot. Over the frequency range of interest (240 to 315 MHz), the impedance changes rapidly, as shown by Fig. 43.

After calculating the effect of several matching networks and experimentally trying one that involved the use of only commercially available parts, the decision was made to use a pair of co-axial cavities. One cavity would be as close to the feed point as practical, and the other would be placed where necessary to accomplish the desired match. As with the dipoles, the goal was to attain a good match at the transmit and receive frequencies.

Figure 43 was plotted from data obtained by measuring a single slot on a 16-slot, full-scale antenna model with all the other slots open at the feed point. Therefore, it is close to being the self-impedance of a single slot. Mutual-coupling effects are complicated by the fact that in actual operation the termination of each of the eight slot pairs depends on the electronic switch which scans the beam. This switch (identical with that used for the dipoles) was discussed in Sec. IV-A. As with the dipoles, upper and lower slots are fed in phase as collinear pairs; then, each pair is connected by coaxial transmission line to the switch, which causes the line to be terminated either in an open diode or through a conducting diode to the triplexer.

Since the radiated beam is formed by exciting two adjacent collinear slot pairs, the total impedance of each active slot is the sum of its self-impedance and the mutual impedance due to coupling with the adjacent active slot and all the inactive slots. This is further complicated by the fact that two beam positions are obtained from each set of adjacent slot pairs by exciting them in two different phase relationships.

## 2. Initial Radiation-Pattern Measurements

Two adjacent slot pairs of the antenna model were prepared for radiation-pattern measurements by matching the individual elements to 50 ohms at the transmit frequency using appropriate stubs. All the other elements were terminated in adjustable-length, open-circuited lines as explained in Sec. IV-A. Equatorial-plane radiation patterns were then measured and recorded at the transmit frequency for the two adjacent slot pairs fed in phase. The lines to the unused slots were adjusted in length to get the narrowest (most directive) beam from the in-phase slots. This takes advantage of the mutual coupling between slots to get the highest gain possible at the transmit frequency. Variation in beamwidth was considerable as the "unused" line lengths were changed. Half-power beamwidths varied between 50° and 70°, as indicated by Fig. 9.

With the unused line lengths set for the narrowest beam, enough phase delay (40°) was introduced between the feed point and one slot pair to shift the beam the desired $11\frac{1}{4}°$. It was then inserted between the feed point and the other slot pair, where it shifted the beam $22\frac{1}{2}°$ from the first. This test proved the feasibility of the basic scanning system, and also permitted calculation of the desired impedance "seen" by each unused slot, looking back to the switch. From this, the correct line length between the finally matched slot and the switch terminal was calculated to get the maximum possible directivity from the radiating set of slots at the transmit frequency. This was necessary if the level of slot radiation were to even approach that of the dipoles.

Theoretically, for perfect circular polarization, the gain of the slots and dipoles should be equal. Actually, as borne out by the experience with LES-5, these slots are relatively inefficient

19

radiating elements. On LES-5, they compared favorably with the dipoles only because mechanical considerations forced the use of the more inefficient full-wave dipoles. With half-wave dipoles, it was expected that the gain of the slots would be about a decibel less than that of the dipoles.

### 3. Matching Networks

Calculations showed that matching-network loss for the slots could be reduced by about 0.5 db by using coaxial-cavity matching devices rather than conventional open- or short-circuited stubs. This was based on using 0.5-inch-diameter air dielectric, 50-ohm coaxial line for the cavities as against 0.141-inch-diameter teflon, 50-ohm coaxial lines for the stubs. In either case, all interconnecting cable would be 0.141-inch teflon line.

Initially, for test purposes, the coaxial cavities were made of 0.5-inch o.d. thin-wall, brass-tube outer conductors and 3/16-inch o.d. brass-tube inner conductors which, with air dielectric, formed 50-ohm coaxial lines. Each cavity was short-circuited at one end, open at the other, and tapped in-between. One cavity shunts each slot, at the feed point. This cavity is resonant at a frequency between transmit and receive, and the tap is such that the combined admittance of the cavity-backed slot and the coaxial cavity is real at both transmit and receive.

Figure 44 shows the measured slot admittance at the transmit and receive frequencies, with points marked A taken from Fig. 43. Also shown is the calculated admittance at each frequency, with the first coaxial cavity shunting the slot; these points are marked B. Note that both admittances are pure real (on the axis) and, in fact, the admittance at receive represents a match to 50-ohm line. At the end of about 5 inches of 50-ohm, teflon-dielectric coaxial line, the admittance at transmit is shown by point C (while at receive it is still matched, of course). This is where the second coaxial cavity is placed across the line. The second cavity is theoretically resonant at the receive frequency, to preserve the match, and it has enough negative susceptance at the transmit frequency to achieve a match here also. Figure 45 shows the theoretical variation of susceptance with frequency for the two cavities discussed above.

Coaxial cavities have some important advantages over stubs as elements of matching networks. To accomplish the same thing with stubs, they would have to be relatively long (several multiples of 1/2 or 1/4 wavelengths) or of very high or low characteristic impedance because the two frequencies at which a match is desired are quite close to each other, and the needed susceptances are of opposite sign at the slot feed point. Either long stubs or very high or low characteristic impedance would result in higher losses and lower power-carrying capability. The longest coaxial cavity would be less than 1/4 wavelength at the lowest frequency of operation (transmit) and the characteristic impedance could be 50 ohms, which is a good compromise between the optimum for low attenuation and high power-carrying capacity.

When test coaxial cavities were actually installed on the antenna model slots, the measured impedances were close to those calculated. However, matching of the final flight-model slots was complicated by several factors, some of which were anticipated and some unexpected. As pointed out in Sec. IV-C-1, the measured slot impedance upon which the calculations of the matching network were based was essentially the self-impedance of a single slot. Experience with LES-5 indicated that the impedance would differ from slot-to-slot due to variations in the mechanical structure. As on LES-5, the backup cavity for an upper slot is a little longer than for a lower slot because of the equipment platform just below the viewband. This is about an inch thick and the necessary volume is taken from the lower backup cavities. Thus, the top slot impedance is

different from that of the bottom. Also, on LES-5 the slot impedance was measurably different with the final solar panels in place than with the dummy panels that were in place for all but the final tests. Three parameters were made adjustable on the LES-5 slots to allow for trimming the slot impedance to get the desired match despite the aforementioned variations; one of these parameters was the slot length. On LES-6, the slot length is fixed.

### 4. Mutual-Coupling Effects

On LES-5, the effect of mutual coupling between all the slots was ascertained by measuring the total impedance of one slot while all the others were excited equally and in phase. This quantity could not as easily be measured on LES-6 as twelve of the slots are inactive, while four are active and the mutual coupling depends upon the unused line length as demonstrated by the effect of the unused lines on the radiation patterns, described in Sec. IV-A-1-b. Also, the phase of the mutually coupled energy depends upon the phasing between the adjacent active slots, and this is switched for beam-scanning purposes. Therefore, the procedure adopted was to find the self-impedance at each of the two important frequencies that would result in the best match in actual operation (including the mutual-coupling effects), taking into account the fact that at each frequency the impedance would be different for each of the two beam positions obtained with each set of adjacent slot pairs.

On LES-5, the dipoles had no measurable effect on the slot impedance; therefore, much of the LES-6 development was accomplished using separate antenna models for the slots and dipoles. When dipoles were mounted on the slot antenna model, they were found to have a marked effect on both the impedance and the radiation patterns of the slots. This was unexpected, but eventually explainable in terms of the difference in mechanical design between the LES-6 and LES-5 dipoles. Refer again to Fig. 1 and note that each dipole support constitutes a pair of parasitic radiators directly over the middle of each slot and polarized in the same direction as the slot field in which it is immersed. This is, of course, much different than the LES-5 configuration in which the dipoles were supported at the short-circuited ends of each slot. There was no measurable difference in the LES-5 slot impedance with and without the dipoles; if there was any difference in the radiation patterns, it was not noticed because the patterns were omnidirective.

When the dipoles were first mounted on the antenna model, the change in slot impedance was noted immediately since the VSWR at the transmit and receive frequencies increased to 1.7 from <1.2 for a slot pair fed in proper phase with an adjacent slot pair. Equatorial-plane radiation patterns revealed that the beams were all shifted about 8° from where they were with no dipoles. This will be covered in more detail when the radiation characteristics are discussed in Sec. V-B.

### 5. Flight Matching Devices

Coaxial matching cavities for the flight-model satellite were quite different from those used on the antenna test model. Calculations indicated that the spacing between the inner and outer conductor might be large enough to permit multipactor voltage breakdown[5] to occur. Although 0.5-inch-diameter coaxial cavities passed an RF power test in $10^{-6}$-torr vacuum with no evidence of multipactor, the design was considered marginal and the flight-model cavities were reduced in diameter so that the spacing between the inner and outer conductor would be less than 0.1 inch, making the frequency-spacing product <70 MHz-cm, a value that should insure freedom from multipactor effects.

For mechanical reasons, a major change in the cavities was made which resulted in somewhat different electrical behavior. Figure 46 is a photograph of one of the first coaxial cavities which shunts a slot at the feed point. Instead of being a straight length of coaxial line, as the test cavities, this is a "folded" cavity; i.e., the coaxial line is, in effect, folded back on itself at the tap between the open- and short-circuited ends so that they both point the same way. This permits the first coaxial cavity to be mounted in the channel section between slot backup cavities with the ends pointing toward the viewband. A feed probe (seen in the lower part of the photograph) is tapped off the inner conductor; this probe projects into the backup cavity near the center of the slot, where it is soldered to a gold-plated feed tab in contact with the inner surface of a solar panel.

The main reason for folding the coaxial cavities is to permit easy access to the tap point for making the connections. Access is provided by a removable cover plate on the bottom of the unit shown in Fig. 46. Undercut pieces of teflon dielectric fill the transition region in such a way as to prevent multipactor voltage breakdown. Without solid dielectric, the geometry is such in this region that multipactor would occur.

Additionally, folding allowed the first coaxial cavities to be mounted in the channel sections without making holes in the fiberglass support rings, which would have been necessary to accommodate straight coaxial cavities. Such holes would have weakened the structure considerably. Also, since all the coaxial cavities (second as well as first, upper and lower) point toward the viewband, they help keep the satellite center of gravity close to the geometrical center.

At the bottom of the photograph, the input connector to the coaxial cavity can be seen; this is a miniature OSM-type panel jack. At the top can be seen an adjusting screw that varies the value of a re-entrant capacitor, which has the effect of changing the length of the open end of the coaxial cavity. In the version shown by Fig. 46, the length of the short-circuited end is not adjustable, and both open- and short-circuited ends are air-dielectric lines. Figure 47 shows the final flight version of the coaxial cavities; in this version, the short-circuited end is a length of semi-rigid, 0.141-inch-diameter teflon dielectric, 50-ohm line with an OSM plug on one end and a shorting cap on the other. Thus, it is a replaceable short-circuited stub which can be changed to another length, if necessary. This provides another adjustment in case the slot impedance with the flight solar panels is different enough from that with the dummy panels to be beyond the range of the adjusting screws.

Semi-rigid, 0.141-inch-diameter teflon line was used between all the RF components of the antenna system; the characteristic impedance is 50 ohms. A 27-inch length was used to connect each upper-slot matching network to that of a corresponding lower slot to obtain eight sets of in-phase collinear pairs of slots. This length was chosen to minimize the unavoidable large mismatch at the high end of the RFI band, and was also made long enough to go from the coaxial cavity to the viewband and around any components that might be mounted in the vicinity. However, this length was chosen before the final design was known, and it turned out that there were no components around which the lines must be bent. Therefore, a relatively long loop was made in each line to take up the excess length. This can be seen in Fig. 48, which is a photograph of the inside of the upper array and shows the mounted coaxial cavities and associated feed lines. When the two arrays (upper and lower) are assembled to the viewband, the upper and lower feed lines are connected in parallel pairs by means of an OSM power divider or tee connector for each pair. The resulting 25-ohm level is compensated back to 50 ohms with a short length of line and an open-circuited stub, as seen in Fig. 49 which shows the inside of the viewband above the equipment

platform with a matching stub on the left side of the photograph. Another OSM tee connects the open-circuited stub to the short length of line, and the remaining terminal is the 50-ohm output of the collinear slot pair. Eight semi-rigid lines connect these terminals to the slot switch in a configuration similar to that used for the dipole pairs. These lines run alongside the dipole lines on the eight support struts for the thermal blanket and terminate on a distribution ring in the center of the satellite. From here, shorter lines connect to the diode switch terminals.

### 6. Intermodulation

The most persistent problem associated with the slot antenna elements is the generation of intermodulation (IM) noise at points of electrical contact in the backup cavities. IM noise results from mixing two or more frequencies in a nonlinear or semiconducting medium, as explained in Sec. IV-A-5-a. In the specific case of LES-6, mixing transmit and beacon RF energy in a non-linear conductor can result in a harmonic very close to the receive frequency. When generated, IM can seriously reduce the sensitivity of the transponder receiver.

Design and fabrication procedures for preventing IM consisted mainly of gold-plating all contact surfaces, cleaning them before assembly, and assembling them in close contact in a clean environment. In this way, the formation of nonlinear coatings (such as oxides) would hopefully be prevented. Extensive testing indicated that clean, gold contact surfaces would be relatively free of IM. Measurement techniques were developed which permitted the detection and identification of IM products as low as −140 dbm over the frequency range of interest. As described in Sec. II, the slot backup cavities result from dividing the annular space between the inside mesh panels and the solar panels. Reference to Fig. 1 will reveal how the solar panels are fastened to the support structure. Each panel is held on by a row of bolts along its top and bottom edges. These fasteners also serve to force the gold-plated electrical surfaces into intimate contact. All the inside mesh panels are similarly fastened except that they are bolted along all four edges of each panel. Tests have demonstrated that any IM produced at the bolt-fastened joints is below the −140-dbm power level.

Reference to Fig. 1 again will reveal that the two edges of each solar panel which form the slot antenna elements are not fastened with bolts. Instead, electrical contact is established by the use of gold-plated, spring fingers which press against the gold-plated inside surface of the panels. This finger-type contact proves to be a source of IM, probably because contact pressure is much less than that developed by the bolts.

Each of the slots was tested for the generation of IM noise with representative amounts of transmit and beacon power. For some slots, the IM closest to the receive frequency had a power level in excess of −100 dbm. This was found to be generated in the finger contacts. A marked reduction in the IM level, down to −140 dbm, was obtained by burnishing the contact surfaces by inserting clean paper between the contact fingers and the solar panel and moving the paper back and forth to polish the surfaces. The theory behind this procedure was that the microscopic surface would be modified by the burnishing action of the paper. Nonlinear coatings would be removed, but the paper is not abrasive enough to damage the very thin gold plate.

Unfortunately, the effects of burnishing appear to be short term, since the IM returned generally after a few days in the space laboratory environment. Tests in a simulated space environment were not made on the satellite, as a suitable vacuum chamber was not available. A shielded, anechoic vacuum facility would be required, and the Lincoln Laboratory vacuum chamber is not large enough to provide such an environment.

A 1-foot long section of solar panel substrate, with finger stock in contact, was constructed to simulate a section of the backup cavity small enough to fit into an 18-inch-diameter bell jar which could be evacuated down to $10^{-6}$ torr. Suitable connectors were provided for feeding RF energy through the contact fingers and the panel to a dummy load. With this setup, a series of tests were conducted at pressures of 1 atm and at $10^{-6}$ torr.

First, at room pressure, 90 watts of RF power at the transmit frequency and 6 watts at the beacon frequency were fed through the test piece to obtain IM noise of the same frequency and power level as occurred in the satellite. Then, the surfaces were burnished using paper. IM was found to be reduced below $-140$ dbm, at room pressure. Next, the bell jar was evacuated to less than $10^{-6}$ torr and the IM increased to about the $-110$-dbm level. Beacon power was then reduced by 10 db and IM dropped to $-140$ dbm. This demonstrated that a possible remedy might be to reduce the beacon power.

After the beacon power was increased to normal and the high IM was observed again, the transmit power was increased to about 160 watts. After about 8 hours of this higher power, it was reduced to the normal 90-watt level and the IM was found to be reduced below $-140$ dbm. Transmit power was increased to about 110 watts to make the IM observable at greater than $-140$ dbm. This experiment suggests the possibility that the RF energy may modify the contact surfaces, in a vacuum, eliminating the nonlinear material and the associated IM noise. In orbit, with all transmitters turned on, the generation of IM noise did not prove to be a problem. Some effects of IM were noted when the beacon was first turned on. These effects were intermittent and soon dropped below the level at which they could reduce the receiver sensitivity. At no time did they impair the operation of the communications link.

## D. Telemetry Antenna

A telemetry system is used in LES-6 to supply diagnostic information on the internal state of the various satellite subsystems. Also, it verifies that ground commands to the satellite have been received and executed properly. Because of the experimental nature of the main antenna system, a highly reliable separate telemetry (TLM) antenna was desirable (see the block diagram in Fig. 3). Then, in case of a malfunction in the main antenna system, diagnostic data could be obtained and hopefully used to correct the malfunction, if possible, or at least applied to learn something about its nature and cause. A simple monopole placed on the spin axis, located over a ground plane at the top of the satellite (Fig. 2) was finally chosen as the best antenna which met all the conflicting requirements. The monopole has a linearly polarized doughnut-shaped radiation pattern with approximately isotropic gain in the equatorial plane. This gain, though low, is adequate for the intended usage.

The ground plane consists basically of a perforated solid sheet of aluminum, 0.020 inch thick. The amount of material removed from the sheet is a compromise between limiting the shadowing of the back of the solar cells and other sensors, and providing enough material to withstand the shock and vibration of the launch and ejection sequence, while also providing a suitable RF reflecting surface with low leakage. The ground plane is fastened at the periphery to the top fiberglass ring of the satellite, and is also supported at the center by the bipod assembly. All electrical contacts to the ground plane are gold-plated to help eliminate possible nonlinear contacts and IM noise.

The monopole has been designed to be readily removable by first removing four screws from the mounting flange which holds the monopole to the bipod, and then unscrewing the RF connector

at the monopole base. This removal is often necessary due to some space limitations in the handling, testing, and shipping of the satellite. The monopole was made as long as possible, but is still only $0.2\lambda$ long at the telemetry frequency. Consequently, the input VSWR was about 5:1. The antenna was matched by using a short-circuited stub about $2\frac{1}{2}$ inches long located about $2\frac{1}{2}$ inches from the input connector.

The matching stub and feed line are semi-rigid, 0.141-inch-diameter, teflon dielectric, 50-ohm coaxial cable, as commonly used elsewhere in the satellite antenna system. The final input VSWR was about 1.1 measured at the telemetry frequency.

A longer monopole could have been used ($\sim 0.25\lambda$) if it were made of a stiff flexible material, say similar to the common metal tape measure, and then bent over to minimize the projection from the satellite top. This probably could have eliminated the need of a matching stub, but would have introduced the problem of deploying the tape after the satellite was in orbit. The simple fixed monopole was finally selected because it was inherently more reliable than any deployable antenna.

The monopole structure is essentially a tube of stainless steel about $\frac{3}{8}$ inch in diameter with 0.006-inch wall, copper and gold plate for low loss and ease of soldering, mated to the center conductor of a "TNC"-type panel jack (the details are shown in Fig. 50). The assembly is held rigid by a dielectric shell which is epoxied to the tube and then bolted to the connector and mounting flange. The monopole tube, as well as the ground plane, is painted with a special white "thermal" paint which helps control the orbital temperature of these components.

The flight-model TLM antenna patterns for the polar and equatorial planes are shown in Figs. 51(a) and (b). These patterns were not at all sensitive to the monopole length, for lengths $\leqslant 0.25\lambda$. The pattern peak occurs about 45° off the equatorial plane; this is typical for monopoles on small ground planes. Measured gain of the TLM antenna system, referenced to the output of the TLM filter (does not include filter loss), is about $-1.8$ db. The variation in equatorial gain due to satellite spin is about $\pm 0.3$ db.

Coupling from the TLM antenna to either the slots or dipoles is $< -30$ db at all the frequencies of interest. This decoupling effectively prevents undesirable interactions between the $f_T$, $f_B$, $f_R$, and TLM functions.

### E. Hybrid Power Divider

To produce the required circular polarization, the slot and dipole arrays must be excited with equal amplitude signals having a 90° phase difference. A convenient way to do this is to use the 90° hybrid for both the power division and phase shift. The hybrid also provides some protection in case of failure in one part of the antenna system. The unit chosen is essentially the same design as used in LES-5, with the connectors changed to a miniature type. Figure 52 shows the hybrid performance, and a photograph of the unit is shown in Fig. 53. The advantage of using a proven, space-qualified unit is obvious; also, much development time was saved by adopting the existing design.

Initially, only the antenna hybrid was used in the LES-6 feed system. The power division at the switch input was accomplished by using a matched tee power divider built in stripline as an integral part of the switch itself. However, it was found that this design was quite sensitive to antenna mismatch and produced poor performance, especially at the beacon frequency. It was then decided to use a separate power divider (the 90° hybrid again) and eliminate the tee divider from the system. This has worked well in providing a power split to the switch which is independent of the mismatch of the antenna elements. This arrangement is also more convenient for

experimental purposes since the line lengths needed to scan each beam properly can be changed easily, whereas with the former arrangement, modification of the whole switch unit would be required. These switch hybrid power dividers also help isolate the effects of any possible failure on one side of the antenna system in a manner similar to that previously explained for the antenna hybrid.

### F. Phasing Network

The philosophy used in designing the LES-6 antenna matching devices was to try to minimize the insertion-loss characteristic and then to set the final phase difference needed for a good axial ratio by adjusting various line lengths. However, when this was done, the performance of the transmit and receive frequencies was good, while the beacon and RFI bands were quite poor. This situation was caused by the necessity for using a long differential line length between the slots and dipoles, and hence a frequency sensitive arrangement to get the correct phase shifts at transmit and receive. Evidently, a matched network having low insertion loss and giving the appropriate phase shifts over the frequency band of interest was needed. Such an "all-pass" network or pure phase shifter can be constructed from a 3-db hybrid and two equal-length short- or open-circuited lines, as shown in Fig. 3. This device is well known and has had extensive use in microwave systems.[6]

There are many variables available in this method of phase shifting: the network can be placed either in the dipole or slot side of the system; the hybrid lines can be open- or short-circuited; and the length of the lines can be varied, along with their characteristic impedance levels. Also, more complicated sets of open- or short-circuited stubs can be envisioned to further increase the possibilities. A network giving the appropriate phase shifts at the transmit and receive frequencies was installed in the antenna model and adjusted for optimum performance. Satisfactory operation was achieved by placing the network in the dipole side of the feed system, and by using equal lengths of 50-ohm open-circuited stubs about 16 inches long. In addition, this network gave acceptable results at all the other frequencies of interest; consequently, further development of the many other possibilities was not considered worthwhile. The same 3-db hybrid as described in Sec. E above was selected again because of its availability and known performance.

### G. Loads

Each of the 3-db hybrids shown in Fig. 53 has a port which is normally decoupled (~20 db) from the input port. These ports, for the three hybrids in the system, must be terminated in loads to prevent spurious reflected signals being generated. Since the load requirements for the worst case of a failure condition might be about 50 watts, this sets the lower limit of the load dissipation. A commercial 120-watt conduction-cooled unit was selected as a compromise between size, weight, and power dissipation. This load (Fig. 54) has TNC-type coaxial connector input, then transforms to a stripline on a beryllia substrate on which is fired the lossy resistive coating. Beryllia is an excellent thermal conductor and electrical insulator combined, and is used to conduct the heat to the body of the load. The input VSWR is $\leqslant 1.05$ for the frequency band of our interest. This load has been successfully qualified for flight, having been tested for high-power vacuum breakdown, heating effects, IM noise generation, shock and vibration, and thermally cycled from $-40°$ to $60°C$. The load is first attached to a small plate for convenience in final mounting and then finally bolted to the appropriate box or platform location. A thermally

26

conductive silicone rubber material, used extensively in the satellite, fills all the small gaps between the mountings and thus insures a low thermal resistance between the load and the final heat sink.

### H.   Triplexer

Each VHF band-pass filter of the LES-6 triplexer uses quarter-wave interdigital resonators with Chebyshev responses.  These resonators were designed from the low-pass prototype.[7]  Three filters were combined by appropriate lengths of line into a four-port configuration separating the transmit, beacon, and receive frequencies.  The triplexer arrangement is shown in Fig. 55.  The telemetry filter, a fourth unit, was used in a separate channel.  Because this design is exactly identical to the TLM filter used in LES-5 (a discussion of which can be found elsewhere[8]), this section will be concerned only with the transmit, beacon, and receive filters.[9]

#### 1.   Transmit and Beacon Filters

Optimum design for both the beacon and transmit filters proved to be a 5-element Chebyshev interdigital design with a 0.01-db ripple.  With 5 MHz separating the transmit and beacon frequencies, system specifications required approximately 40-db mutual rejection and a pass-band loss of $< 0.5$ db.  Because of the small separation between $f_T$ and $f_B$ and the requirement that the TLM frequency be isolated from the $f_T$ by 40 db, the unloaded Q had to be increased from the approximately 1200 (used in the receive and telemetry filters) to about 2400.  This made it possible to achieve the high rejection combined with the low pass-band loss at $f_T$ and $f_B$.  These frequencies were placed in the first null at the edges of their respective pass bands [see Figs. 56(a) and (b)], thus increasing the out-of-band rejection characteristics.

In LES-5, the transmit filter was filled with a low-loss polystyrene foam to prevent occurrence of the secondary emission resonance (multipactor) phenomenon.[5]  The same technique was attempted with the LES-6 transmit filter; however, the higher transmitter power (100 watts) combined with a larger filter volume resulted in a buildup of heat which destroyed the dielectric and resulted in a breakdown.  After experimentation with other low-loss dielectrics proved fruitless, the solution proved to be a filter sealed at a pressure of 1 atm.  A 90-percent nitrogen, 10-percent helium gas mixture was used to fill the filter, then a leak rate of $\approx 1 \times 10^{-8}$ cc/sec of helium at 1-atm differential was measured.  By assuming a constant leak rate, this assures sufficient pressure for at least 10 years, which is twice the 5-year design goal.

Since the beacon filter was designed to operate at a power level of approximately 10 watts, the multipactor problem was not as severe.  The only regions susceptible to multipactor at this power level are in the capacitive gaps at the ends of the resonant elements.  Multipactor was observed in the 2- to 5-watt range, and the solution was to retune the resonant rods with a shorter capacitive gap to prevent multipactor.

The measured response of both beacon and transmit filters exhibits $< 0.5$-db insertion loss in their respective pass bands and mutual rejections of $\sim 40$ db.  The transmit filter also rejects the TLM frequency by 40 db.  Figures 56(a) and (b) are plots of the measured triplexer response.  The difference between the $f_B$ and $f_T$ pass-band losses is attributed to the longer coaxial line between the beacon filter and the junction box.

Both filters are of aluminum construction, copper-plated for minimum loss, and then gold-flashed to inhibit corrosion.  Both beacon and transmit filters are approximately $18 \times 12 \times 2\frac{1}{2}$ inches.  The pressurized filter weighs 10.2 pounds, and the unpressurized filter weighs 7.6 pounds.

## 2. Receive Filter

The design technique for the receive filter is identical to that used for the LES-5 receive filter.  Several calculations of Chebyshev and equal-element configurations showed that the optimum design was a 7-element Chebyshev, with a ripple of 0.1 db, and the receive frequency at about the center of the 25-MHz pass band.  As seen in Fig. 56(b), the triplexer pass-band loss of this filter is approximately 0.5 db throughout the 25-MHz bandwidth.  At $f_R$, the measured loss is 0.4 db with a VSWR = 1.11.  Construction was in aluminum, copper-plated for low loss, then gold-flashed to prevent corrosion.  The filter is about 11 inches square by $1\frac{1}{4}$ inches deep, and weighs $\sim 3\frac{1}{4}$ pounds.

## 3. Triplexer Junction

The junction is a copper-plated, gold-flashed aluminum box on which four "OSM" panel jack connectors are mounted; then, the common junction is soldered together.  By adjusting line lengths $L_1$, $L_2$, and $L_3$ (see Fig. 55), the impedances of each filter at the critical frequencies were transformed to open circuits at the common junction.  $L_1$, $L_2$, and $L_3$ were experimentally adjusted to give the best overall performance at $f_T$, $f_B$, and $f_R$.

Figure 57 is a photograph of a completed flight-qualified triplexer assembly on a partial mockup of the satellite platform.  Two completely assembled triplexers were successfully subjected to thermal cycling, acceptance shock and vibration, and high-power vacuum testing.

## V. PERFORMANCE

### A. General

During the early stages of development, radiation characteristics were measured at Lincoln Laboratory's outdoor Antenna Test Range.  As explained in Ref. 1, this range suffered from reflection effects at the relatively low frequencies.  About halfway through the antenna development process, the Laboratory's new high-performance antenna test chamber was completed.  This facility, known as the Space Electronic Laboratory Anechoic Chamber, is shown in Fig. 58.  It is 85 feet long from the back wall of the 30-foot cubical test volume to the small end of the 54-foot long pyramidal taper.  The entire inside surface is covered with aluminum sheet, to provide shielding, and this is covered with pyramidal RF absorbers which reduce reflections by at least 35 db over the frequency range of interest.

Figure 59 shows the LES-6 antenna model, in the center of the test chamber, mounted on the dielectric support tower of the antenna positioner.  This is a Scientific-Atlanta azimuth-over-elevation positioner (Fig. 60) with a rotatable model support head on the tower.  Figure 61 is a close-up view of the antenna model mounted on the head.  A slip-ring assembly, which can be seen between the head and the model support, carries AC power to the switch circuitry,  The RF rotary joint to which a flexible coaxial cable is attached can also be seen in this view.  This cable is brought down the mast to a similar rotary joint in the azimuth axis of the positioner.  A close-up of the other end of the model (Fig. 62) shows the TLM stub antenna and its ground plane.  The tubular frame that was used inside the antenna model for support and stiffening is visible in some of these photographs.  It was not used in the flight model.

A high-gain, linearly polarized Yagi antenna is mounted on a polarization rotator in the small end of the pyramidal taper about 65 feet from the satellite model.  This is the transmit antenna used for measuring the response of the LES-6 antennas, which are reciprocal devices.  Patterns and gain are measured with the satellite receiving at all frequencies, including those at which

the satellite normally is transmitting. However, the effective radiated power (ERP) is measured by receiving energy transmitted by the satellite to the Yagi which is then used as a receiving antenna.

All the motions of the antenna positioner and the polarization device of the Yagi can be controlled and indicated at a console outside the anechoic chamber; this is also the data-recording center. RF power-generating, receiving, and measuring equipment is at this one location so that radiation patterns, polarization, gain, and ERP can be quickly and conveniently measured.

### B. Radiation Patterns

During the developmental phase, radiation characteristics of the antenna model were measured in the anechoic chamber. Principal-plane radiation patterns were recorded for the flight model shortly before it was transported to Cape Kennedy. Agreement was excellent between patterns obtained from the two models. With the satellite on the model support head of the antenna positioner, any conical pattern cut can be recorded by rotating the head. When the satellite spin axis is perpendicular to the line-of-sight between the model and the Yagi, a principal-plane pattern (the equatorial cut) can be recorded. Rotating the antenna positioner in azimuth results in a polar cut through a plane containing the spin axis, the plane being determined by the setting of the head.

Patterns were recorded in both the scan and omni-modes of operation. In the scan mode, the head was usually set so that a polar cut was through the maximum of a beam. Equatorial patterns were recorded of all 16 beams at each frequency during the last measurements made of the antenna model. When the flight model was measured, time did not permit the taking of such complete data, as the shipping date was imminent. However, all the performance data presented in this section are from the final flight-model measurements. Figures 63 through 69 show the radiation patterns for both modes of operation of the main antenna system.

At each frequency, the principal linearly polarized field patterns recorded are: the dipole field, which is polarized in the plane containing the satellite's spin axis; and the slot field, which is orthogonally polarized.

### C. Polarization

With the satellite transmitting, left- and right-hand field components were measured using a crossed-dipole antenna which was fed by a hybrid making both senses available. A right-hand helix antenna was used to check the crossed dipoles. These measurements confirmed the predominantly right-hand sense (IEEE definition) of the elliptically polarized radiation from the satellite at each frequency of interest: over the receive band, as well as the transmit and beacon frequencies.

Axial ratio, and its variation with angle, is shown by those radiation patterns recorded while the linearly polarized Yagi antenna was spinning about its polarization axis. This was done both in the scan mode (Figs. 63 through 66), and in the omni-mode (Figs. 67 through 69).

### D. Gain and Effective Radiated Power

Gain measurements were made by the substitution method using a dipole gain standard. This is a broadband dipole mounted on a plane reflector which provides a unidirectional radiation pattern and a gain comparable to that of the satellite antenna. Two of these gain standards were constructed to permit calibration by the identical-antenna method. One gain standard was mounted

| | East Edge of Earth (db) | Center of Earth (db) | West Edge of Earth (db) | Conus (7° North) (db) | Axiol Rotia | |
|---|---|---|---|---|---|---|
| Frequency | | | | | Minimum (db) | Moximum (db) |
| **Transmit (downlink)** | | | | | | |
| Goin | $8.6 \begin{smallmatrix}+ & 0.4 \\ - & 0.3\end{smallmatrix}$ | $9.8 \begin{smallmatrix}+ & 0.3 \\ - & 0.4\end{smallmatrix}$ | $8.0 \begin{smallmatrix}+ & 0.3 \\ - & 0.4\end{smallmatrix}$ | 9.4 | 0.2 | 4.4 |
| ERP* (wotts) | $679 \begin{smallmatrix}+ & 66 \\ - & 45\end{smallmatrix}$ | $895 \begin{smallmatrix}+ & 65 \\ - & 78\end{smallmatrix}$ | $592 \begin{smallmatrix}+ & 42 \\ - & 52\end{smallmatrix}$ | – | – | – |
| **Beocon** | | | | | | |
| Goin | $+7.1 \begin{smallmatrix}+ & 0.3 \\ - & 0.2\end{smallmatrix}$ | $+8.4 \begin{smallmatrix}+ & 0.2 \\ - & 0.3\end{smallmatrix}$ | $+6.9 \begin{smallmatrix}+ & 0.5 \\ - & 0.4\end{smallmatrix}$ | 8.2 | 2.3 | 5.5 |
| ERP* (wotts) | $17.8 \begin{smallmatrix}+ & 1.2 \\ - & 0.8\end{smallmatrix}$ | $24 \begin{smallmatrix}+ & 1.1 \\ - & 1.6\end{smallmatrix}$ | $17 \begin{smallmatrix}+ & 2.0 \\ - & 1.5\end{smallmatrix}$ | – | – | – |
| **Receive (uplink)** | | | | | | |
| Goin | $+8.5 \begin{smallmatrix}+ & 0.8 \\ - & 1.0\end{smallmatrix}$ | $+10.2 \begin{smallmatrix}+ & 0.3 \\ - & 0.3\end{smallmatrix}$ | $+8.3 \begin{smallmatrix}+ & 1.0 \\ - & 1.3\end{smallmatrix}$ | 9.9 | 1:6 | 5.7 |

**TABLE V**

**SCAN-MODE GAIN, ERP, AND AXIAL RATIOS**
(For scon made, motched right-hond circular polorizotion
goin; average of 16 beoms with voriation indicated)

\* These ERP volues ore colculoted for 26-volt bus voltoge or

Tronsmit power = 93.8 wotts
Beocon power = 3.48 watts

---

**TABLE VI**

**OMNI-MODE GAIN AND AXIAL RATIOS**
(All measurements in decibels)

| Frequency (MHz) | Lineor Goin Element 1 | | Motched CP Goin and Spin Voriation | Axiol Rotio | | Minimum Linear Goin |
|---|---|---|---|---|---|---|
| | Dipole | Slot | | Minimum | Maximum | |
| Transmit | −3.2 | −3.8 | −1.1 ± 0.7 | 1.8 | 6.0 | −7.2 |
| Beacon | −5.3 | −8.0 | −2.8 ± 0.6 | 6.6 | 9.0 | −12.5 |
| Receive | −3.1 | −3.3 | −0.7 ± 0.5 | 1.6 | 7.2 | −8.6 |
| RFIH | −2.4 | −12.2 | −1.5 ± 0.6 | 6.0 | 9.8 | −12.4 |
| RFIL | −4.2 | −9.3 | −3.5 ± 0.6 | 5.4 | 7.0 | −11.9 |

Telemetry Antenno:

Goin is −1.8 ± 0.3-db spin voriation in the equotoriol plane

At ±8° obove ar belaw the equotorial plone, goin is 0.5 db less thon obave volues

ERP — measured 0.64 wott

on the support tower, in the anechoic chamber, with its center of radiation where the satellite's radiation center would be when the satellite is mounted. RF energy was transmitted by the Yagi antenna, and the relative power received by the gain standard was noted at each frequency of interest. Reciprocity was verified by interchanging the transmit and receive functions of the Yagi and the dipole. When the satellite was substituted for the gain standard, the relative power received by the satellite antenna (at the same frequencies) was compared with that recorded for the dipole to calculate the gain of the satellite antenna. Measurements were made for each of two orthogonal polarizations at each frequency. Gain to matched polarization is the sum of the two linear component gains expressed as absolute ratios.

Unlike the LES-5 gain, which was calculated by using the range equations after measuring transmitted and received power and the distance between the antennas, a substitution method had to be used for LES-6 because the space loss in the anechoic chamber does not follow the simple inverse-square law of free space. The long, tapered, absorber-lined chamber behaves like a lossy waveguide, and propagation characteristics differ significantly from those of free space. Calibration of the gain standard dipole antennas was conducted at the outdoor Antenna Test Range where the inverse-square law holds true.

ERP was measured in the anechoic chamber. With the satellite transmitting, the power received by the Yagi was measured on a Hewlett-Packard HP-431C power meter that had been calibrated with an HP-8402A power standard.

Gain, ERP, and axial ratios are given in Tables V and VI. These values are referenced to the input of the hybrid shown in Fig. 3.

### E. Impedance

Individual antenna-element impedances were measured and the matching networks adjusted for a good match to the 50-ohm transmission lines at the two main frequencies, as explained in Sec. IV. At the transmit frequency, the VSWR was <1.3; at the receive frequency, it was <1.5.

Measurements were also made at the TLM antenna terminal and at the reference input (see Fig. 3) of the main antenna system for each beam position. These data are tabulated in Table VII.

| TABLE VII | |
|---|---|
| MAXIMUM MEASURED VSWR AT ANTENNA INPUT | |
| Frequency (MHz) | VSWR |
| Telemetry | 1.1 |
| Transmit | 1.2 |
| Beacon | 1.2 |
| RFIL | 1.7 |
| Receive | 1.5 |
| RFIH | 1.5 |

# VI. CONCLUSIONS

A sixth spin-stabilized experimental satellite, designed, built, and tested by Lincoln Laboratory, was placed in a synchronous orbit and successfully operated in several space communication applications.  The antenna system is the first circularly polarized, electronically despun, VHF transmit-receive array to be used on an orbiting satellite.

Maximum antenna gain, in the normal or scan mode of operation, is about 10 db.

REFERENCES

1. M. E. Devane, D. J. Frediani, B. F. LaPage, M. L. Rosenthal, and A. Sotiropoulos, "Antenna System for LES-5," Technical Report 451, Lincoln Laboratory, M. I. T. (18 July 1968), DDC 684167.

2. L. J. Ricardi, "Directivity of an Array of Slots on the Surface of a Cylinder," Technical Note 1966-52, Lincoln Laboratory, M. I. T. (10 October 1966), DDC 641959, H-748; also in Electron. Eng. 39, 578 (1967), DDC 668239.

3. R. L. Sicotte and R. N. Assaly, "Intermodulation Products Generated by a p-i-n Diode Switch," Proc. IEEE 56, 74 (1968), DDC 668721.

4. P. S. Carter, "Antenna Arrays Around Cylinders," Proc. IRE 31, 671 (1943).

5. "The Study of Multipactor Breakdown in Space Electronic Systems," Hughes Aircraft Company, NASA, CR-448 (July 1966); CR-71999, Vol. II (April 1965).

6. R. J. Mohr, "Some Design Aspects of Components Utilizing Symmetric 3 db Hybrids," Microwave J. 5, No. 6, 90 (1962).

7. S. B. Cohn, "Direct-Coupled-Resonator Filters," Proc. IRE 2, 187 (1957).

8. A. Sotiropoulos, "LES-5 Triplexer," Technical Report 438, Lincoln Laboratory, M. I. T. (31 August 1967), DDC 823174.

9. D. R. Bold and A. Sotiropoulos, "LES-6 Triplexer," Technical Report 459, Lincoln Laboratory, M. I. T. (2 December 1968).

Fig. 1. LES–6 flight model.

P202-2032



-60-7083-1

TELEMETRY
ANTENNA

GROUND PLANE

DIPOLE ANTENNAS

SOLAR PANELS

OPTICAL SENSOR
VIEWBAND

CAVITY-BACKED
SLOT ANTENNA
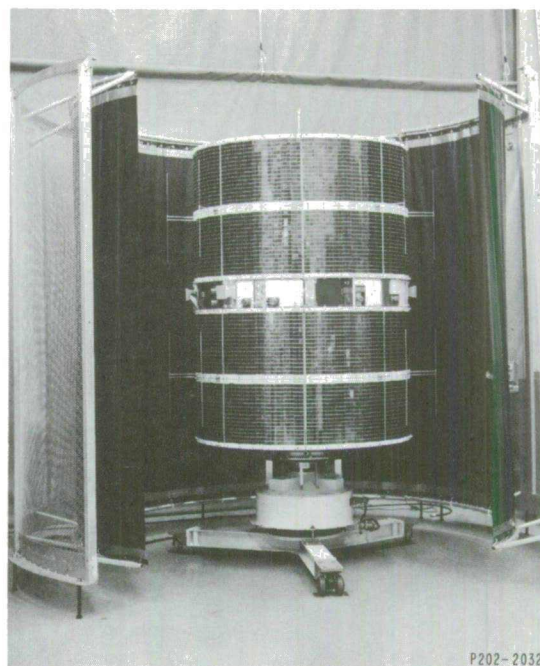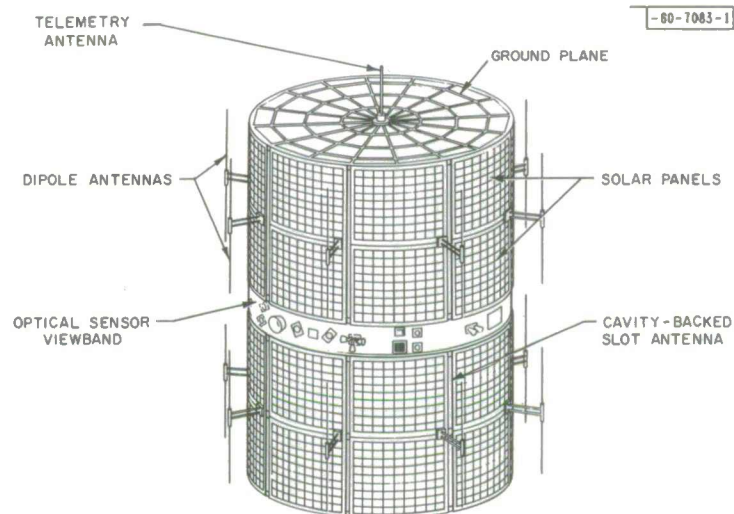
Fig. 2. LES–6 configuration.
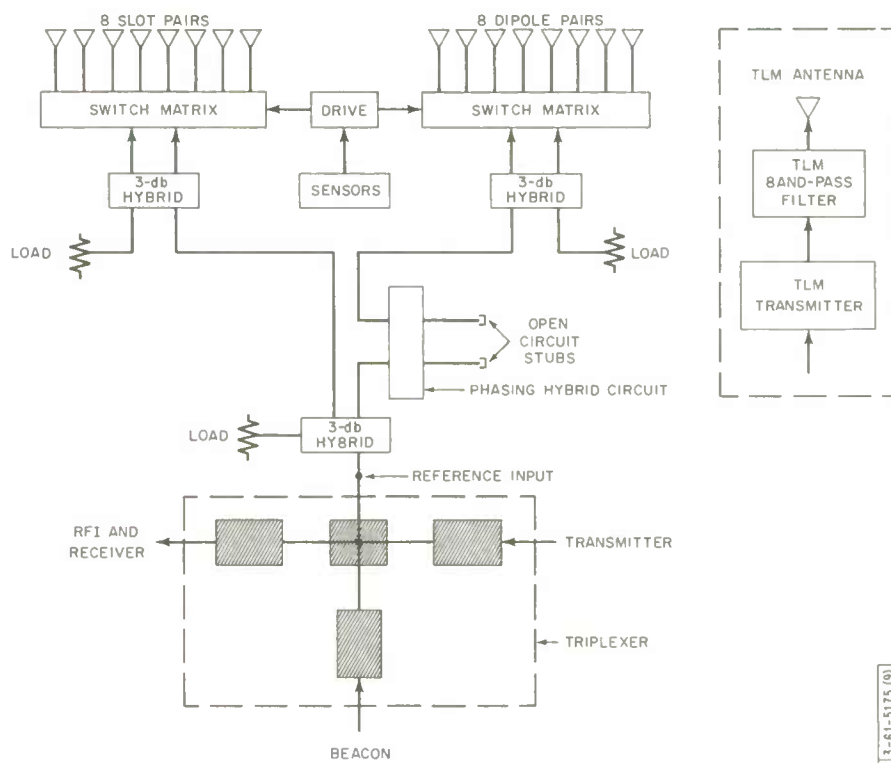
Fig. 3.  Antenna feed network.

3-60-8962-4

EAST EDGE

A

11.25°

8.5°

SATELLITE

Q

E

P    WEST EDGE

B

EARTH

r

h = 5.61r

N

SUBTENDED ANGLE 17°

54° HPBW

34° HPBW
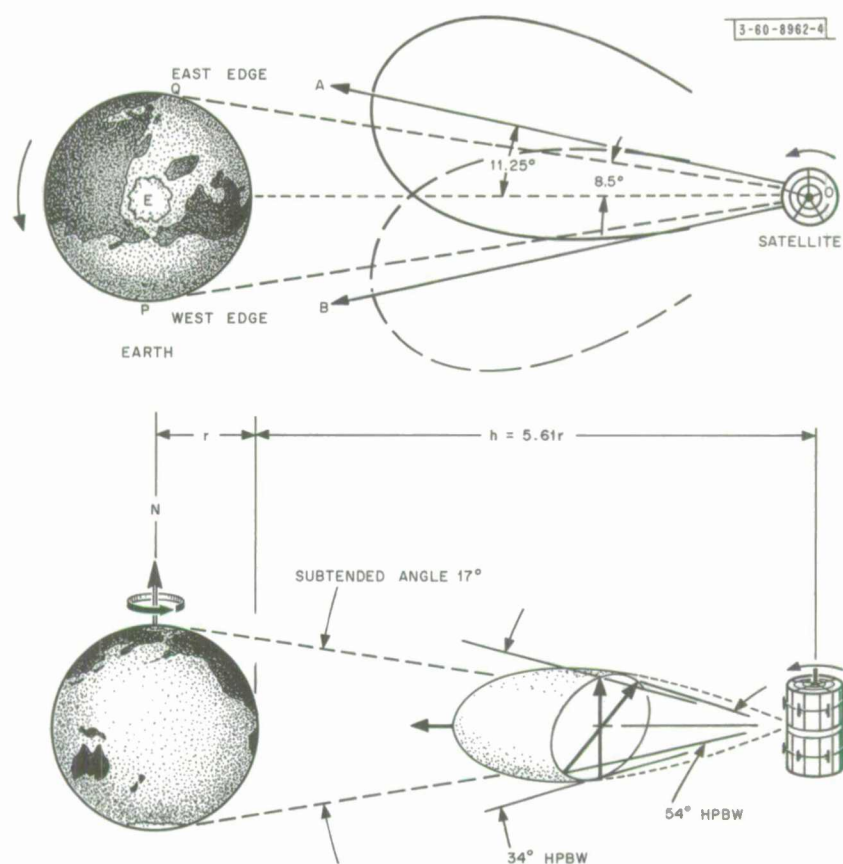
Fig. 4.  Earth illumination.



18-6-9683

$\Gamma$

$Q(\phi_0 - \theta_0, \theta_0)$

$\theta$

$\sigma$

$R(\phi, \theta)$

EARTH

O

$\phi$

$C(\phi_0 - \theta_0, 0)$

$P(\phi_0, 0)$
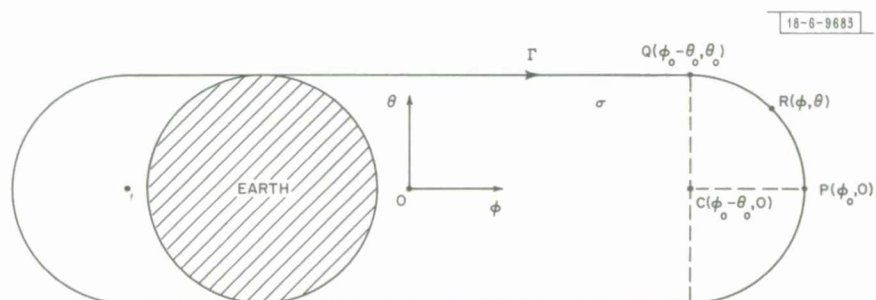
Fig. 5.  Geometry of pattern coverage.
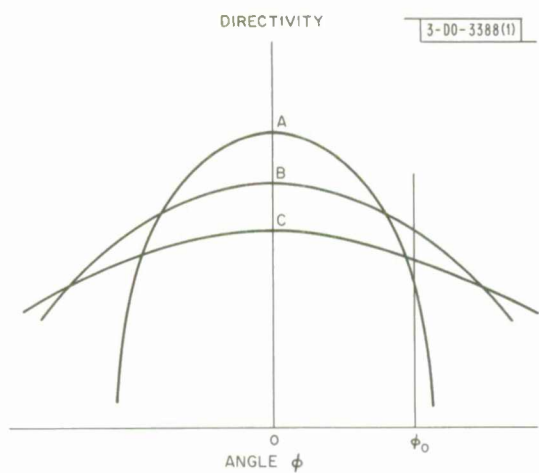
Fig. 6. Dependence of directivity on antenna pattern shape.
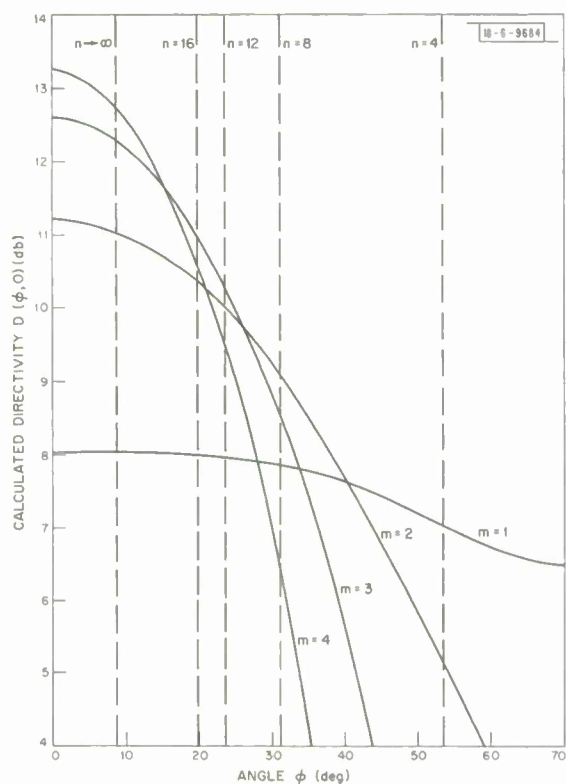


Fig. 7. Calculated directivity $D(\varphi,0)$ for four sets of excitations.
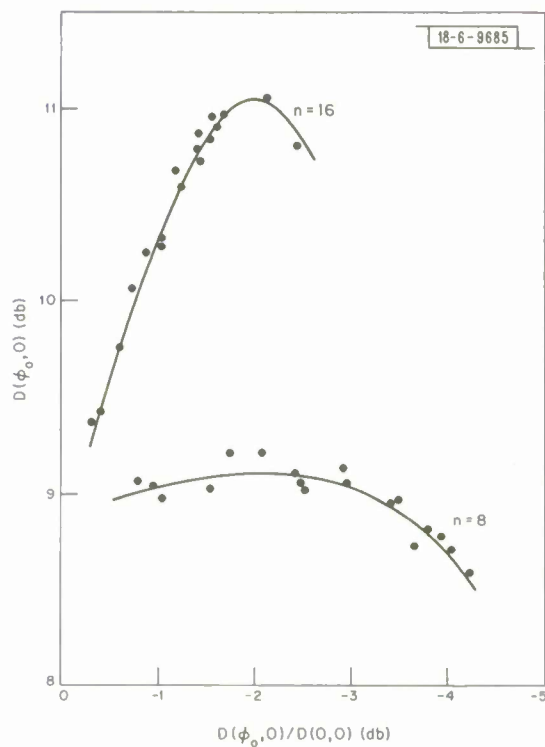


Fig. 8. $D(\varphi_o,0)$ vs $D(\varphi_o,0)/D(0,0)$ calculated for a number of patterns.
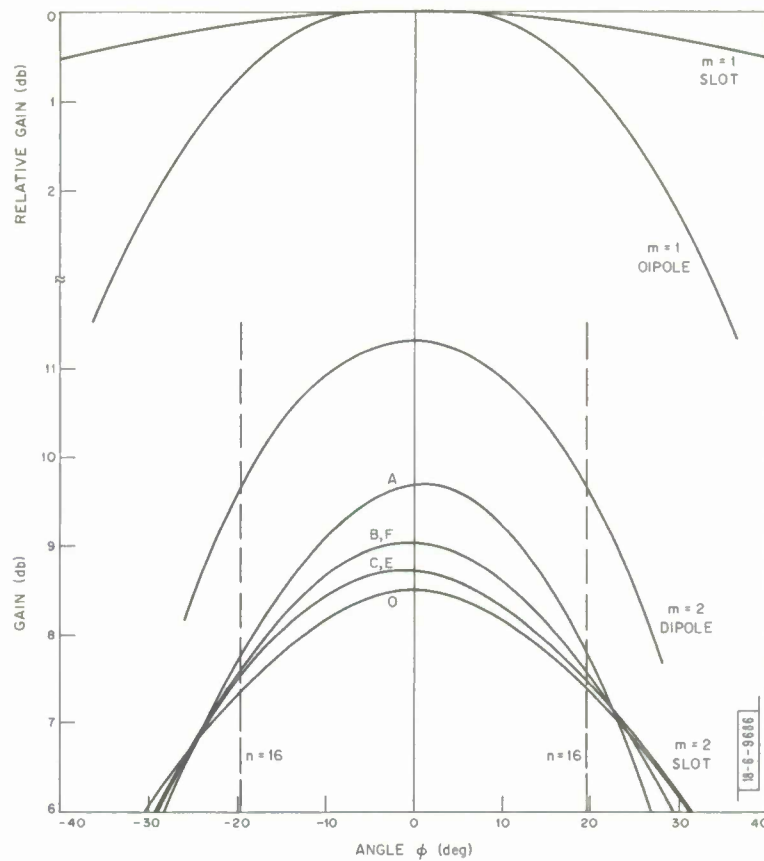
Fig. 9. Measured equatorial-plane patterns.
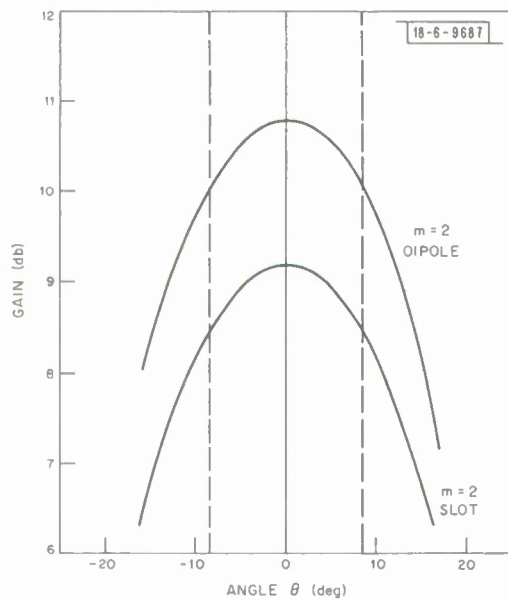


Fig. 10. Measured polar-plane patterns.
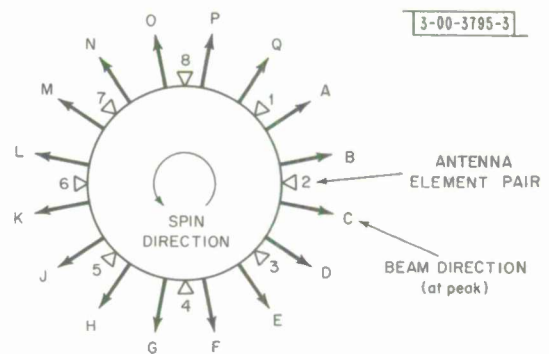


Fig. 11. Relation of beam directions to antenna positions.

37
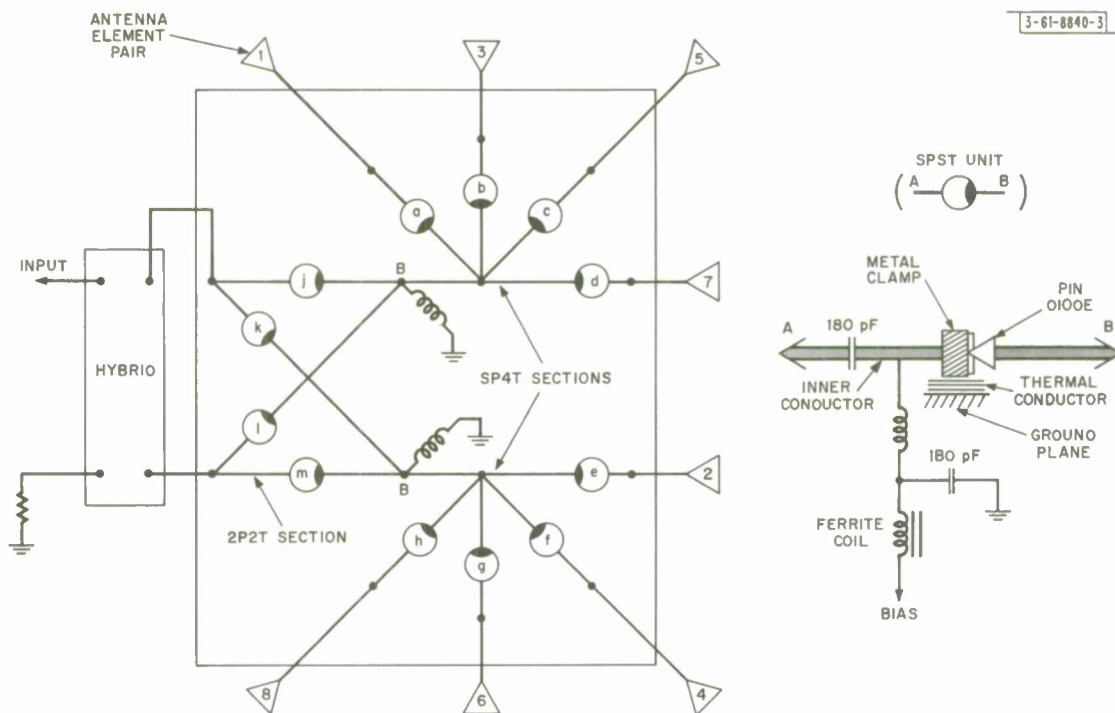
Fig. 12. Switch matrix and details as given in a SPST unit.
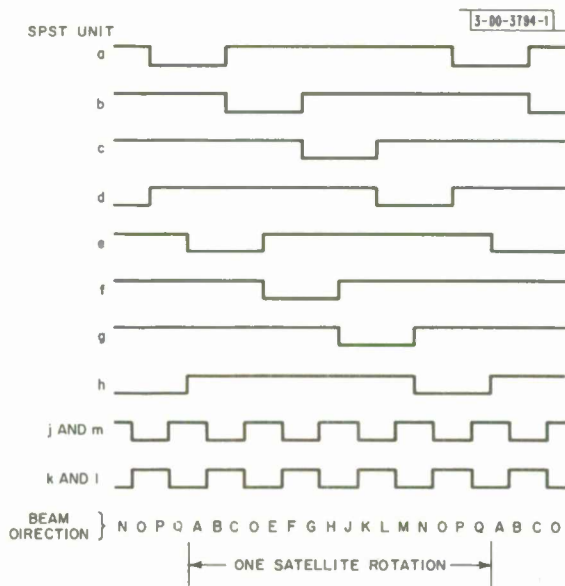


Fig. 13. Signal representations of states of SPST units.
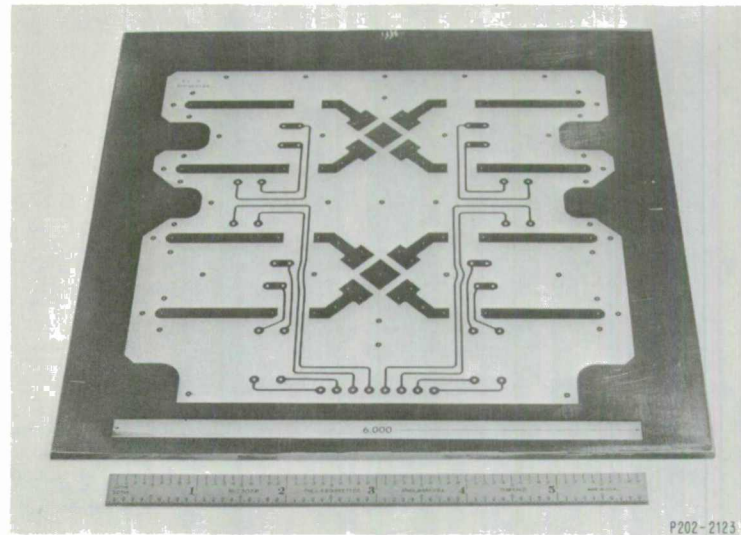
Fig. 14. Photo-etched circuit board.



Fig. 15. Alignment of 2P2T and SP4T sections.
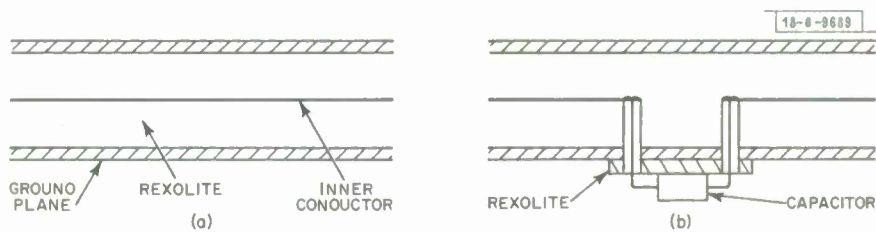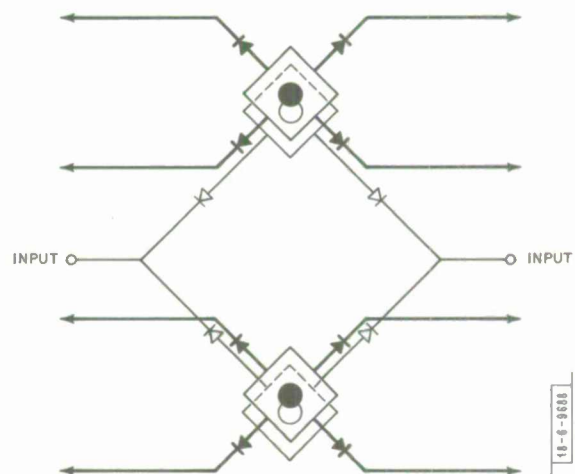


Fig. 16(a-b). Configuration for measuring effect of locating components outside stripline sandwich.

18-6-9690

METAL BLOCK

1/2 INCH

DIODE

BORON
NITRIDE

1 INCH

REXOLITE

6 INCHES

GROUND PLANES

* THERMOCOUPLES

SUPPORT
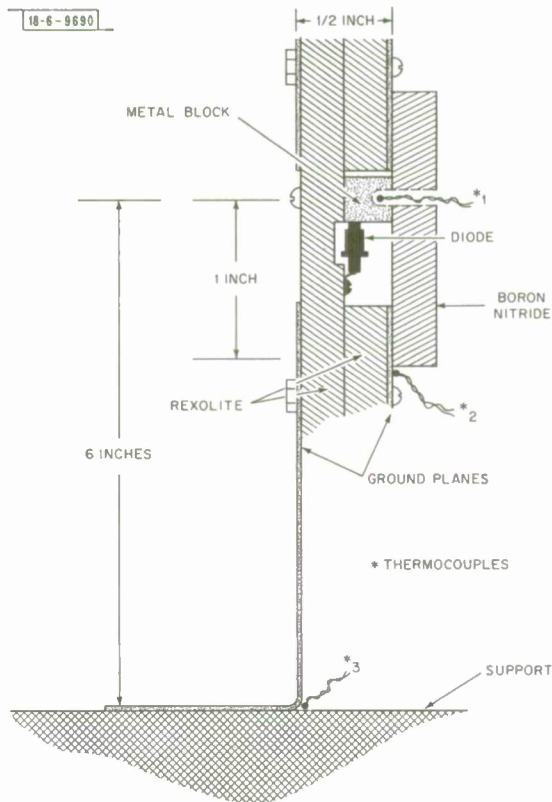
Fig. 17.   Sketch of diode placement and boron
nitride for heat dissipation.



P202-1800
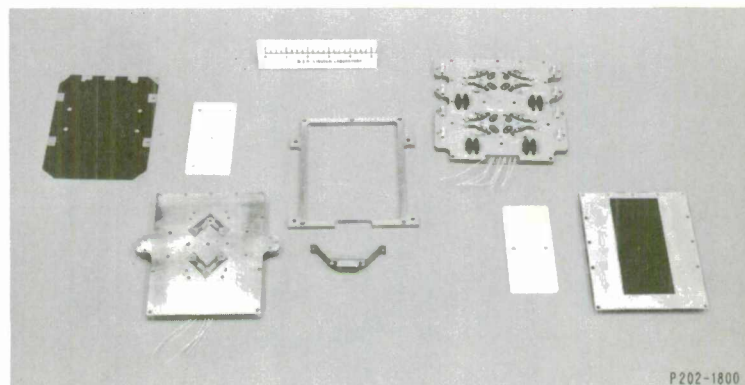
Fig. 18.   Switch sections.
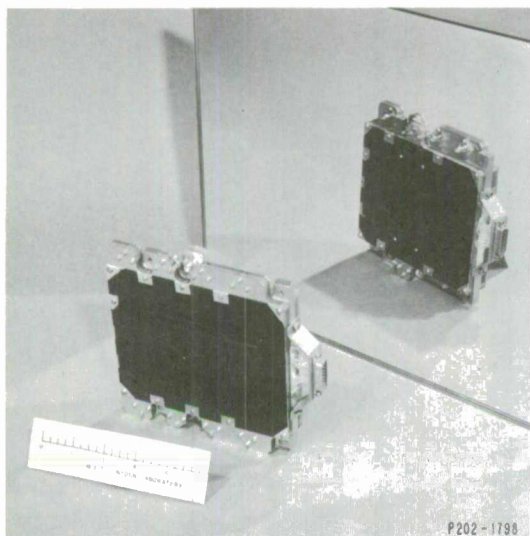
Fig. 19. Switch assembled.
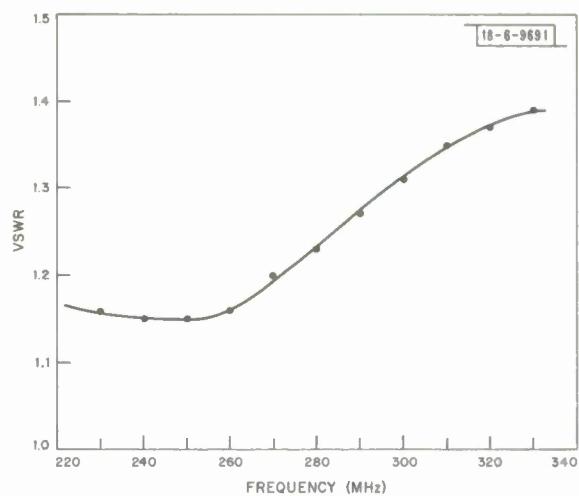


Fig. 20. Switch VSWR vs frequency.
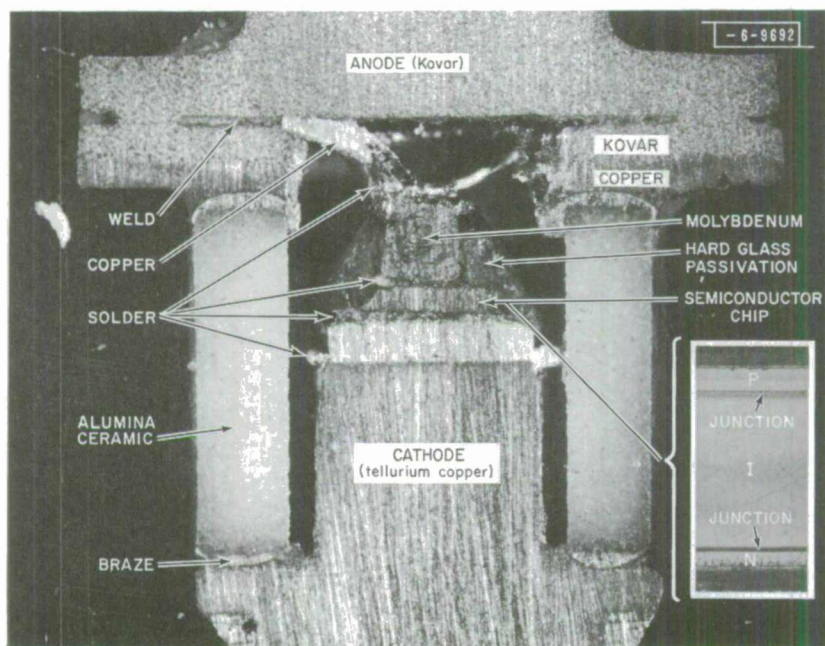


Fig. 21. Details of PIN diade. Anode, cathode, capper, and malybdenum parts are gald plated.

41
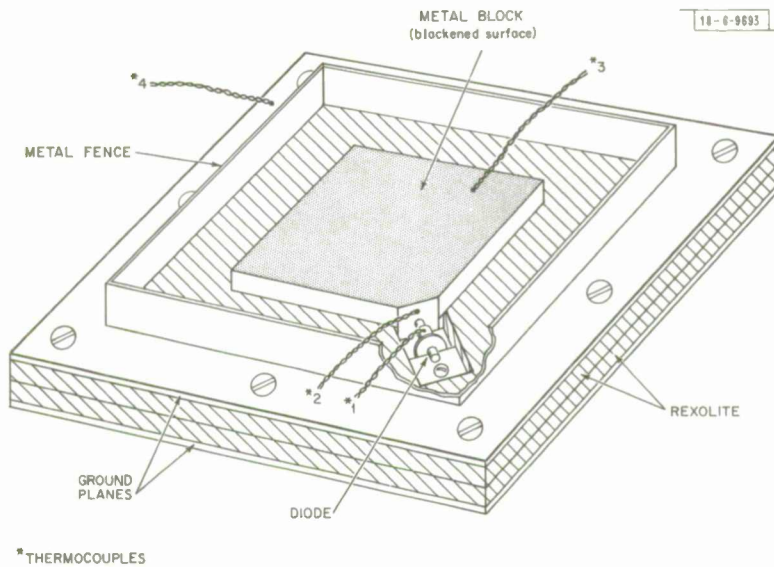
Fig. 22. Diode with heat radiator.
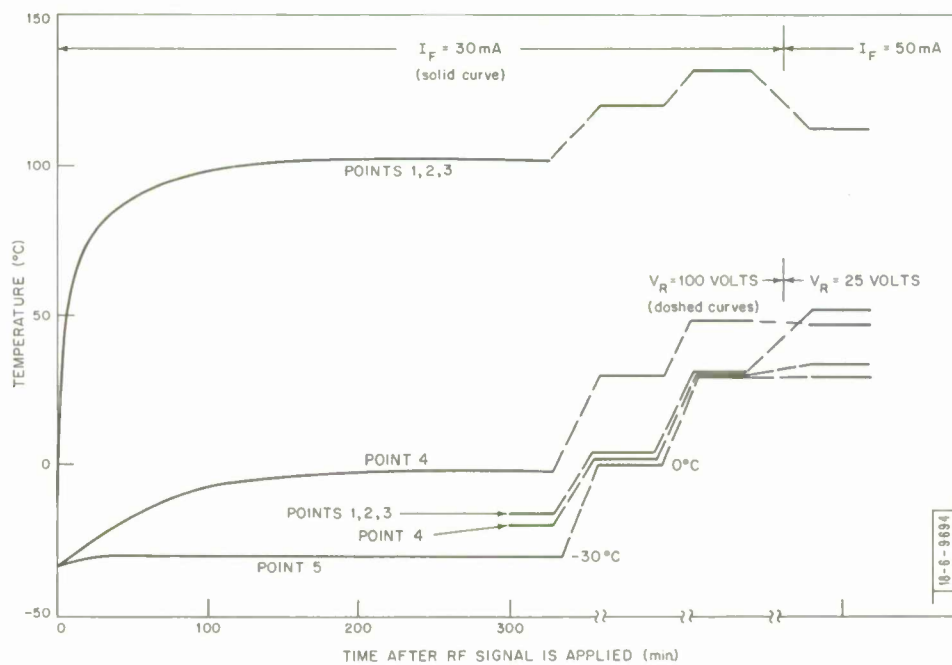


Fig. 23. Measured temperatures in vacuum of SPST unit of configuration shown in Fig. 22 ($P_T = 30$ watts; $P_d = 1.0$ watt; pressure $< 10^{-5}$ torr; diode: 1 ohm; 18°C/watt).

Fig. 24. Vacuum measurements af SPST unit af configuratian shown in Fig. 17 ($P_T = 30$ watts; $P_d = 1.0$ watt; $I_F = 50$ mA; pressure $< 10^{-5}$ tarr; diade: 1 ohm; 18°C/watt).
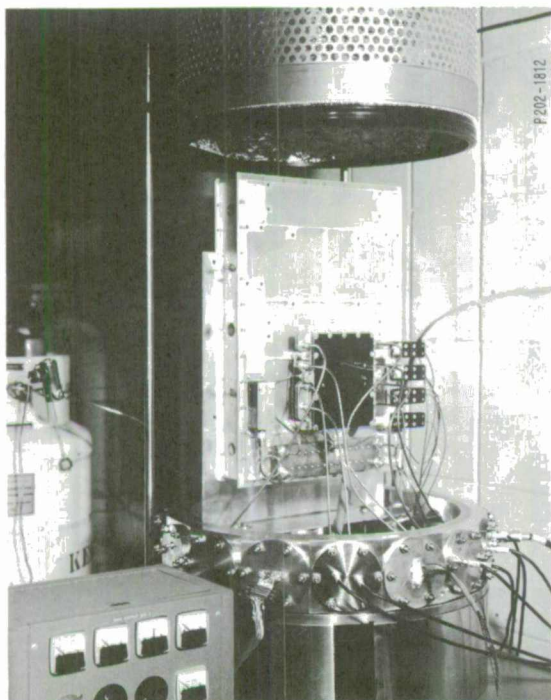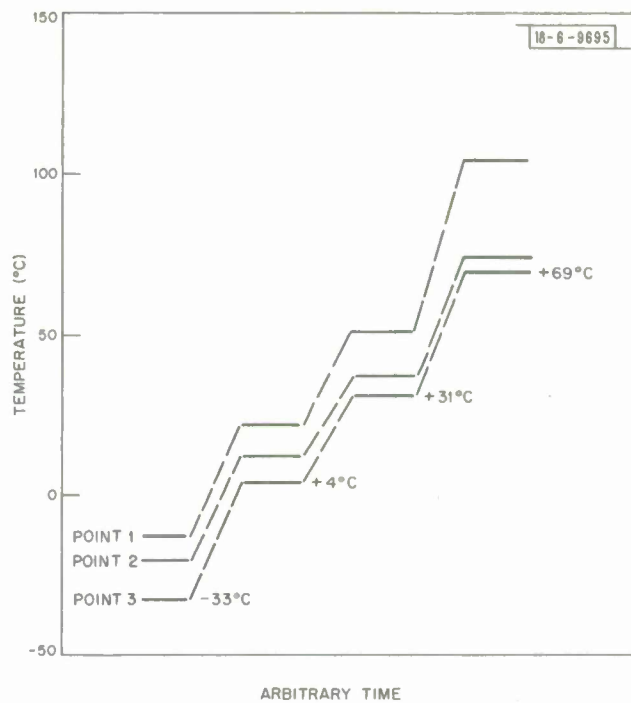


Fig. 25. Switch matrix maunted for temperature vacuum measurements.

43
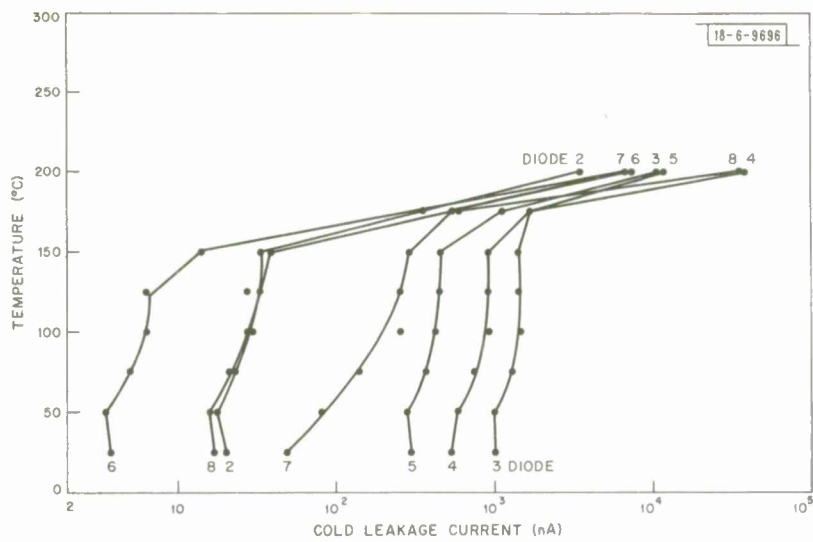
Fig. 26. Cold leokoge current of 7 diodes in stress test ot 100-volt bios with temperotures stepped 25°C in 24-hour intervols.
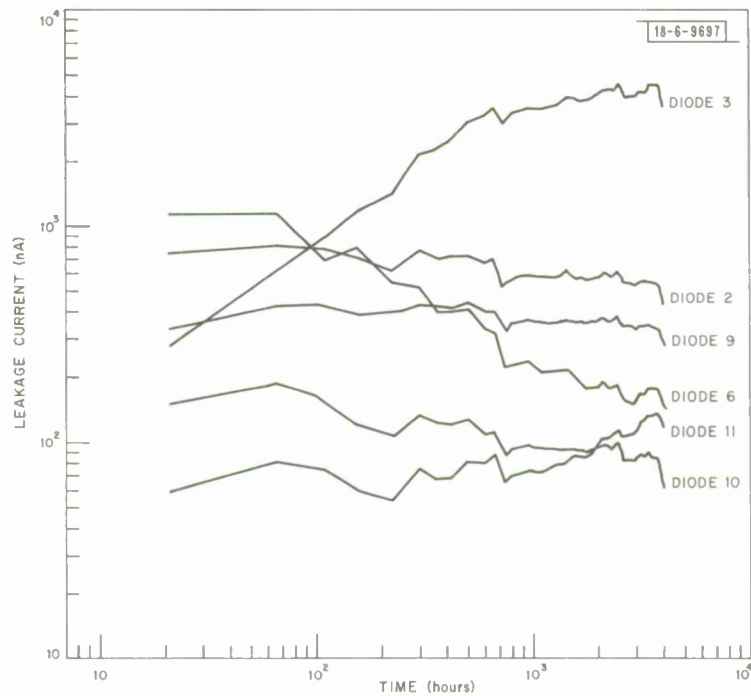


Fig. 27. Cold leokoge current of 6 diodes in life test ot 100-volt reverse bios ond 125°C.
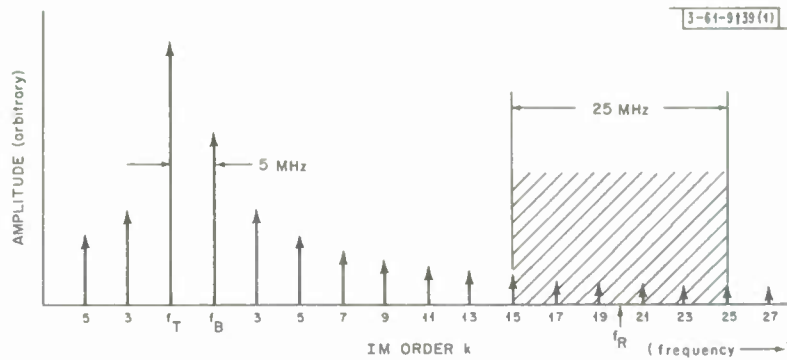
Fig. 28. IM terms affecting the communications system.
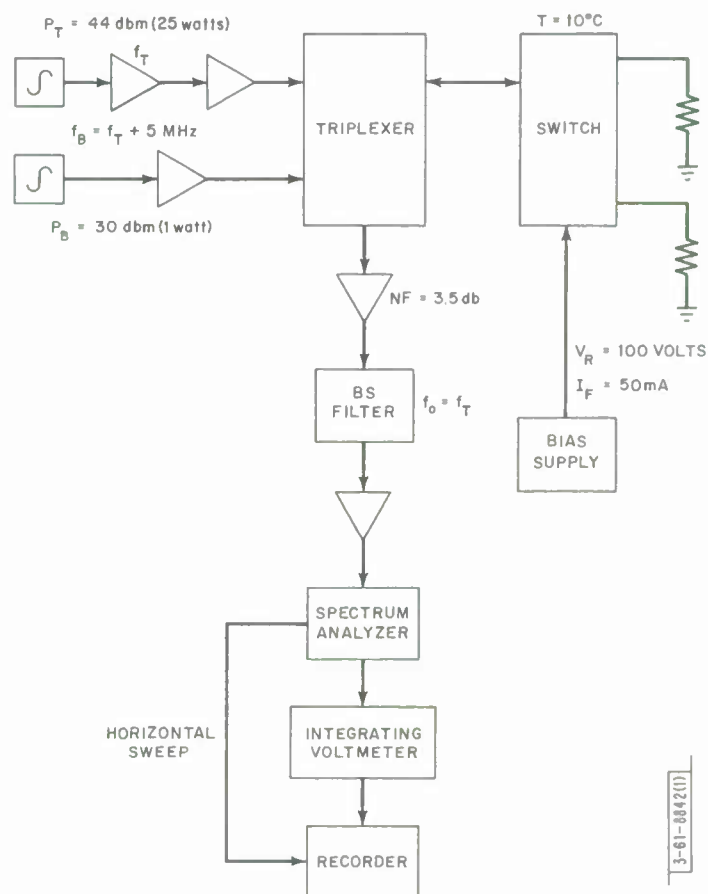


Fig. 29. Setup for IM measurement.
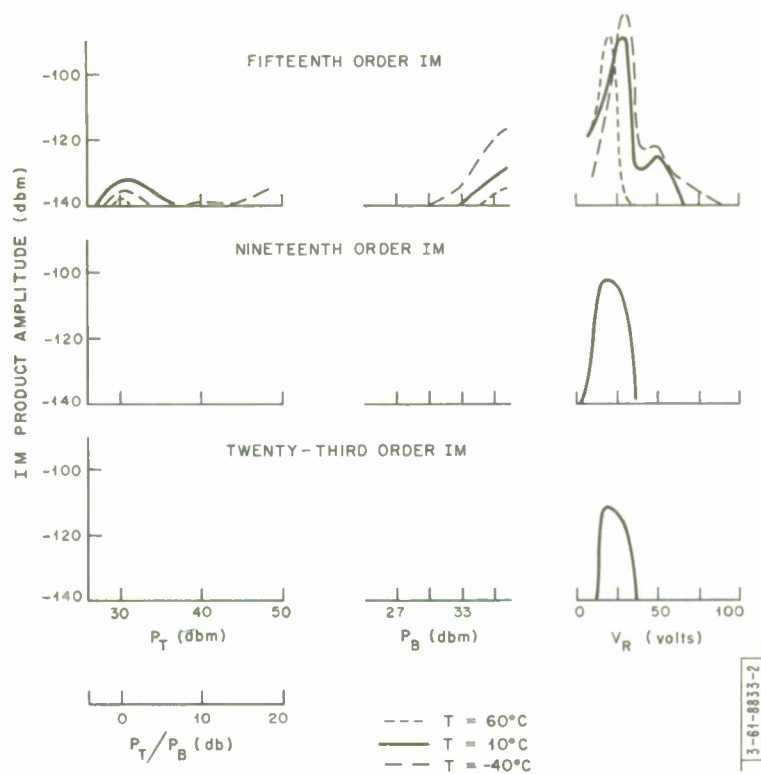
Fig. 30. IM dependence on $P_T$, $P_B$, $V_R$, and T for 3-mil diode.
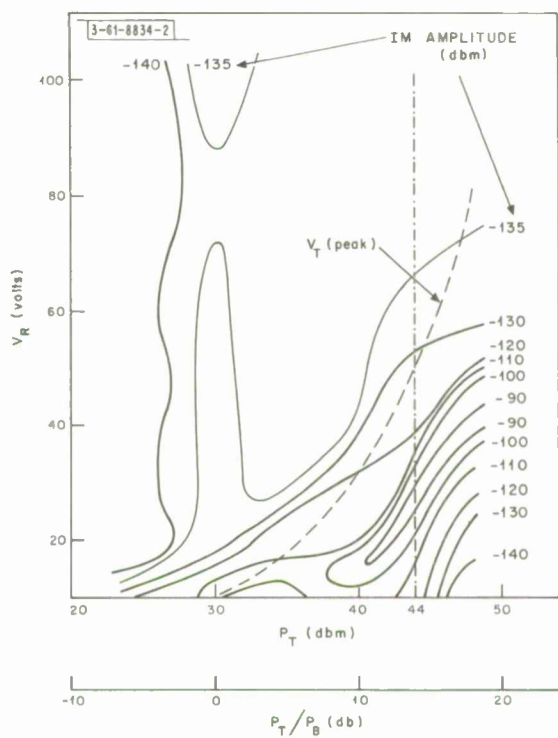


Fig. 31. Contours of constant IM (fifteenth order) for 3-mil diode (T = 10°C).
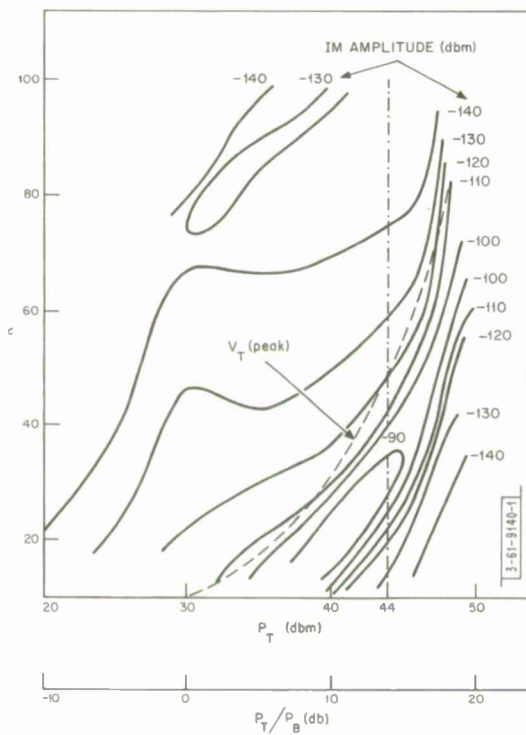


Fig. 32. Contours of constant IM (fifteenth order) for 2-mil diode (T = 10°C).
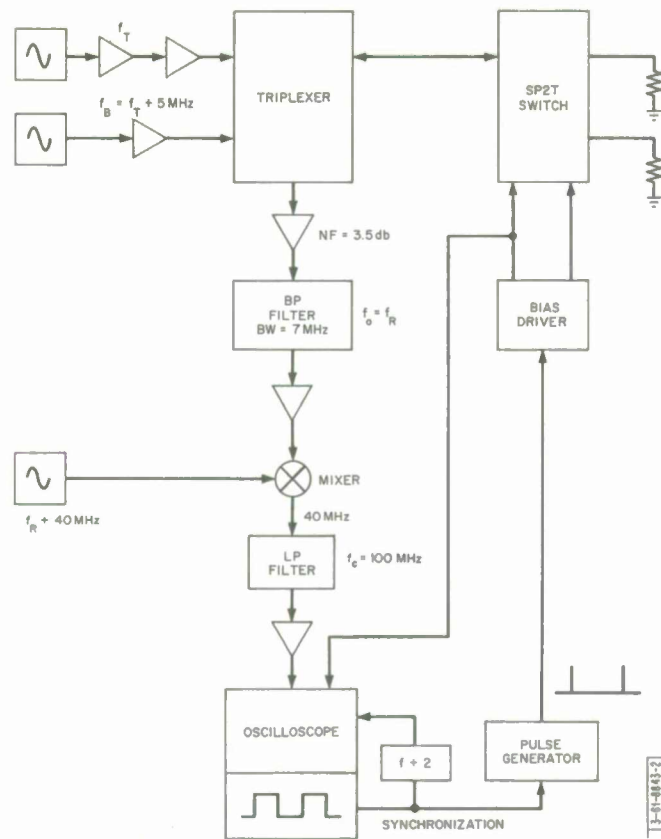
Fig. 33.  Setup for switching-noise measurement.
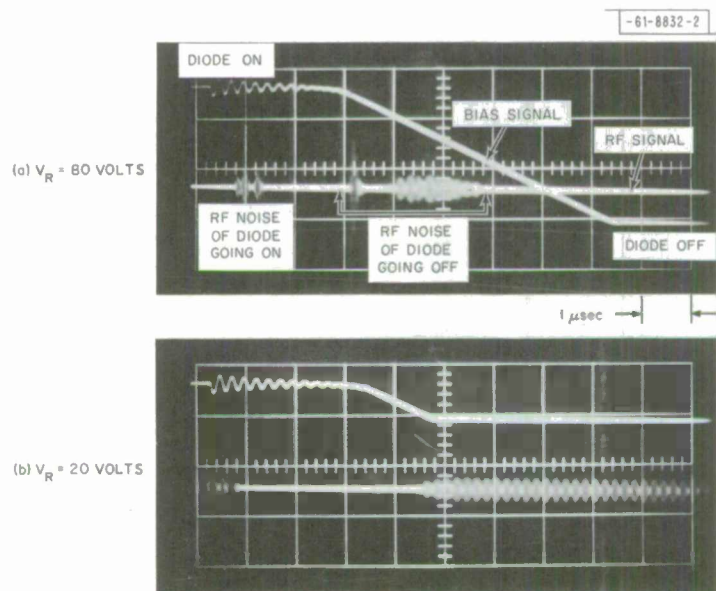


Fig. 34(a–b).  Bias and RF signals during switching transient
$(P_T = 44$ dbm,  $P_B = 36$ dbm,  $I_F = 50$ mA, $T = -40°C)$.

47

OFF TO ON

ON TO OFF

$-90$

$-\infty$    30    40    50

$P_T$ (dbm)

$-\infty$    27    33

$P_B$ (dbm)

0    25    50

$I_F$ (mA)

0    10    20

$P_T/P_B$ (db)

- - - -  T = 60° C
———  T = 10° C  } (3-mil diode)
— — —  T = -40° C
· · · · ·  T = 10° C (2-mil diode)

3-61-8837-2
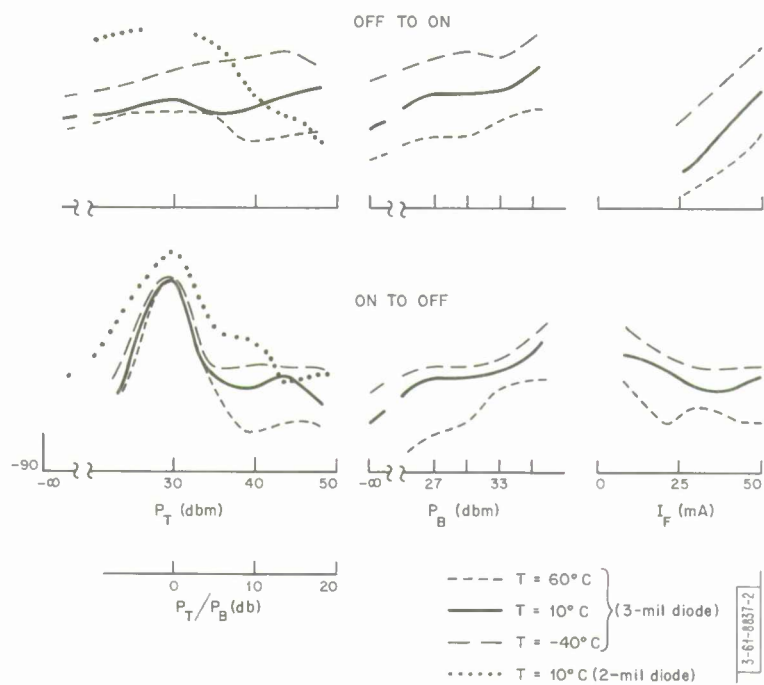
Fig. 35.  Switching-noise dependence.



Fig. 36.  Dipole.

48
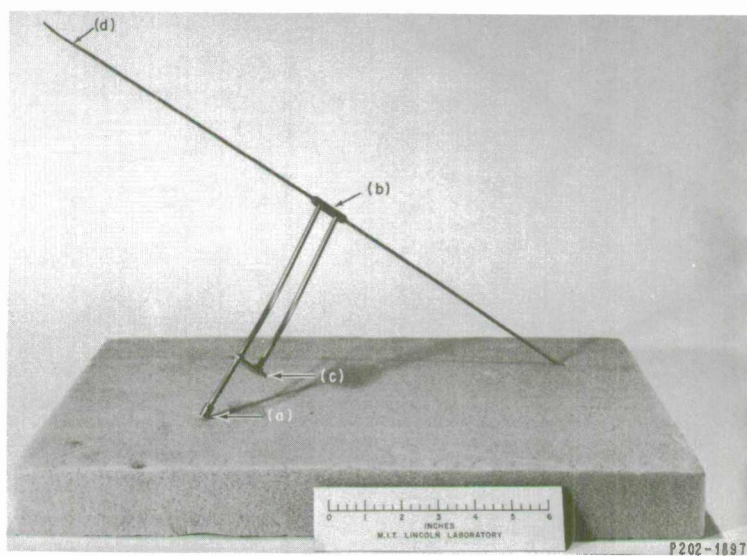
Fig. 37. Sheet-metal model with dipoles.
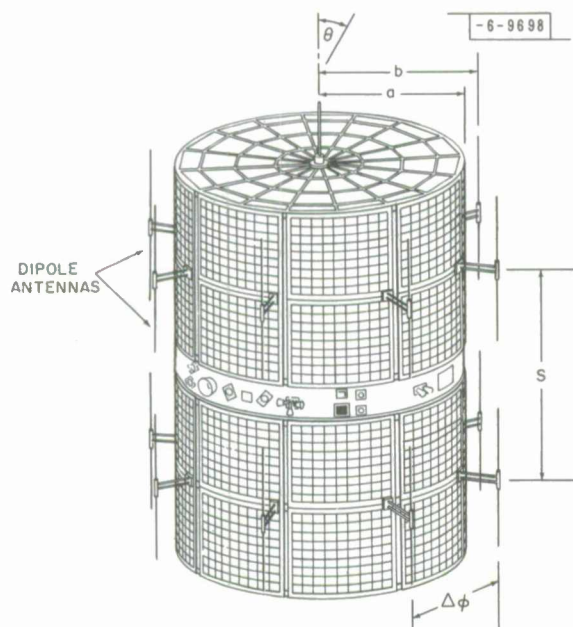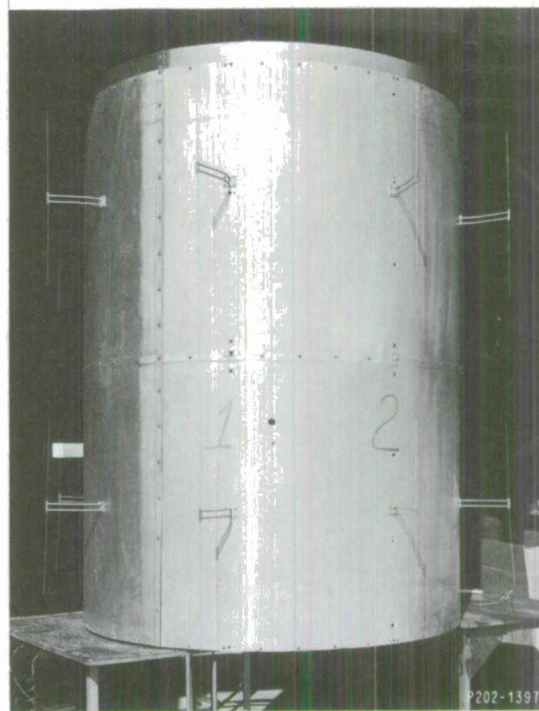


Fig. 38. Dipole geometry.

49
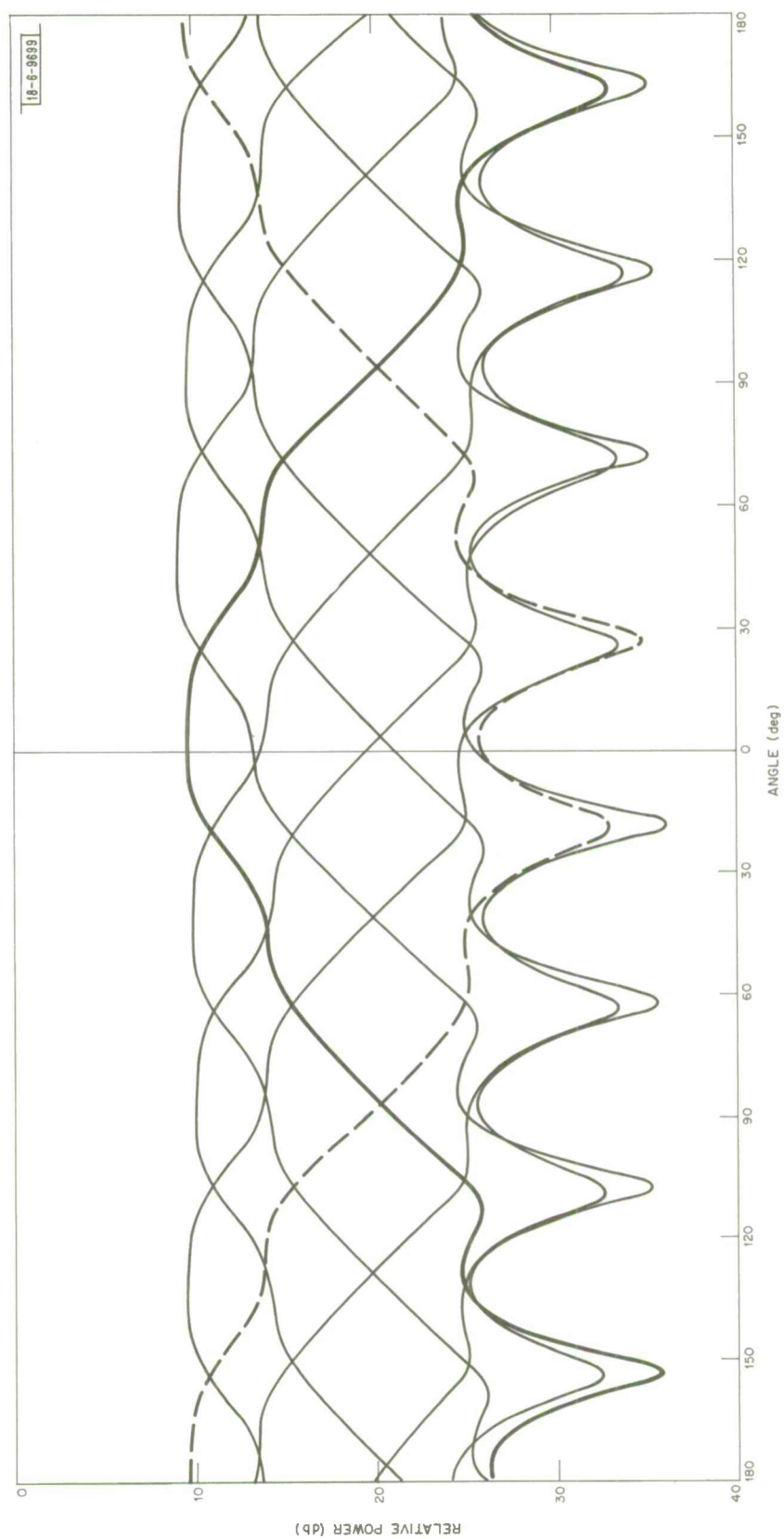
Fig. 39. Measured dipole patterns, equatorial plane.

18-6-9699

ANGLE (deg)

RELATIVE POWER (db)

50

Fig. 40.  Measured admittance of dipole.



Fig. 41.  Admittance of dipole and matching stubs.
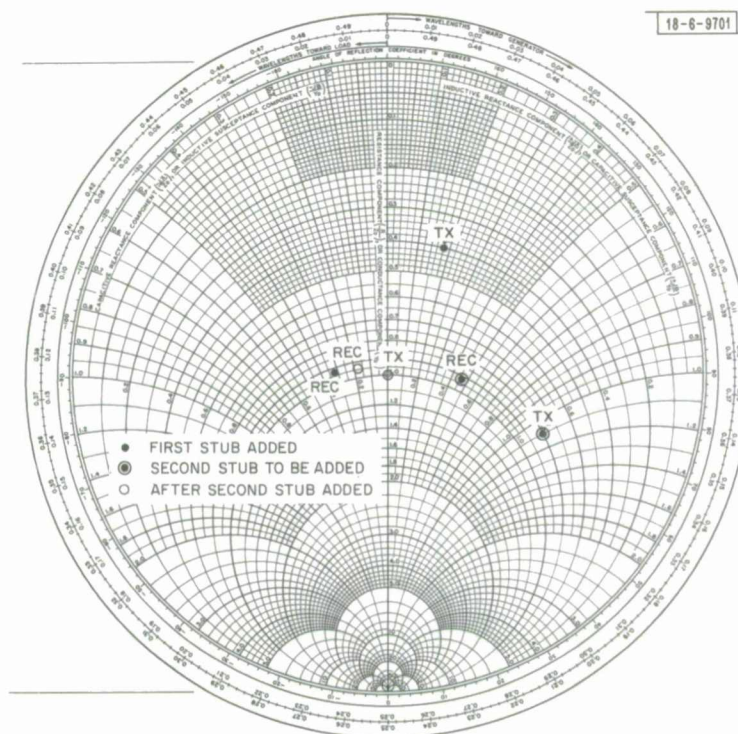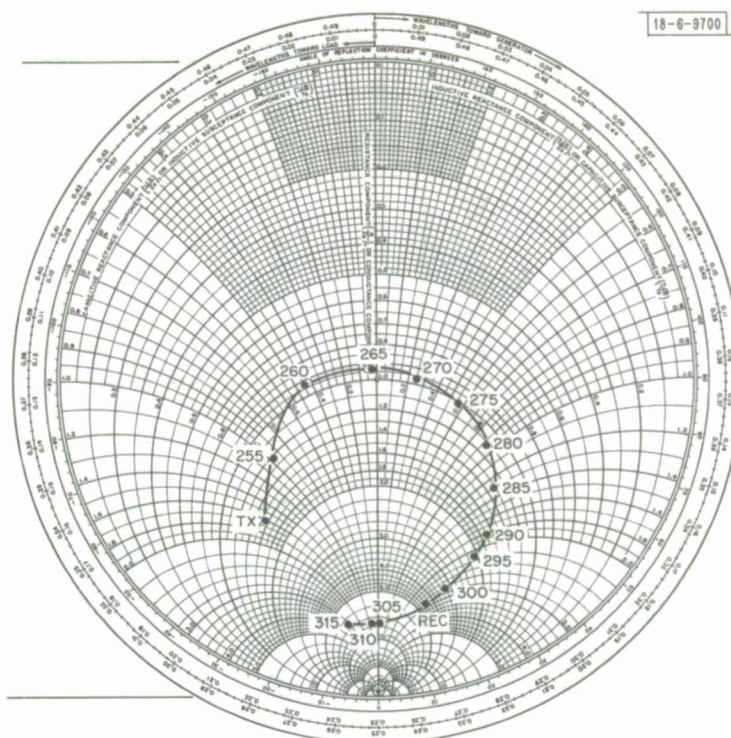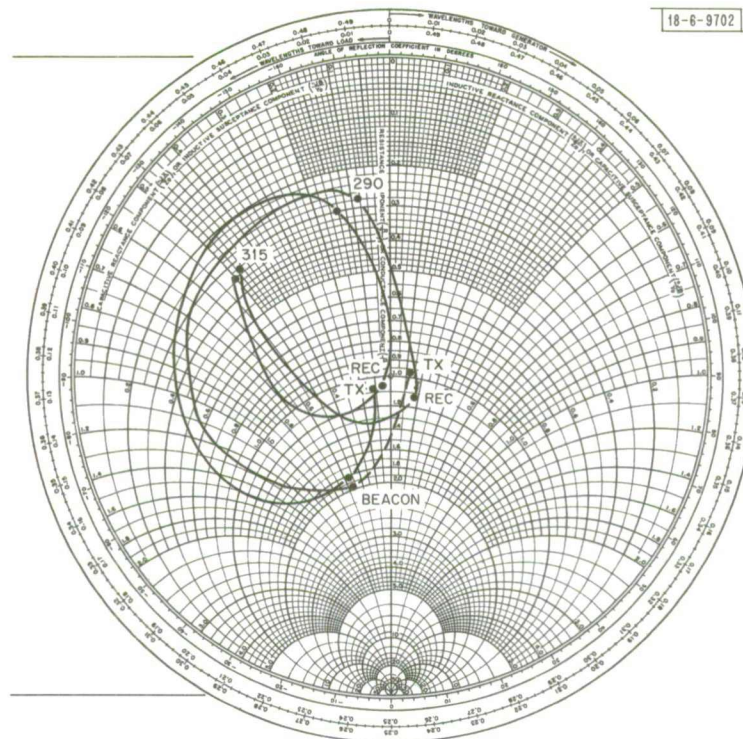
Fig. 42. Effect of scanning on dipole impedance.
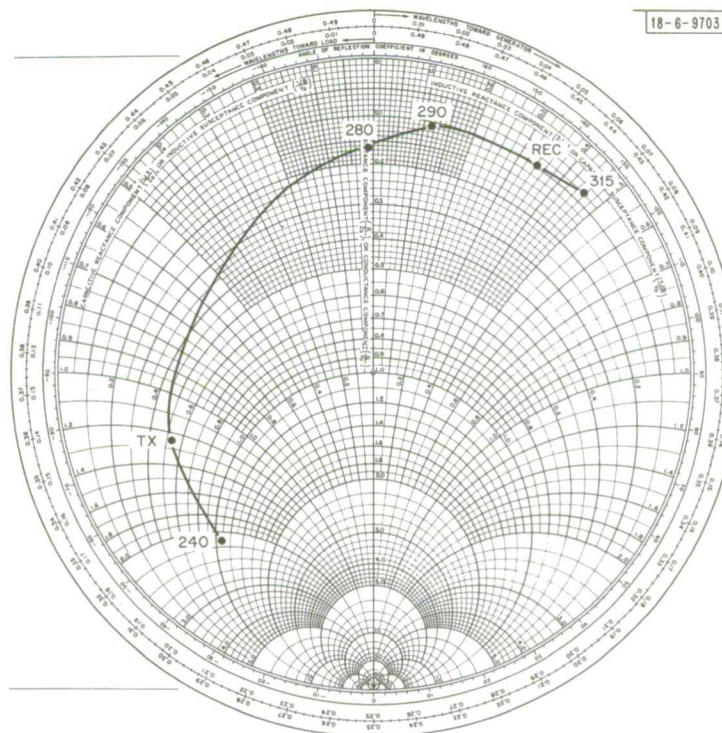


Fig. 43. Measured impedance of single slot.
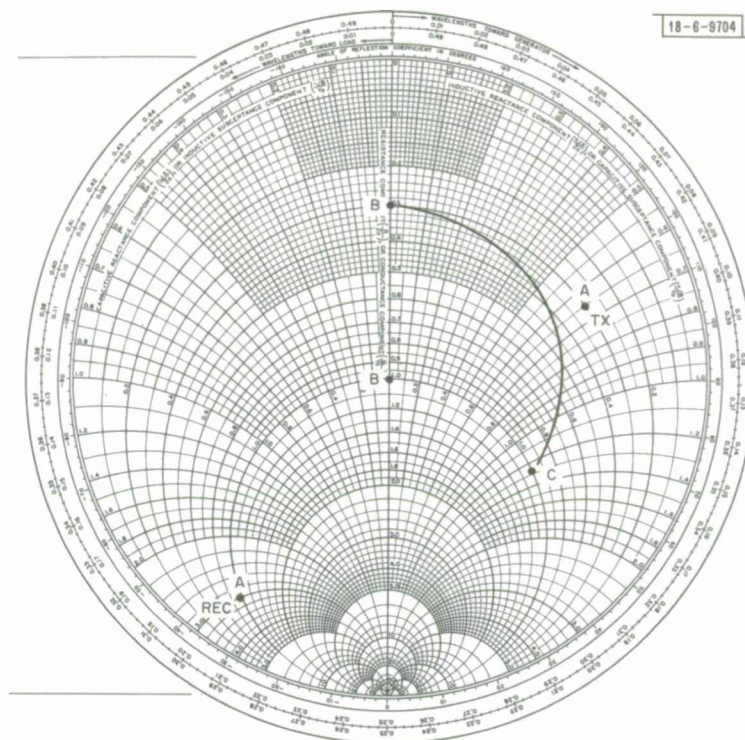
Fig. 44. Slat and matching network admittance.
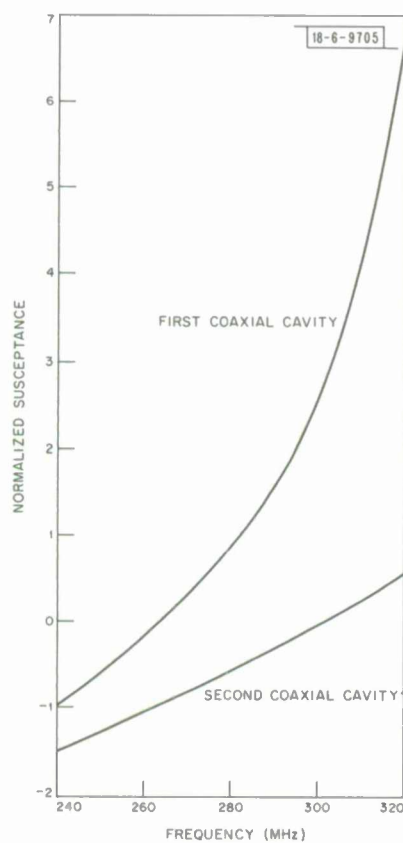


Fig. 45. Coaxial-cavity susceptance.
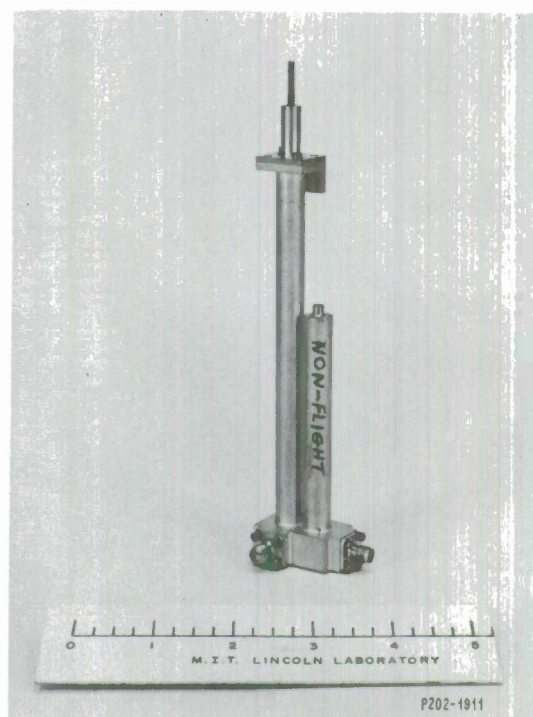


Fig. 46. Folded coaxial cavity.

53
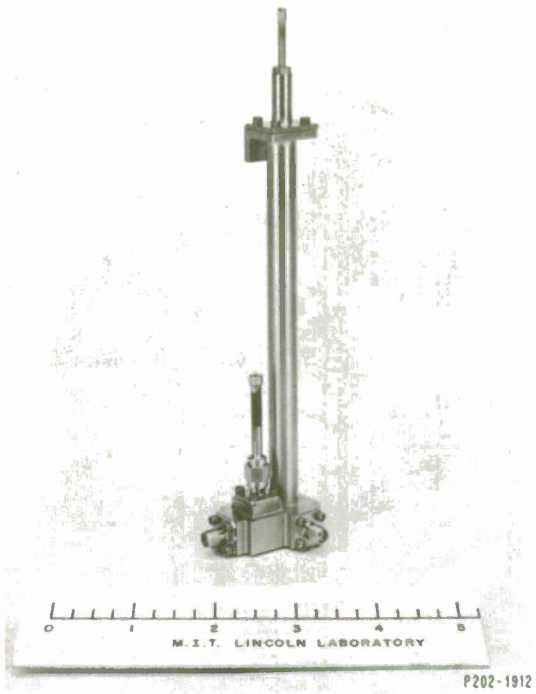
Fig. 47.  Flight coaxial cavity.

P202-1912
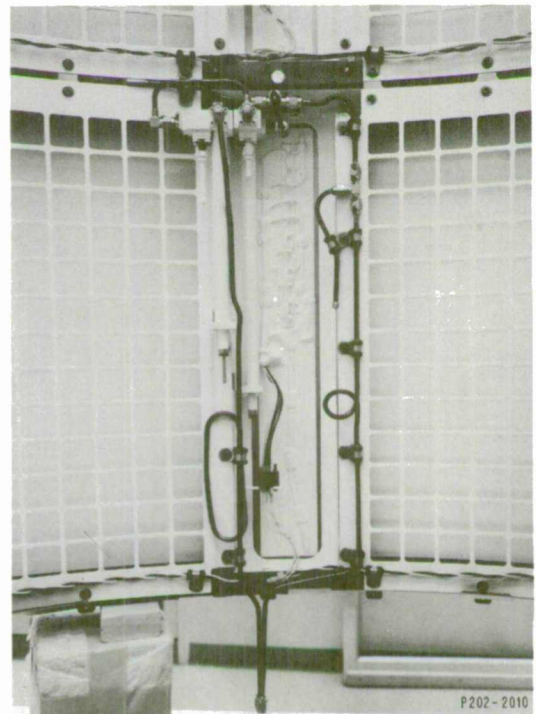


Fig. 48.  Inside view of upper array.

P202-2010

Fig. 49. Inside view of viewband.

P202-1568



18-6-9706
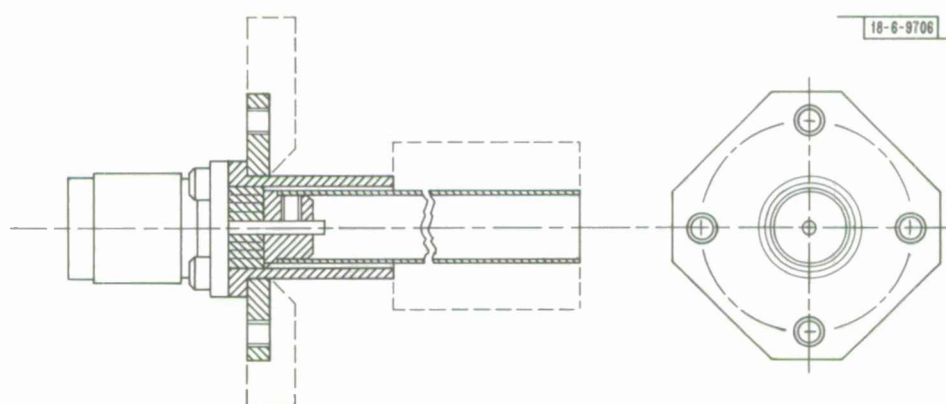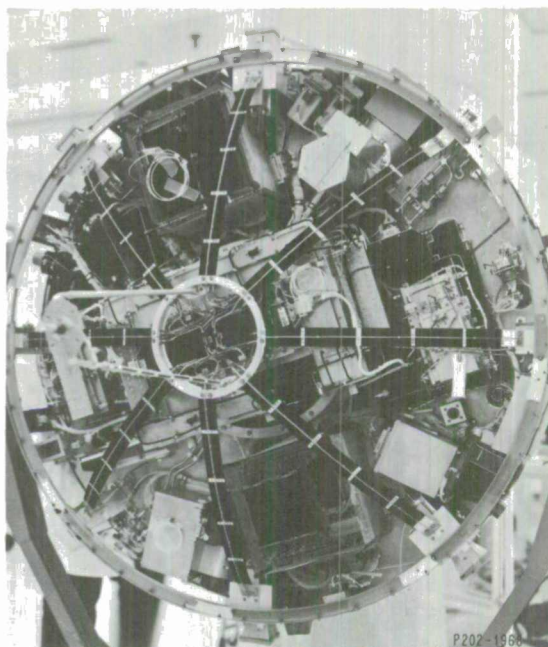
Fig. 50. Monopole details.
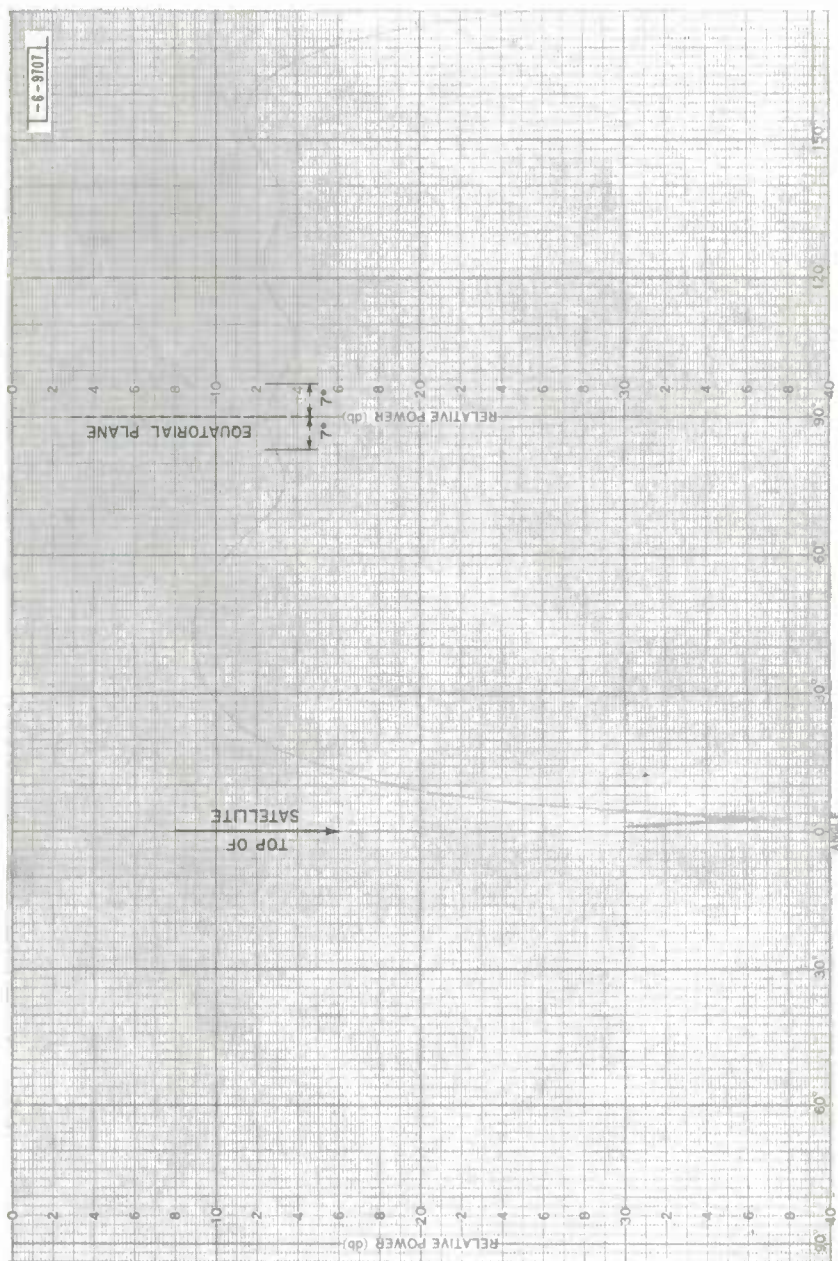
(a) Polar pattern.

Fig. 51. Flight-model TLM antenna patterns.
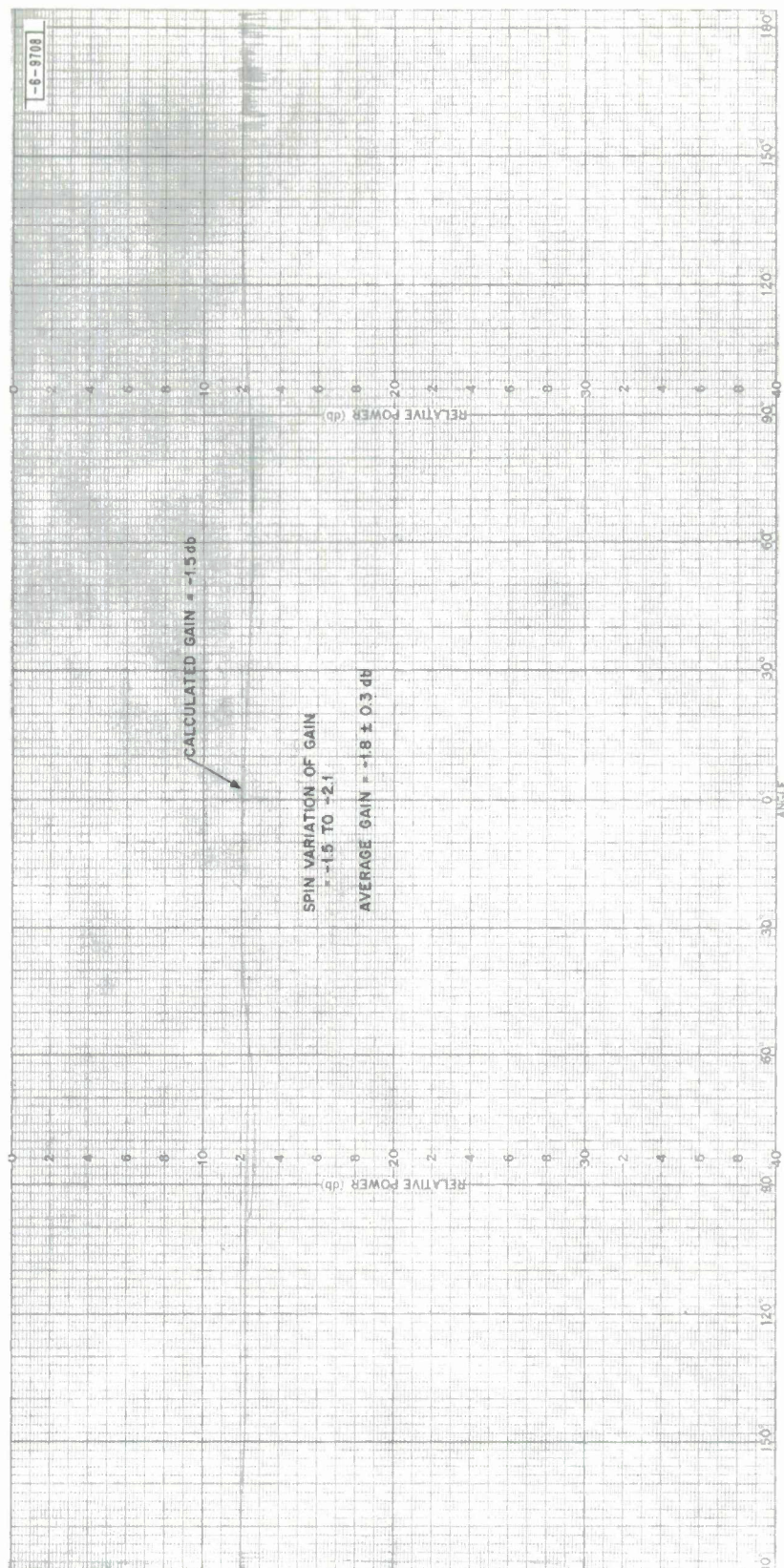
(b) Equatorial pattern.

Fig. 51. Continued.
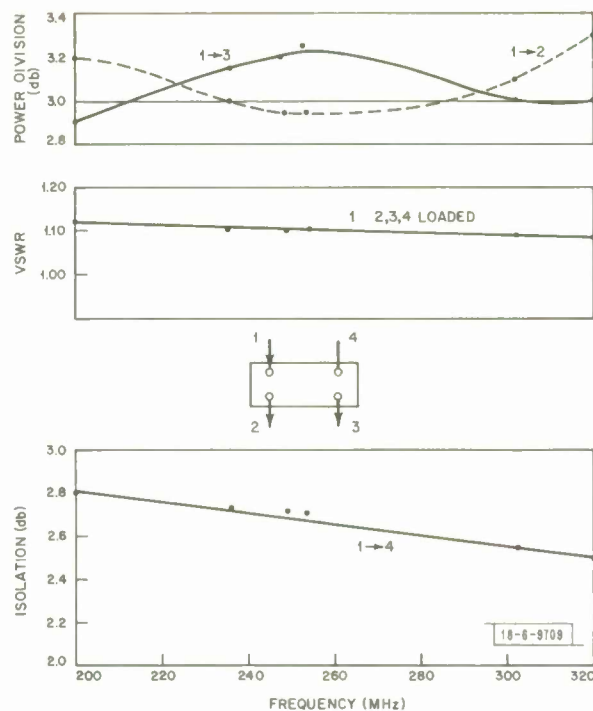
Fig. 52. LES-6 hybrid typical data.
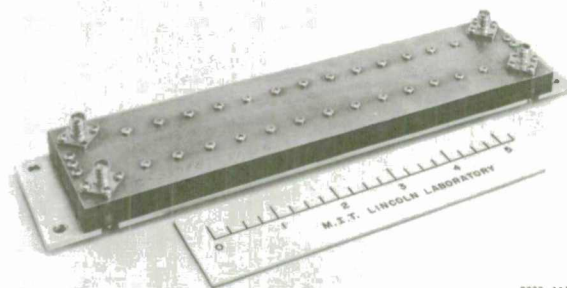


Fig. 53. Hybrid.
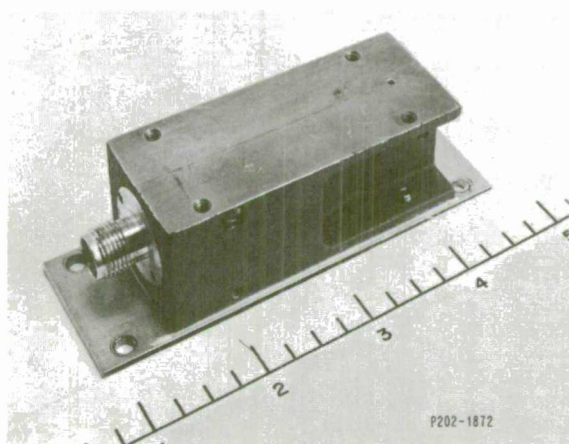


Fig. 54. Hybrid load.
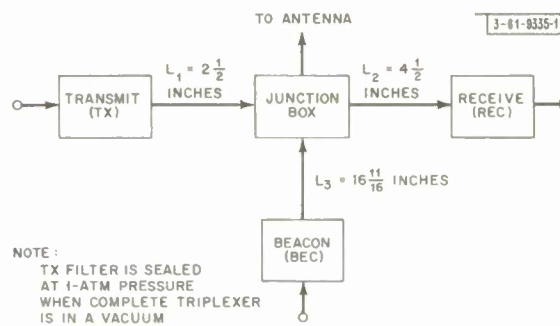


Fig. 55. LES-6 triplexer configuration.
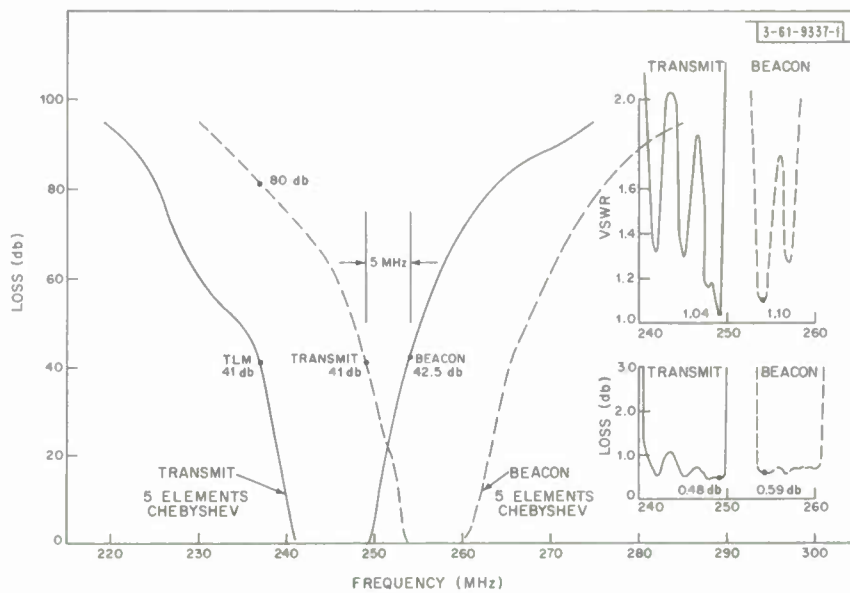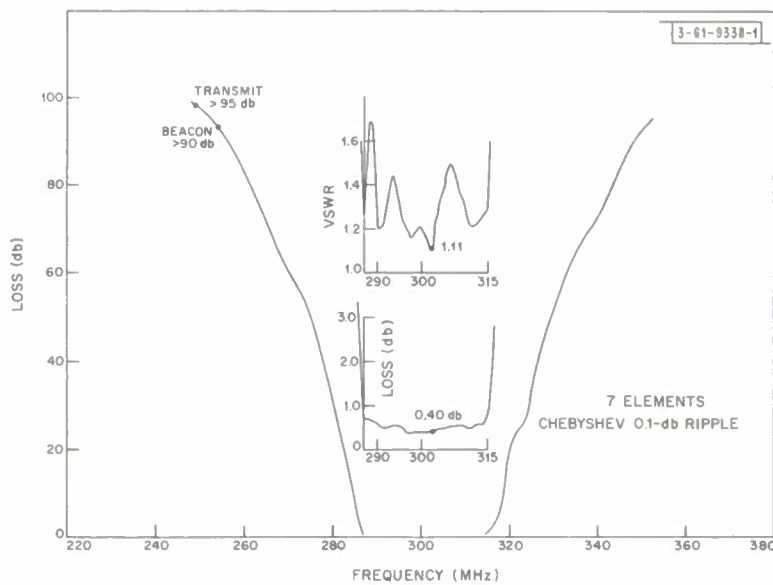
Fig.56. Measured response of (a) transmit and beacon interdigital filters; (b) receive interdigital filter.

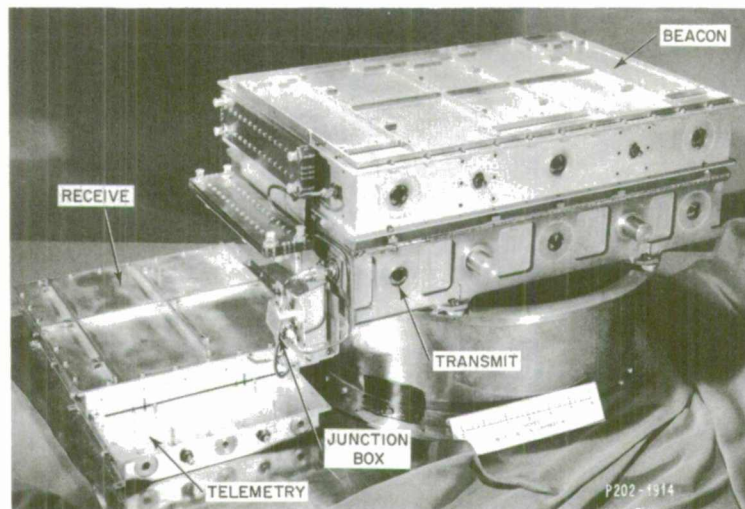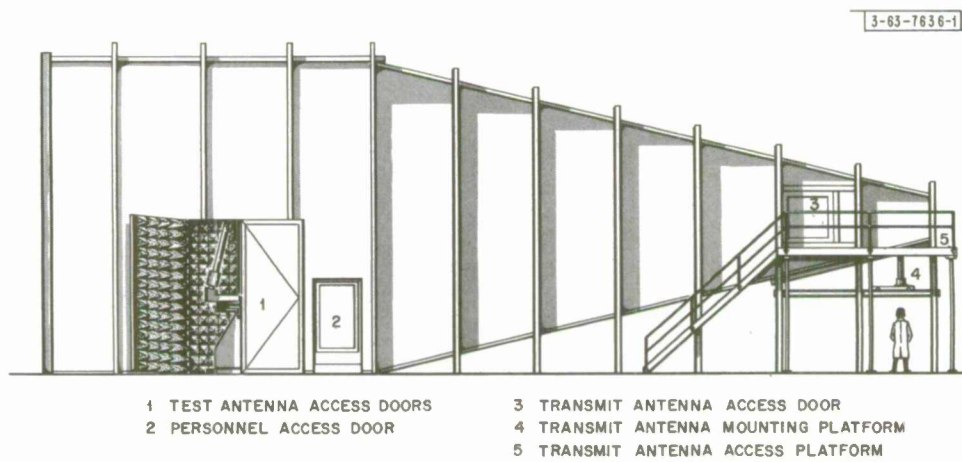Fig. 57. LES-6 triplexer.



1  TEST ANTENNA ACCESS DOORS       3  TRANSMIT ANTENNA ACCESS DOOR
2  PERSONNEL ACCESS DOOR           4  TRANSMIT ANTENNA MOUNTING PLATFORM
                                   5  TRANSMIT ANTENNA ACCESS PLATFORM

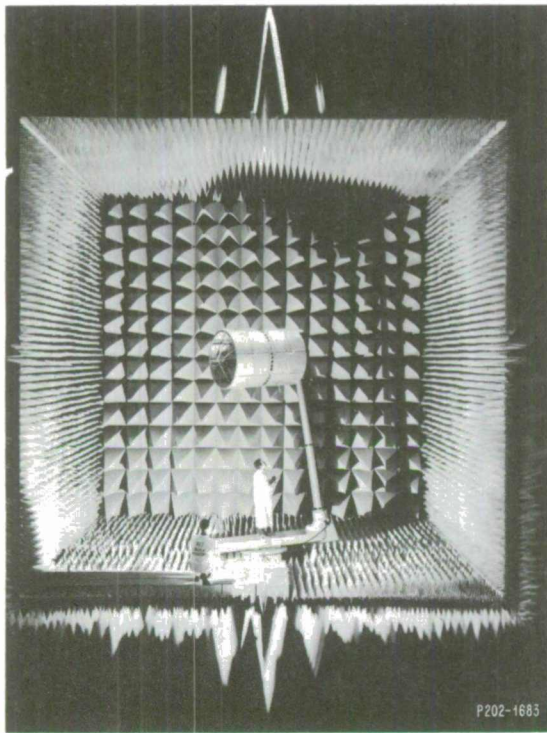Fig. 58. SEL anechoic chamber.

Fig. 59.   LES-6 antenna model in anechoic chamber.
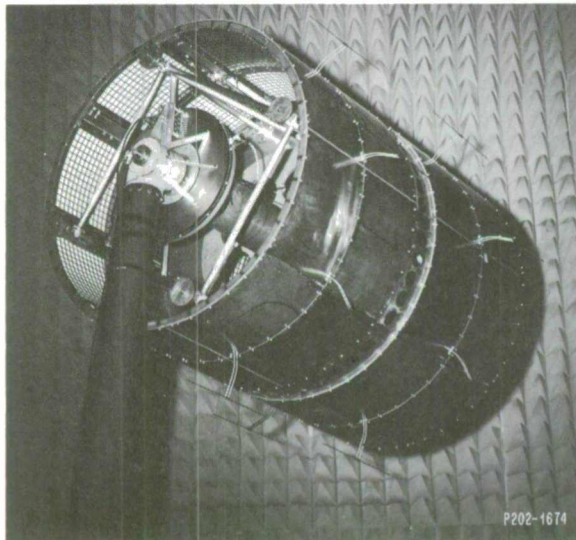


Fig. 60.   Antenna positioner.
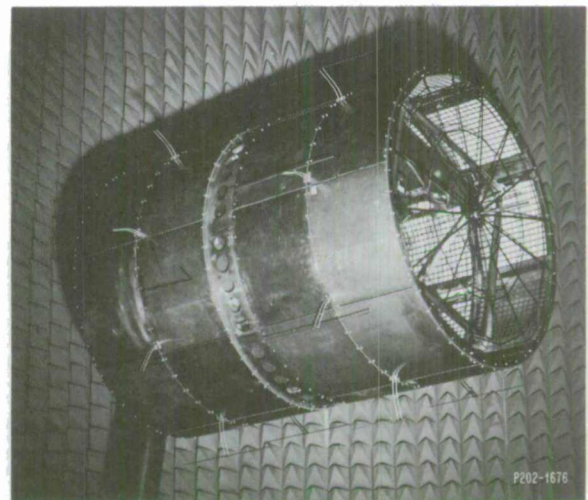


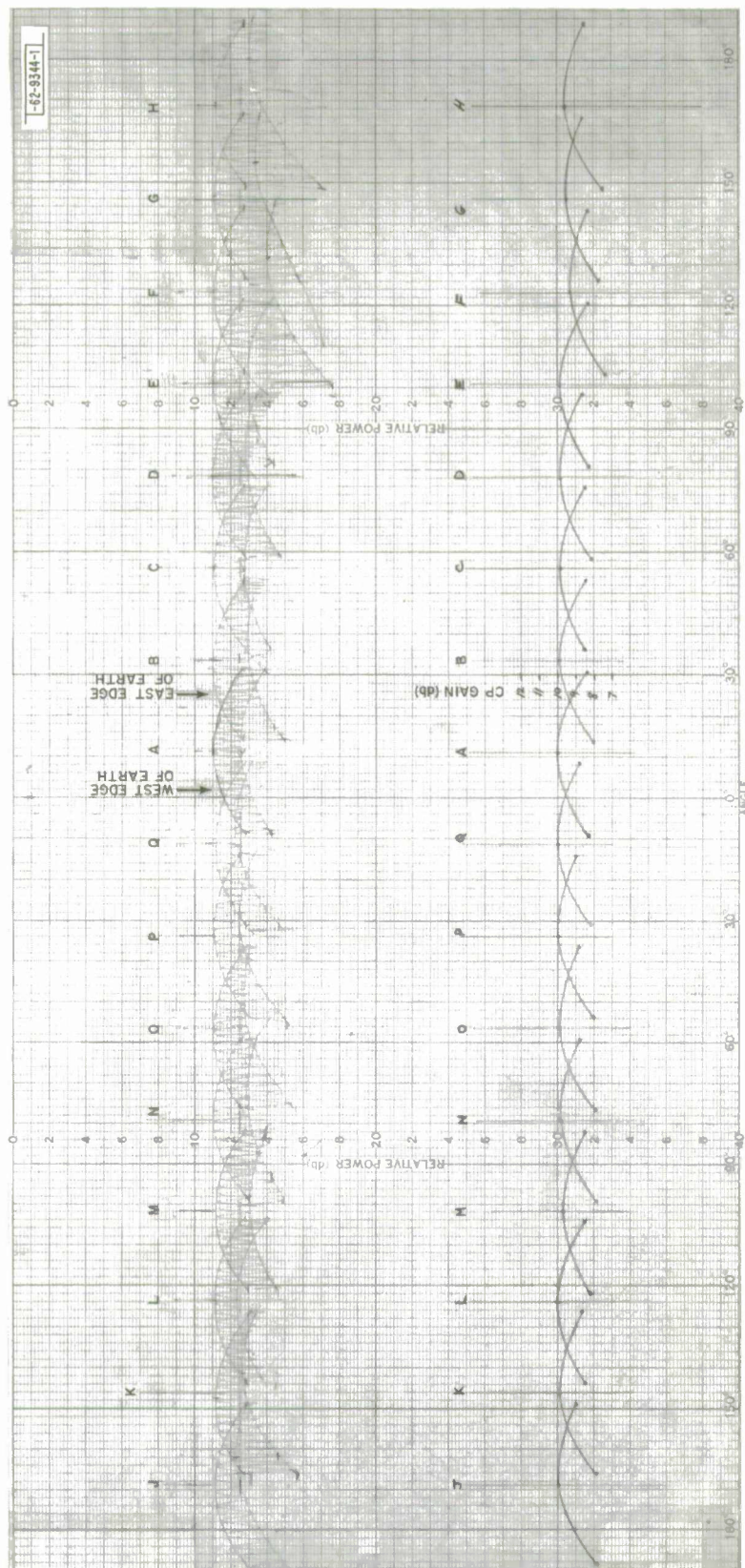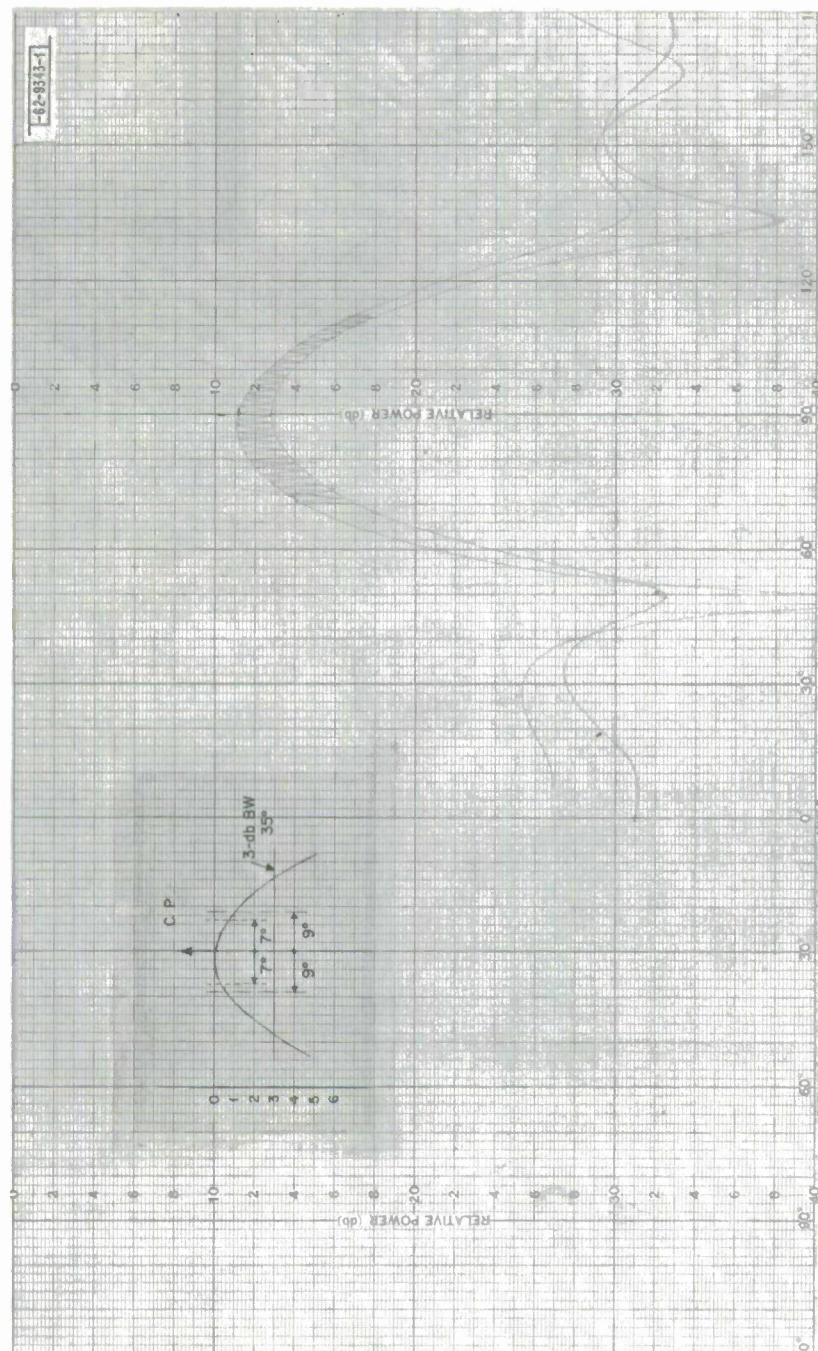Fig. 61.   Head and slip-ring assembly.



Fig. 62.   TLM antenna and ground plane.

(a) Equatorial-plane pattern.

Fig. 63. Radiation patterns for scan mode, transmit frequency.
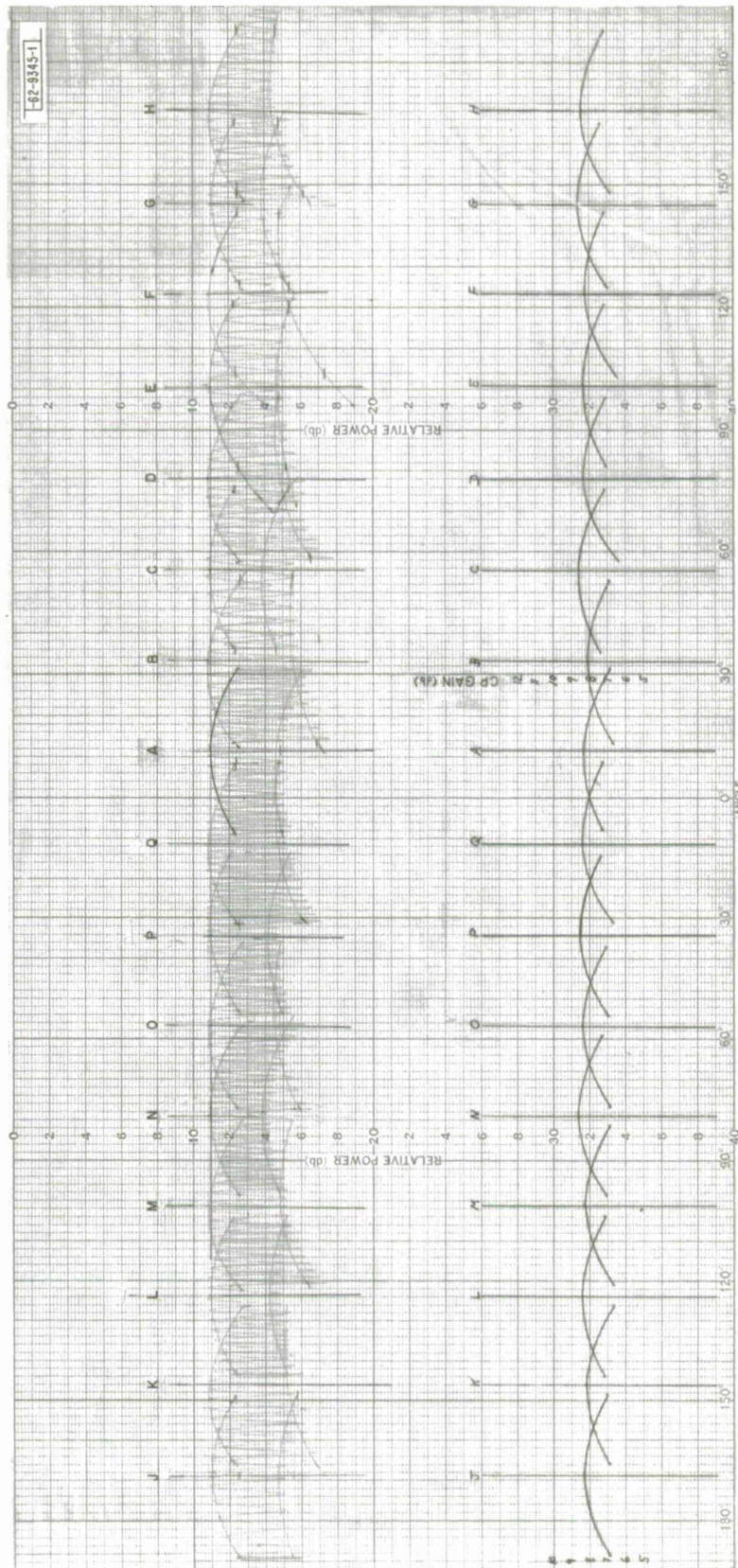
(b) Polar-plane pattern.

Fig. 63.  Continued.

(a) Equatorial-plane pattern.

Fig. 64. Radiation patterns for scan mode, beacon frequency.

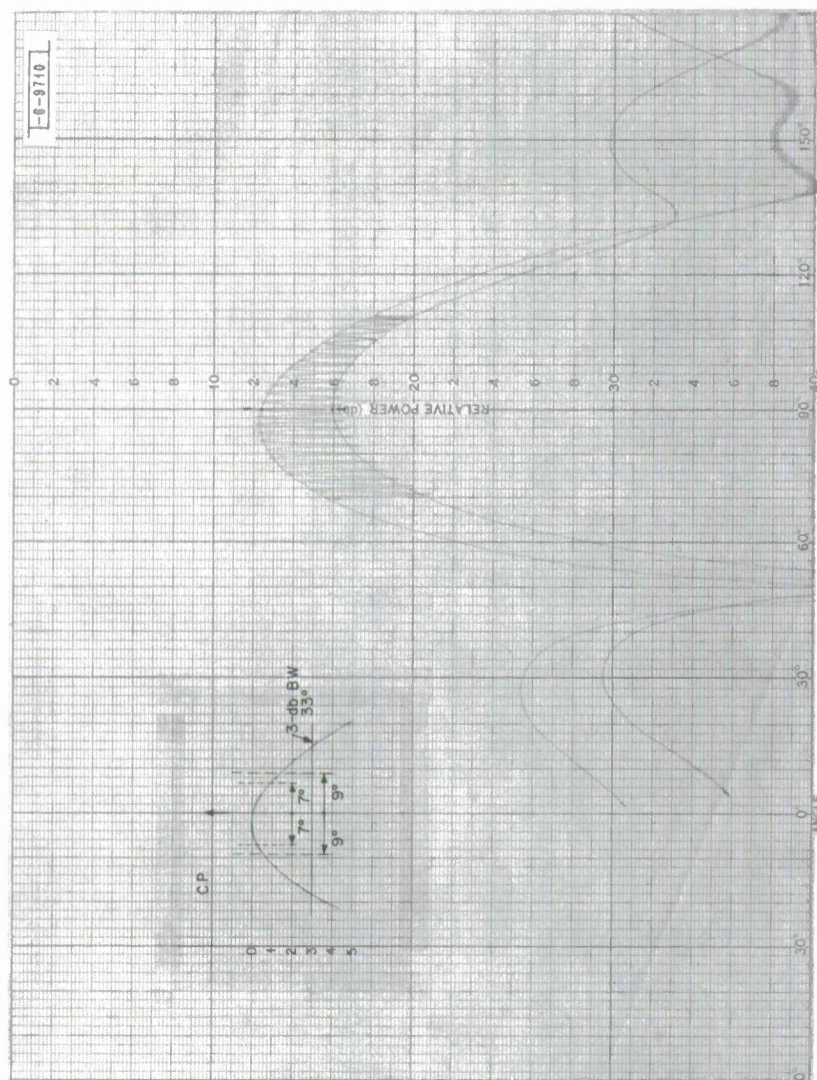(b) Polar-plane pattern.

Fig. 64. Continued.
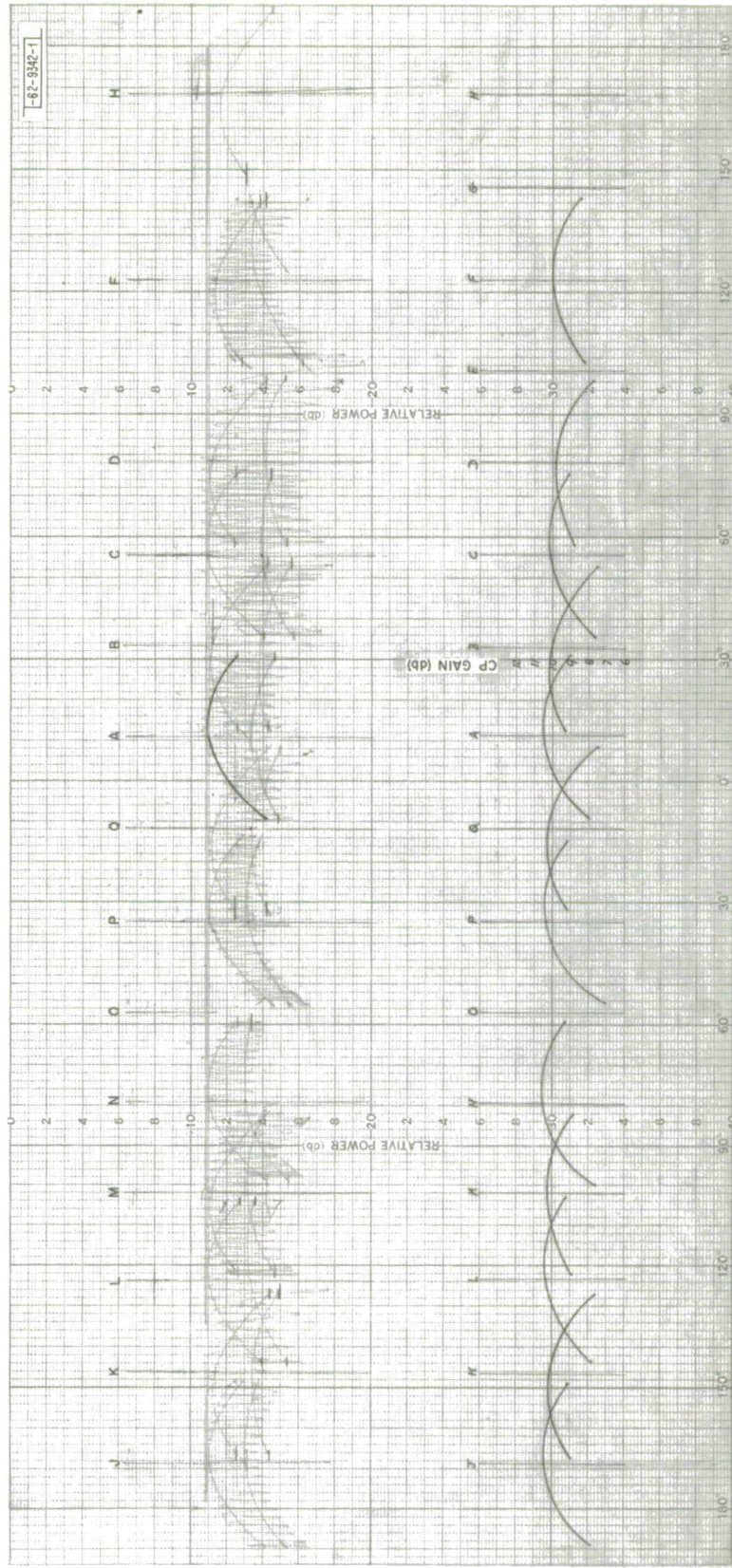
(a) Equatorial-plane pattern.

Fig. 65. Radiation patterns for scan mode, receive frequency.
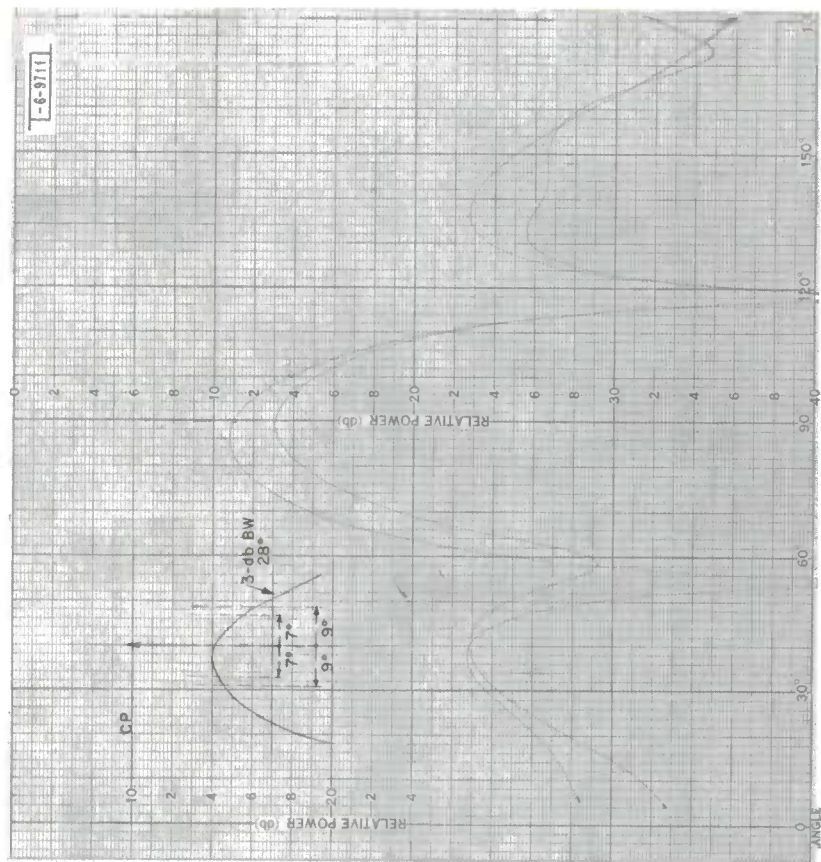
(b) Polar–plane pattern.

Fig. 65.   Continued.
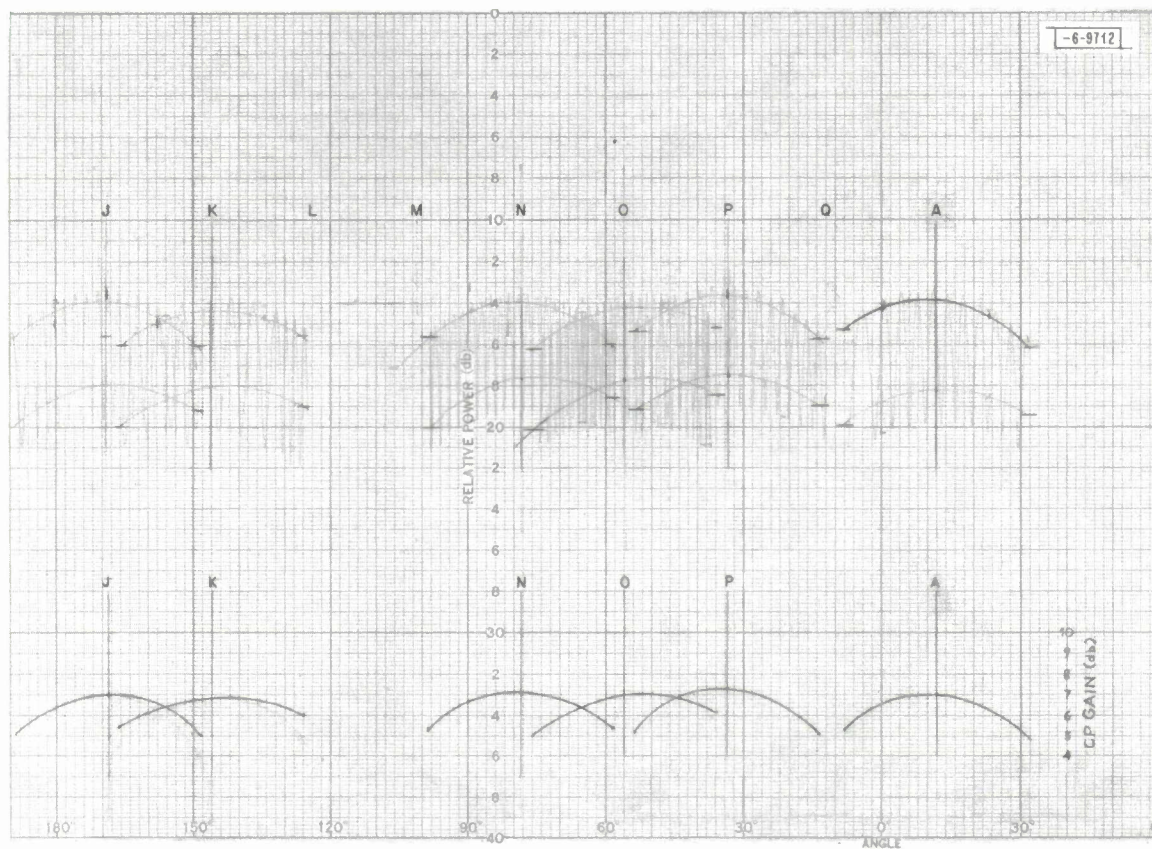
(a) Lowest RFI band frequency.

Fig. 66. Equatorial-plane patterns for scan mode.
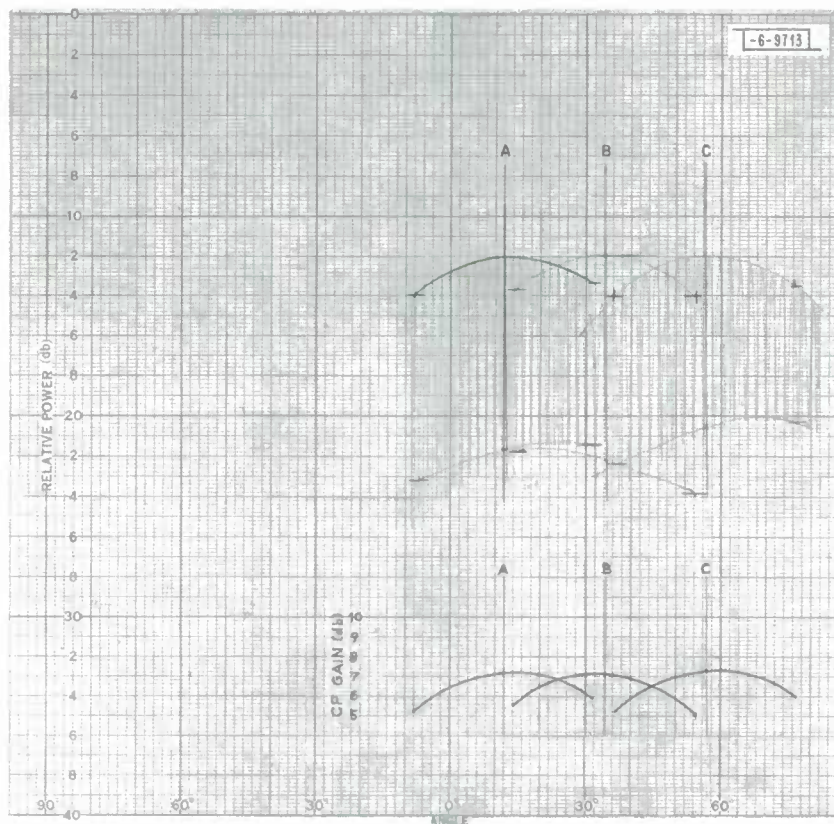
(b) Highest RFI band frequency.

Fig. 66. Continued.
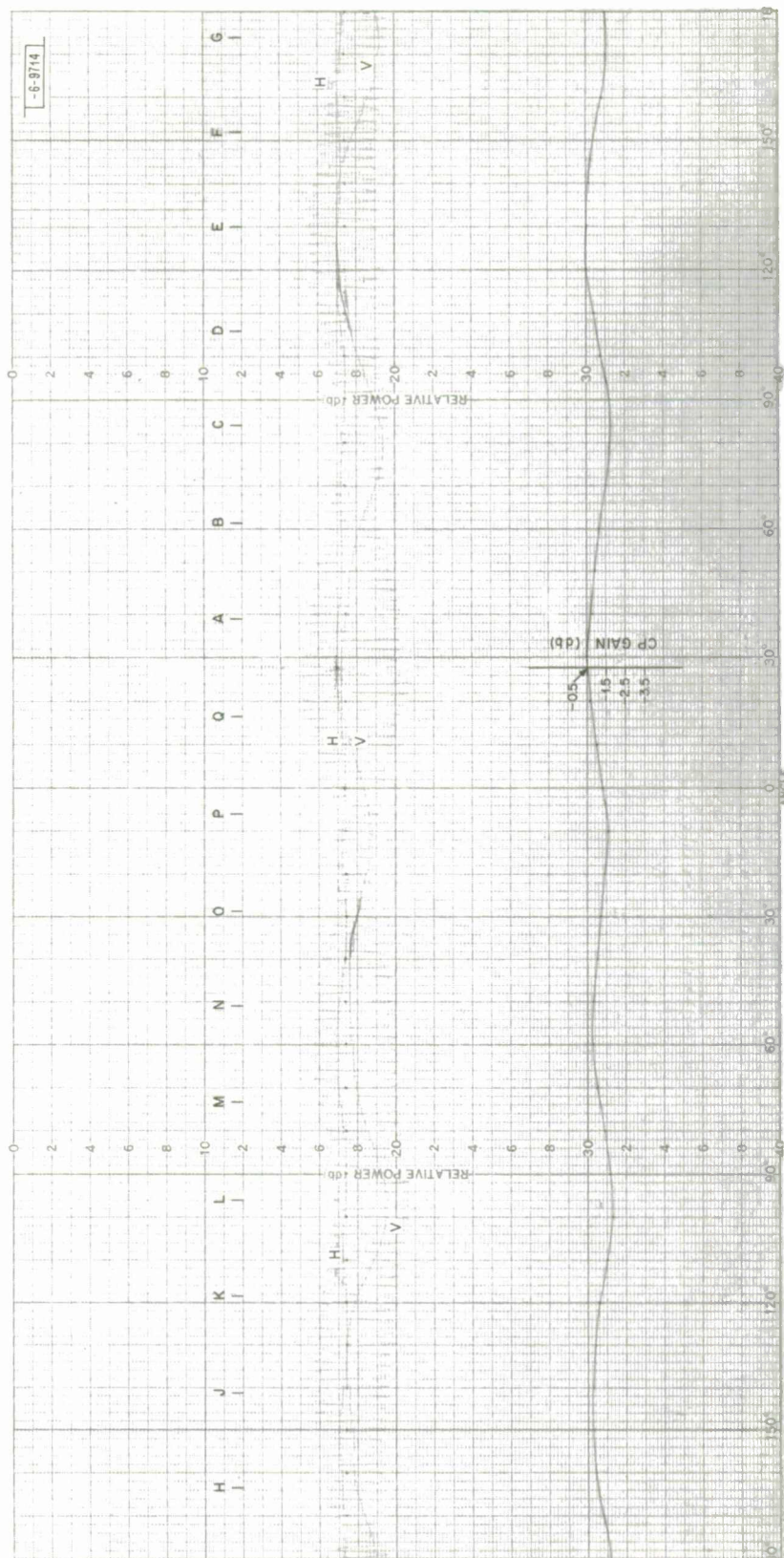
(a) Transmit frequency.

Fig. 67. Equatorial-plane patterns for omni-mode.
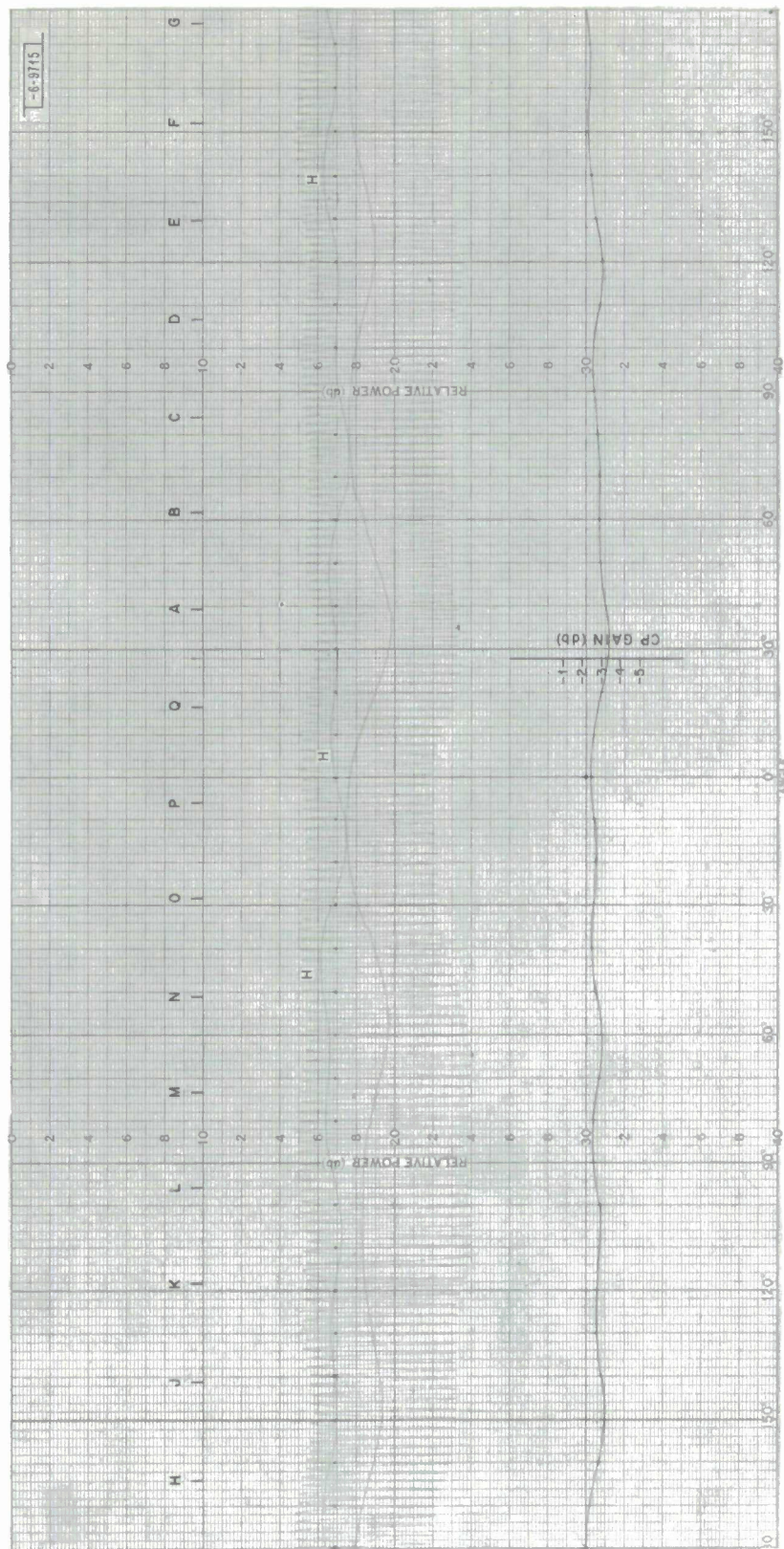
(b) Beacon frequency.

Fig. 67. Continued.

71
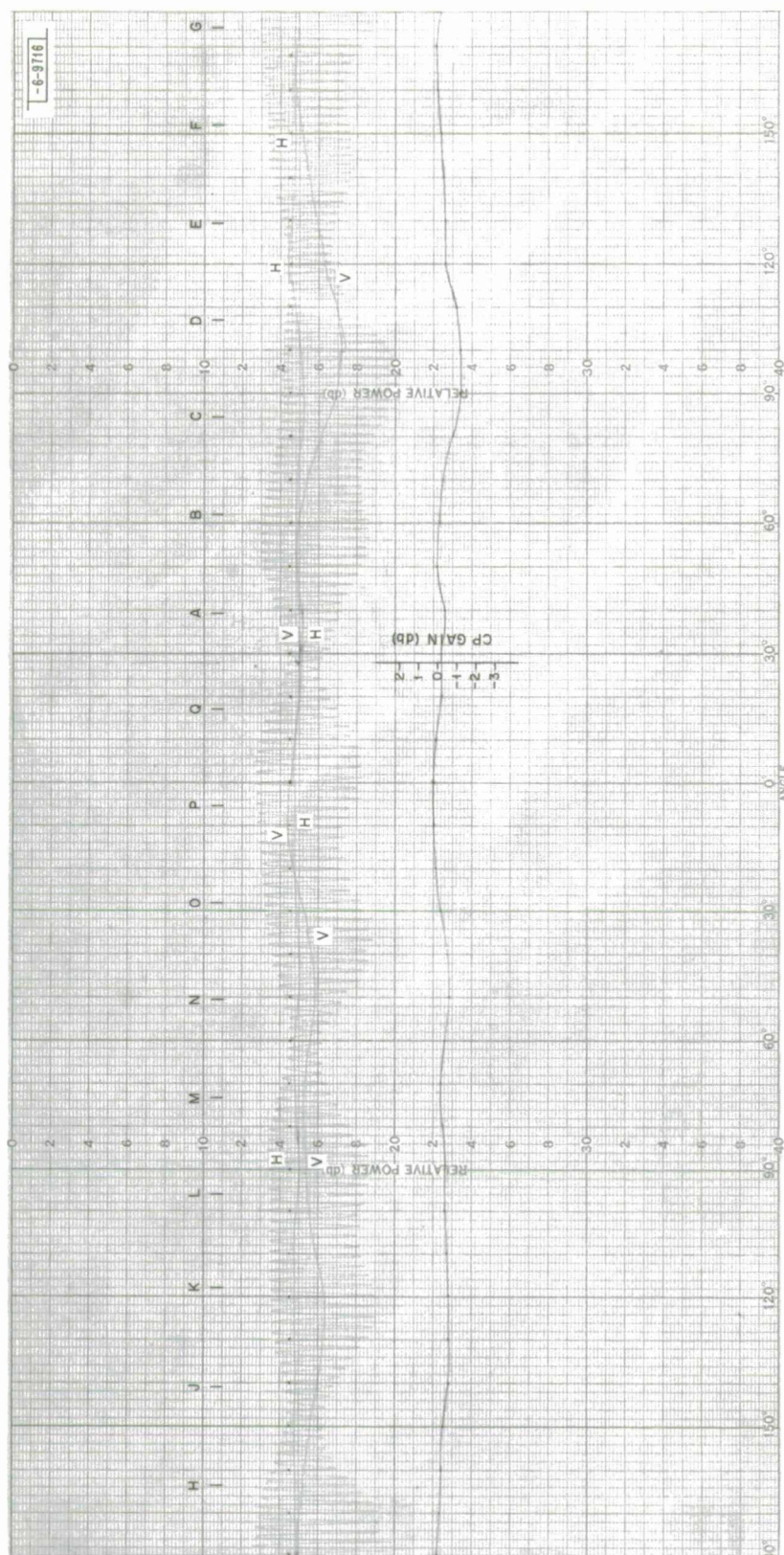
(c) Receive frequency.

Fig. 67. Continued.

72
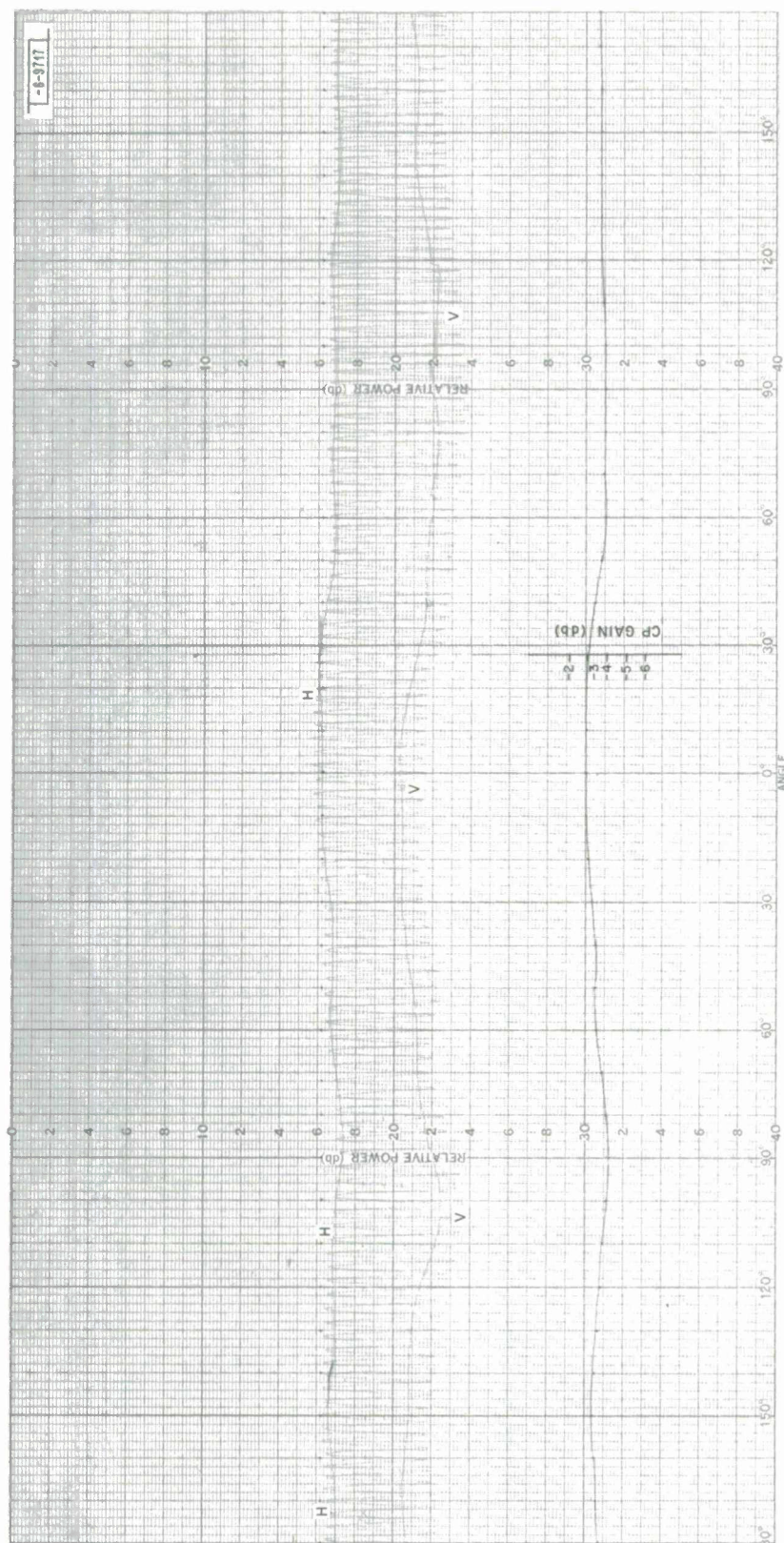
(a) Lowest RFI band frequency.

Fig. 68.  Equatorial-plane patterns for omni-mode.

73
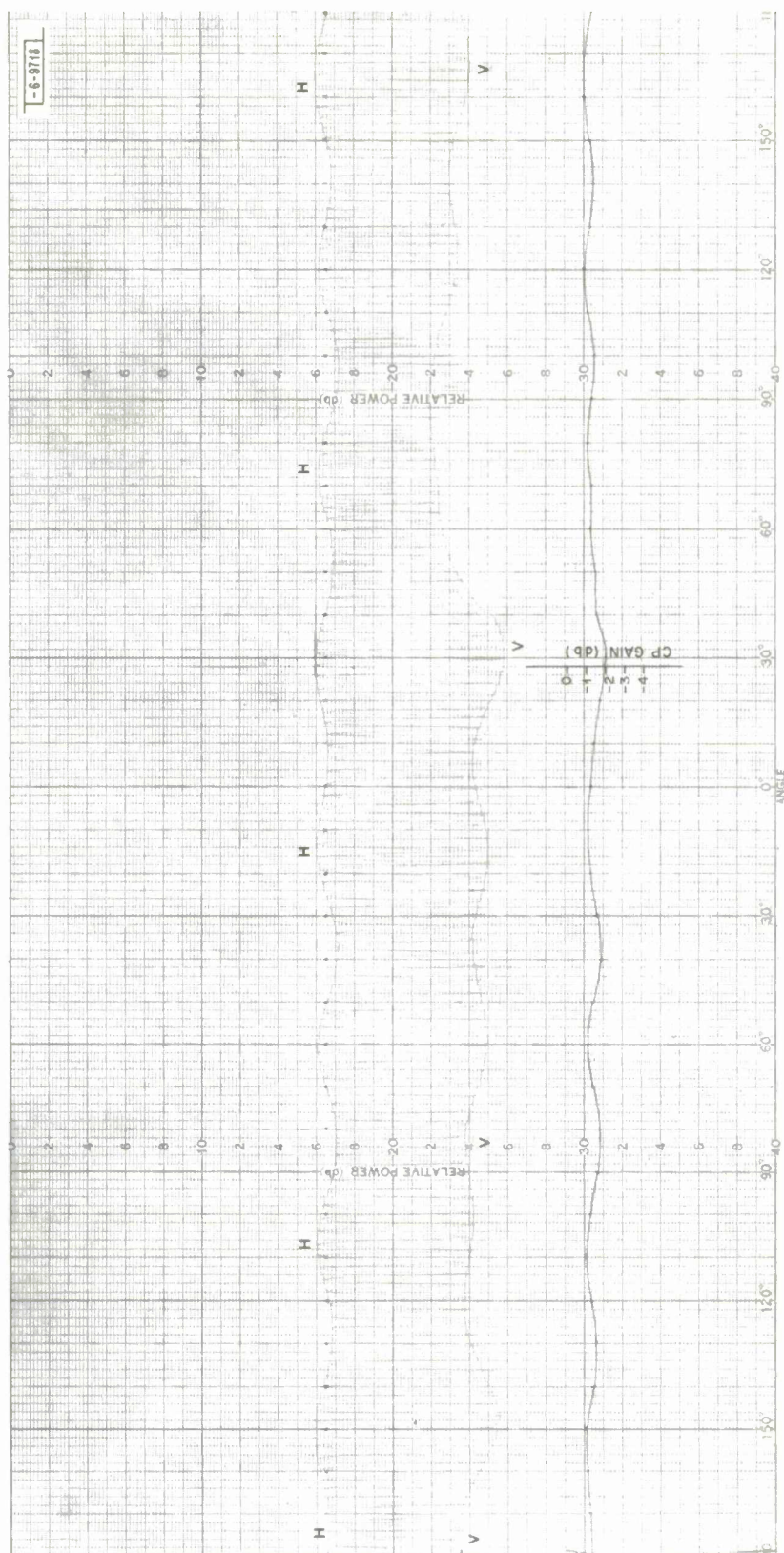
(b) Highest RFI band frequency.

Fig. 68. Continued.

74
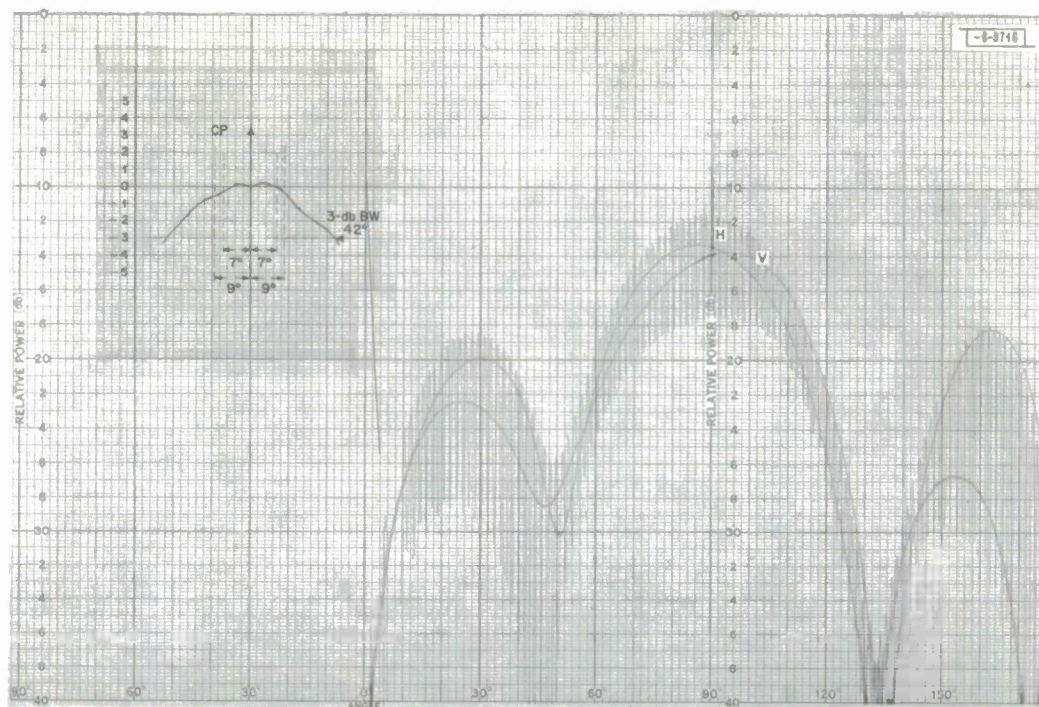
(a) Transmit frequency.
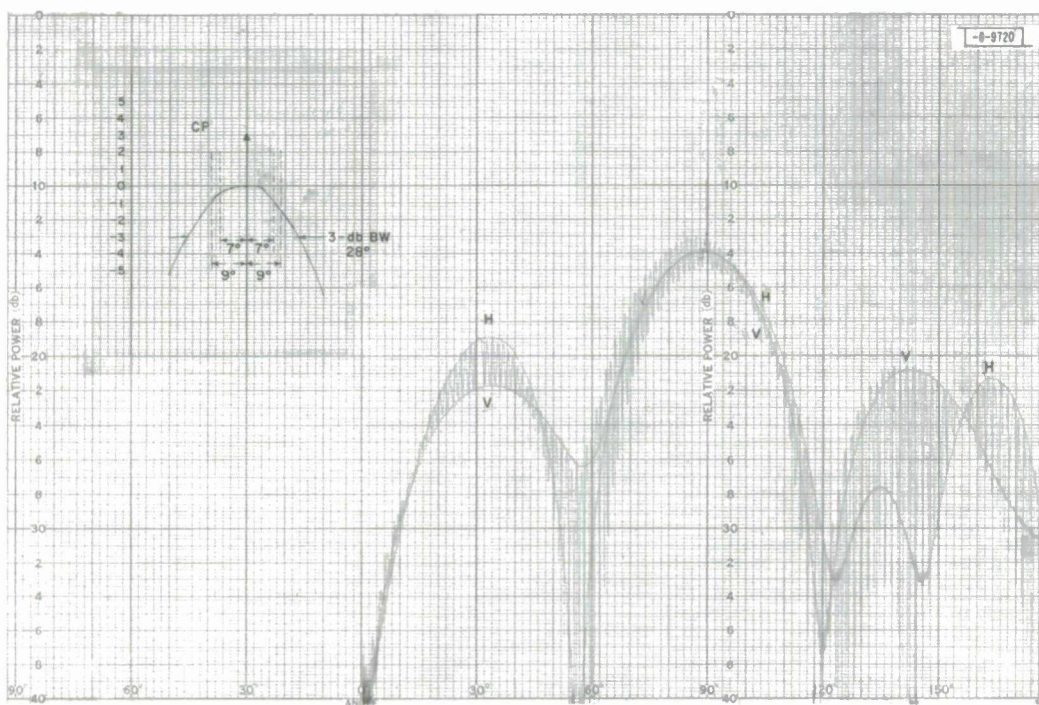


(b) Receive frequency.

Fig. 69.  Polar-plane patterns for omni-mode.

75
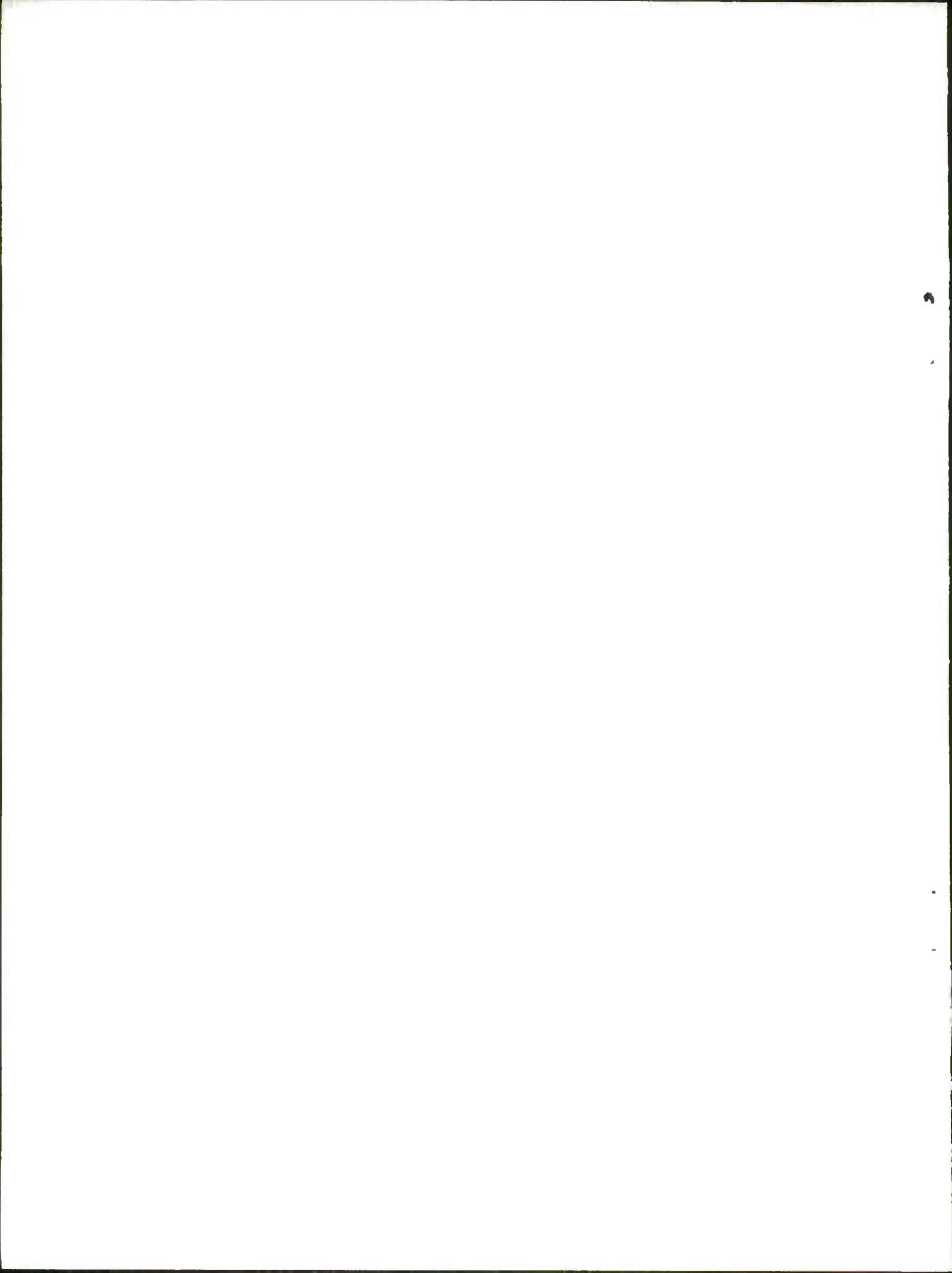
```
C   OIPOLE ARRAY AROUNO A CYLINOER
C   INPUT PARAMETERS-
C             RC     = RADIUS OF CYLINDER IN WAVELENGTHS
C             RR     = RADIUS OF RADIATOR CIRCLE IN WAVELENGHTS
C             N      = NO. OF OIPOLES IN A ROW
C             DPHI   = ANGULAR SEPARATION BETWEEN DIPOLES IN DEGREES
C             BETA   = PHASE OF EACH RADIATOR IN A ROW IN RAOIANS
C             AMP    = AMPLITUDE OF EACH RAOIATOR IN A ROW (VOLTAGE)
C             PMAX   = MAX. VALUE OF PHI IN DEGREES
C             PMIN   = MIN. VALUE OF PHI IN OEGREES
C             PINC   = INCREMENTAL VALUE OF PHI IN DEGREES
C             TMAX   = MAX. VALUE OF THETA IN OEGREES
C             TMIN   = MIN. VALUE OF THETA IN DEGREES
C             TINC   = INCREMENTAL VALUE OF THETA IN OEGREES
C             TO     = MAX. ALLOWABLE OIFF. OF CONSEQUTIVE TERMS OF THE
C                      SMALL N (NSM) LOOP
C             NQ     = NO. OF CONSEQUTIVE TERMS IN WHICH CRITERIA SET BY TO
C                      MUST BE MET
C             FIXTHE= FIXEO VALUE OF THETA(DEG.) WHEN PHI IS INCREMENTED
C             FIXPHI= FIXED VALUE OF PHI(DEG) WHEN THETA IS INCREMENTED,
C                      NOTE-IF FIXPHI MUST EQUAL PHIO,THE INPUT OF FIXPHI
C                      MUST BE 500.0
C             ROW = NO. OF ROWS
C             S = SPACING BETWEEN ROWS IN WAVELENGTHS
C             THE2 = UPPER LIMIT OF INTEGRATION
C             THE1 = LOWER LIMIT OF INTEGRATION
C             Q1   = MAX. ALLOWABLE OIFF. OF CONSEQUTIVE RESULTS OF
C                    INTEGRATION
C             TALL =    LENGTH OF ELEMENTS IN WAVELENGTHS
      CALL TIMHMS(JHOUR,JMIN,JSEC)
      DIMENSION AMP(10),BETA(10),EMAGT(200),PHASET(200),EMAGP(200),
     1PHASEP(200),POB(200),TOB(200),PHIO(200),PHIR(200),THEO(200),
     2THETR(200),TITLE(18)
      COMMON/DATA/    PIS,ROW,RCK,RRK,NQ,TD,PISR,DPM,PTALL,CPTALL,TALL
      COMPLEX HCO,HRO,VO,SUM1,AEJB,SUM2,XJN,HCN,HRN,VN,COSIN,EO,TERM,TWO
     1,RJN,CJN,CJO,RJO,AFACT,EO1,SUMP,SUMM,AEJ,CAREA,SIZE
      NAMELIST/INPUT/RC,RR,N,DPHI,BETA,AMP,PMAX,PMIN,PINC,TMAX,TMIN,
     1TINC,TD,NQ,FIXTHE,FIXPHI,         ROW,S,THE1,THE2,Q1,TALL
      IEND = 0
 1000 READ (5,1,ENO=9000)(TITLE(I),I=1,18)
    1 FORMAT (18A4)
      WRITE (6,1) (TITLE(I),I=1,18)
      REAO (5,INPUT)
      WRITE(6,INPUT)
      WRITE(6,1) (TITLE(I),I=1,18)
      TWO=(2.0,0.0)
      PTALL = 3.14159*TALL
      CPTALL = COS(PTALL)
      NINCP = (PMAX-PMIN)/PINC+1.0
      NINCT = (TMAX-TMIN)/TINC+1.0
C SET UP TABLES OF PHI(OEG.) AND PHI(RAD.)
      DO 10 JP = 1,NINCP
      PHIO(JP) = PINC*FLOAT(JP-1)+PMIN
   10 PHIR(JP) = PHID(JP)*.0174533
C SET UP TABLES OF THET(OEG.) ANO THET(RAO.)
      THEO(1) = TMIN
      IF(TMIN.EQ.0.0) THEO(1) = 5.0
      THETR(1)= THEO(1) *.0174533
      DO 20 JO = 2,NINCT
      THED(JO) = TINC*FLOAT(JO-1)+TMIN
```

77

```
       20 THETR(JO)= THED(JD)*.0174533
          DPHIR= DPHI*.0174533
          PHIO = FLOAT(N-1)/2.0*DPHIR
          THETAO = 1.5708
          IF(FIXPHI.EQ.500.0) GO TO 30
          PHI = FIXPHI*.0174533
          GO TO 40
       30 PHI=PHIO
          XPHI=PHI/.0174533
       40 INC=NINCT
          RAD=THETR(1)
          ASSIGN 200 TO K2
          RCK = RC*6.28319
          RRK = RR*6.28319
          K3=-1
          ISWTCH = 0
          PIS = S*3.14159
          PISR = PIS*ROW
C LOOP FOR THETA OR PHI ITERATIONS
       45 DO 910 J=1,INC
          SINR = SIN(RAO)
          COST = COS(RAO)
          IF(COST.LT.1.0E-8) COST=1.0E-8
          IF(TALL.GT..1) GO TO 888
          SIZE = (1.0,0.0)
          GO TO 889
      888 SIZE = CMPLX((COS(PTALL*COST)-CPTALL)/SINR,0.0)
      889 IF(ROW.EQ.1.0) AFACT = (1.0,0.0)
          IF (ROW.EQ.1.0) GO TO 201
          IF(ISWTCH.GT.0) GO TO 46
          SPI = PIS*COST
          SPIROW = SPI*ROW
          AFACT =CMPLX( SIN(SPIROW)/SIN(SPI),0.0)
          IF(INC.EQ.NINCP) ISWTCH = ISWTCH + 1
      201 ARGRC = RCK*SINR
          ARGRR = RRK*SINR
          CALL HANKEL (ARGRC,0,HCO)
          CJO = CMPLX(REAL(HCO),0.0)
          CALL HANKEL (ARGRR,0,HRO)
          RJO = CMPLX(REAL(HRO),0.0)
          VO = RJO - HRO/HCO*CJO
       46 SUM1 = (0.0,0.0)
C LOOP FOR M ITERATIONS
          DO 910 M=1,N
          M1=M-1
          AEJB = CMPLX(AMP(M),0.0)*CEXP(CMPLX(0.0,BETA(M)))
          NTEST =-1
          KOUNT = 0
          NSM = 0
          SUM2= (0.0,0.0)
       50 NSM = NSM+1
          IF(NSM.GT.90)GO TO 82
          XJN = (0.0,1.0)**NSM
          CALL HANKEL (ARGRR,NSM,HRN)
          RJN = CMPLX(REAL(HRN),0.0)
          CALL HANKEL (ARGRC,NSM,HCN)
          CJN = CMPLX(REAL(HCN),0.0)
          VV = RJN - HRN/HCN*CJN
          COSIN =CMPLX(COS(NSM*(PHI-M1*DPHIR)),0.0)
          SUM2 = XJN*VN*COSIN+SUM2
          TERM = AEJB*(VO+TWO*SUM2)
          S1=CABS(TERM)
          IF(NTEST.GT.0) GO TO 80
```

```fortran
   70 S2 = S1
      NTEST = 1
      GO TO 50
   80 IF(ABS(S1/S2-1.0).GT.TO) GO TO 100
      KOUNT = KOUNT + 1
      IF(KOUNT-NQ) 70,110,110
   82 WRITE (6,90) M,RAD,PHI
   90 FORMAT (//4X,'ITERATIONS OF SMALL N IN FIELD EQUAT. LIMITED TO 90
     1WHEN M=',I2,'THETA=',F6.4,'PHI=',F6.4//)
      GO TO 110
  100 KOUNT = 0
      GO TO 70
  110 SUM1=TERM + SUM1
      IF (M.LT.N) GO TO 910
      EO1= SUM1*CMPLX(SINR,0.0)
      EO = EO1*AFACT*SIZE
      IF(K3.GT.0) GO TO 914
      GO TO K2,(200,300)
  200 EMAGT(J)=CABS(EO)
      PHASET(J)=ATAN2(AIMAG(EO),REAL(EO))
      IF(J.EQ.INC) GO TO 910
      RAD=THETR(J+1)
      GO TO 910
C CALC. TABLES-MAGNITUDE OF EPHI AND PHASE ANGLE WHEN THETA IS CONSTANT
C CALC. TABLES-MAGNITUDE OF ETHETA AND PHASE ANGLE WHEN PHI IS CONSTANT
  300 EMAGP(J)=CABS(EO)
      PHASEP(J)=ATAN2(AIMAG(EO),REAL(EO))
      IF(J.EQ.INC) GO TO 912
      PHI = PHIR(J+1)+PHIO
  910 CONTINUE
      ASSIGN 300 TO K2
      RAD = FIXTHE *.0174533
      INC =NINCP
      PHI = PHIR(1)+PHIO
      GO TO 45
  912 K3 =1
      PHI=PHIO
      RAD = THETAO
      INC =1
      GO TO 45
  914 ENOT = CABS(EO)
      ANGNOT   =ATAN2(AIMAG(EO),REAL(EO))
      ENOTDB = 20.0*ALOG10(ENOT)
C  CALCULATION FOR DIRECTIVITY
      PIE = 3.14159
      SUMP = (0.0,0.0)
      DO 402 IP=1,N
      IPL1=IP-1
      SUMM = (0.0,0.0)
      DO 401 IM=1,N
      IML1=IM-1
      DPM = OPHIR*FLOAT(IPL1-IML1)
      AEJ = CMPLX(AMP(IM),0.0)*CEXP(CMPLX(0.0,BETA(IM)-BETA(IP)))
C  START OF INTEGRATION
C  INTEGRATION
      KOUNT = 0
      DX = THE2-THE1
      SUMZ = 0.0
      MSM = 0
  206 MSM = MSM+1
      MZ = 0
  202 MZ = MZ+1
      X = (2.0*FLOAT(MZ)-1.0)*DX/2.0**MSM+THE1
      SUMZ = SUMZ+FUN(X)
      LZP = MSM-1
      IF (MZ-2**LZP) 202,203,203
```

```
    203 MP1 = MSM+2
        E = 2.0**MP1
        XLO = THE1+DX/E
        XHI = THE2-DX/E
        IF (MSM.GT.1) GO TO 205
        SUM11 = SUMZ+FUN(XLO)/2.0+FUN(XHI)/2.0
        GO TO 206
    205 SUM22 = SUMZ+FUN(XLO)/2.0+FUN(XHI)/2.0
        RATIO = SUM22/SUM11
        IF (Q1-ABS(RATIO-2.0))301,301,304
    301 KOUNT = 0
    303 SUM11 = SUM22
        RAMAG = ABS(RATIO-2.0)
        IF (MSM-8) 206,206,218
    218 WRITE (6,219)
    219 FORMAT (5X,33HINTEGRATION POINTS LIMITED TO 512)
        GO TO 308
    304 KOUNT = KOUNT+1
        IF (KOUNT-2) 303,307,307
    307 P = 10.0*Q1-(RAMAG+ABS(RATIO-2.0))*5.0
        IF (P-Q1) 303,308,308
    308 INCTOT = 2**MSM
        DELTX = DX/FLOAT(INCTOT)
        AREA = SUM22*DELTX
        WRITE (6,309) INCTOT
    309 FORMAT (10X,26HTOTAL INTEGRATION POINTS= ,I4)
  C   END OF INTEGRATION
        CAREA = CMPLX(AREA,0.0)
        SUMM = AEJ*CAREA+SUMM
    401 CONTINUE
        SUMP = CMPLX(AMP(IP),0.0)*SUMM+SUMP
    402 CONTINUE
        DIR =       ENOT**2/CABS(SUMP)
        DIRDB = 10.0*ALOG10(DIR)
  C   END OF DIRECTIVITY CALCULATION
        DO 920 JP=1,NINCP
    920 POB(JP)=20.0*ALOG10(EMAGP(JP))-ENOTOB+DIRDB
        DO 930 JT=1,NINCT
    930 TOB(JT)=20.0*ALOG10(EMAGT(JT))-ENOTDB+DIRDB
  C
  C   WRITE OUTPUTS
  C
        WRITE(6,1)(TITLE(I),I=1,18)
        WRITE(6,940) PHIO,THETAO,ENOT,ANGNOT
    940 FORMAT(/6X,'PHIO=',F7.4,6X,'THETAO=',F7.4,6X,'MAGNITUDE AT (PHIO,T
       1HETAO=',F10.6,6X,'PHASE ANGLE AT (PHIO,THETAO)=',F10.6)
        WRITE(6,950) RC,RR,OPHIR
    950 FORMAT(/6X,'CYLINDER RADIUS=',F8.6,6X,'RADIATOR RADIUS =',F8.6,6X,
       1 5HDPHI=,F7.6,7HRADIANS)
        WRITE(6,959) DIR,DIRDB
    959 FORMAT(/6X,'MAGNITUDE OF DIRECTIVITY=',F10.6,'DIRECTIVITY IN DB=',
       1F10.6)
        WRITE(6,960) N,FIXTHE,XPHI
    960 FORMAT(/6X,'NO. OF DIPOLES =',I2,6X,'THETA(DEG) WHEN PHI IS INCREM
       1ENTED=',F7.4,6X,'PHI(DEG) WHEN THETA IS INCREMENTED=',F7.4//)
        WRITE(6,970)
    970 FORMAT(5X,3HPHI,10X,4HEPHI,7X,14HPHASE-ANG(RAD),10X,2HDB,15X,5HTHE
       1TA,10X,4HETHE,7X,14HPHASE-ANG(RAD),10X,2HOB)
        IF(NINCP-NINCT) 751,751,752
    751 MS = NINCP
        MB = MS+1
        GO TO 753
    752 MS = NINCT
        MB = MS+1
```

80

```
  753 WRITE(6,4)(PHID(J),EMAGP(J),PHASEP(J),POB(J),THEO(J),EMAGT(J),
     1PHASET(J),TOB(J),J=1,MS)
    4 FORMAT (2X,F8.2,E16.6,E17.6,E17.6,F15.2,E18.6,E17.6,E18.6)
      IF(NINCP-NINCT) 754,760,756
  754 WRITE(6,755) (THEO(J),EMAGT(J),PHASET(J),TOB(J),J=MB,NINCT)
  755 FORMAT (60X,F15.2,E18.6,E17.6,E18.6)
      GO TO 760
  756 WRITE (6,19) (PHIO(J),EMAGP(J),PHASEP(J),POB(J),J=MB,NINCP)
   19 FORMAT (2X,F8.2,E16.6,E17.6,E17.6)
  760 CONTINUE
      IF(IENO.EQ.0) CALL STOIOV(TITLE,49,0)
      IENO = 1
      CALL CAM2V(XX)
      PO = PDB(1)
      DO 998 J = 1,NINCP
      IF (PO-POB(J)) 903,997,997
  903 YMAX = POB(J)
      PO = POB(J)
      GO TO 998
  997 YMAX=PO
  998 CONTINUE
      YMAX = YMAX+5.0
      YMIN = YMAX-40.0
      CALL GRID1V (2,PMIN,PMAX,YMIN,YMAX,5.,1.,4,5,-4,-10,3,3)
      CALL APLOTV (NINCP,PHID,POB,1,1,1,38,IERR)
      CALL APLOTV (NINCT,THEO,TOB,1,1,1,55,IERR)
      CALL RITE2V (15,300,1012,90,1,20,1,'OB-(EPHI=O,ETHETA=X)',IERR3)
      CALL RITE2V (400,10,1012, 0,1,16,1,' OEG-(PHI,THETA)',IERR3)
      CALL RITE2V (100,1010,1012,0,1,50,1,TITLE,IERR3)
      CALL FRAMEV(0)
      CALL TIMHMS(KHOUR,KMIN,KSEC)
      WRITE(6,5028)KHOUR,KMIN,KSEC
 5028 FORMAT(//////10X,'ENO OF EXECUTION',5X,3I6)
      WRITE(6,5029) JHOUR,JMIN,JSEC
 5029 FORMAT(10X,'START OF EXECUTION',3X,3I6)
      GO TO 1000
 9000 CALL PLTND(X,X,X)
      RETURN
      ENO



      REAL FUNCTION FUN(T)
      COMMON/OATA/    PIS,ROW,RCK,RRK,NQ,TO,PISR,OPM,PTALL,CPTALL,TALL
      COMPLEX OHCO,OCJO,OHRO,ORJO,OVO,OHCN,OCJN,OHRN,ORJN,OVN
      COT = COS(T)
      IF(COT.LT.1.0E-8) COT = 1.0E-8
      SINT = SIN(T)
      IF(TALL.GT..1) GO TO 1
      SIZE = 1.0
      GO TO 2
    1 SIZE = ((COS(PTALL*COT)-CPTALL)/SINT)**2
    2 SINT3 = SINT**3 *SIZE
      IF(ROW.EQ.1.0) GO TO 449
      SINO = SIN(PIS*COT)
      SINN = SIN(PISR*COT)
      SFACT= (SINN/SINO)**2*SINT3
      GO TO 500
  449 SFACT = SINT3
```

```
      500 DARGRC = RCK*SINT
          DARGRR = RRK*SINT
          CALL HANKEL (DARGRC,0,DHCO)
          DCJO = CMPLX(REAL(DHCO),0.0)
          CALL HANKEL (DARGRR,0,DHRO)
          DRJO = CMPLX(REAL(DHRO),0.0)
          DVO = DRJO-DHRO/DHCO*DCJO
          DVO2 = CABS(DVO)**2
          S3 = 0.0
          NTEST = -1
          KOUNT = 0
          NS = 0
      511 NS = NS+1
          IF (NS.GT.20) GO TO 510
          CALL HANKEL(DARGRC,NS,DHCN)
          DCJN = CMPLX(REAL(DHCN),0.0)
          CALL HANKEL (DARGRR,NS,DHRN)
          DRJN = CMPLX(REAL(DHRN),0.0)
          DVN = DRJN- DHRN/DHCN*DCJN
          DVN2 = CABS(DVN)**2
          COSD = COS(FLOAT(NS)*DPM)
          S3 = CDSD*DVN2+S3
          IF (NTEST.GT.0) GO TO 520
      515 S4 =S3
          NTEST =1
          GO TO 511
      520 IF(ABS(S3/S4-1.0).GT.TD ) GO TO 517
          KOUNT = KOUNT + 1
          IF (KOUNT.EQ.NO)  GO TO 530
          GO TO 515
      510 TDEG = T/.0174533
          WRITE(6,516) NS,TDEG,IPL1,IML1
      516 FORMAT (1X,'INTEGRATION--SMALL N LIMITED TO ',I3,' WHEN THETA=',
         1F7.2,'SMALL P =',I2,' SMALL M =',I2)
          GO TO 530
      517 KOUNT = 0
          GO TO 515
      530 TWOS = 2.00*S3
          FUN = SFACT*(DVO2+TWDS)
          RETURN
          END


C     HANKEL FUNCTION TYPE 2
      SUBROUTINE HANKEL(ARG,J,RAG)
      DIMENSION NBSFN(1),BSFN(1)
      COMPLEX RAG
      ASSIGN 5 TO K
      IF(J) 1,2,2
    1 ASSIGN 6 TO K
      J=IABS(J)
    2 CALL BESSEL (J,ARG,1,NBSFN,BSFN)
      CALL BESY (ARG,J,VI,IERR)
      IF(IERR.GT.0) WRITE (6,100) IERR
  100 FORMAT (1H0,10X15HERROR IN BESY =I3)
      GO TO K,(5,6)
    5 R=BSFN(1)
      G=-VI
      RAG = CMPLX(R,G)
      RETURN
    6 R=-BSFN(1)
      G=VI
      RAG=CMPLX(R,G)
      RETURN
      END
```

## DOCUMENT CONTROL DATA - R&D

*(Security classification of title, body of abstract and indexing annotation must be entered when the overall report is classified)*

| 1. ORIGINATING ACTIVITY (Corporate author) | 2a. REPORT SECURITY CLASSIFICATION |
|---|---|
| Lincoln Laboratory, M.I.T. | Unclassified |
| | 2b. GROUP |
| | None |

3. REPORT TITLE

LES-6 Antenna System

4. DESCRIPTIVE NOTES (Type of report and inclusive dates)

Technical Report

5. AUTHOR(S) (Last name, first name, initial)

Assaly, Robert N.     LaPage, Bernard F.          Sotiropoulos, Arthur
Devane, Mark E.       Rosenthal, Milton L.

| 6. REPORT DATE | 7a. TOTAL NO. OF PAGES | 7b. NO. OF REFS |
|---|---|---|
| 10 March 1969 | 88 | 10 |

| 8a. CONTRACT OR GRANT NO. | 9a. ORIGINATOR'S REPORT NUMBER(S) |
|---|---|
| AF 19(628)-5167 | |
| b. PROJECT NO. | Technical Report 465 |
| 649L | |
| c. | 9b. OTHER REPORT NO(S) (Any other numbers that may be assigned this report) |
| d. | ESD-TR-69-43 |

10. AVAILABILITY/LIMITATION NOTICES

This document has been approved for public release and sale; its distribution is unlimited.

| 11. SUPPLEMENTARY NOTES | 12. SPONSORING MILITARY ACTIVITY |
|---|---|
| None | Air Force Systems Command, USAF |

13. ABSTRACT

The antenna system for Lincoln Laboratory's sixth experimental satellite (LES-6) is described. It is the first circularly polarized, despun, VHF antenna to be successfully used on an orbiting satellite. A relatively high-gain (11-db peak) beam is electronically scanned to be always Earth-directed. The evolution from the simple LES-5 antenna system is detailed, and performance characteristics of the flight configuration are given.

14. KEY WORDS

| | | |
|---|---|---|
| LES-6 | dipole antennas | antenna radiation patterns |
| LES-5 | slot antennas | Titan III-C |
| circular polarization | communications satellites | solid state |
| VHF | | |